Palladium Based Dense Metallic Membranes for Purification of Hydrogen Isotopes

By

Subhasis Pati

CHEM01201204021

Bhabha Atomic Research Centre

A thesis submitted to the
Board of Studies in Chemical Sciences
In partial fulfillment of requirements
For the Degree of
DOCTOR OF PHILOSOPHY
of
HOMI BHABHA NATIONAL INSTITUTE

December, 2016

Homi Bhabha National Institute

Recommendations of the Viva Voce Committee

As members of the Viva Voce Committee, we certify that we have read the dissertation prepared by **Shri Subhasis Pati** entitled [illegible] **Palladium Based Dense Metallic Membranes for Purification of Hydrogen Isotopes"** and recommend that it may be accepted as fulfilling the thesis requirement for the award of Degree of Doctor of Philosophy.

Chairman - Prof. S. K. Mukerjee **Date:** 23/02/2017

Guide / Convener - Dr. S. C. Parida **Date:** 23/02/2017

Examiner - Prof. K. K. Nanda KKNanda **Date:** 23/02/17

Member 1- Dr. Smruti Dash **Date:** 23/02/2017

Member 2- Dr. A. K. Tripathi Tripathi **Date:** 23/02/2017

Invitee/Technology Adviser - Dr. Manidipa Basu MBasu **Date:** 28-2-2017 *

Final approval and acceptance of this thesis is contingent upon the candidate's submission of the final copies of the thesis to HBNI.

I hereby certify that we have read this thesis prepared under our direction and recommend that it may be accepted as fulfilling the thesis requirement.

Date: 23/02/2017

Place: Mumbai

(Dr. S.C. Parida)
Guide

* I am fully satisfied with the content of the thesis and the presentation made by the student.

STATEMENT BY AUTHOR

This dissertation has been submitted in partial fulfillment of requirements for an advanced degree at Homi Bhabha National Institute (HBNI) and is deposited in the Library to be made available to borrowers under rules of the HBNI.

Brief quotations from this dissertation are allowable without special permission, provided that accurate acknowledgement of source is made. Requests for permission for extended quotation from or reproduction of this manuscript in whole or in part may be granted by the Competent Authority of HBNI when in his or her judgment the proposed use of the material is in the interests of scholarship. In all other instances, however, permission must be obtained from the author.

Subhasis Pati

(Subhasis Pati)

DECLARATION

I, hereby declare that the investigation presented in the thesis has been carried out by me. The work is original and has not been submitted earlier as a whole or in part for a degree / diploma at this or any other Institution / University.

Subhasis Pati

(Subhasis Pati)

List of Publications arising from the thesis

Journal: 04

(1) Pd-Ag-Cu dense metallic membrane for hydrogen isotope purification and recovery at low pressures. **Subhasis Pati**, R A. Jat,, N. S. Anand, D. J. Derose, K.N. Karn, S.K. Mukerjee, S.C. Parida, **J. Memb. Sci.** 522 (2017) 151-158.

(2) X-ray diffraction study of thermal parameters of Pd, Pd-Ag and Pd-Ag-Cu alloys as hydrogen purification membrane materials. **Subhasis Pati**, R. A. Jat, S.C. Parida, S. K. Mukerjee. **Physica B**. 484 (2016) 42-47.

(3) Hydrogen isotope effect on thermodynamic and kinetics of hydrogen/deuterium absorption–desorption in $Pd_{0.77}Ag_{0.10}Cu_{0.13}$ alloy. **Subhasis Pati**, R.A. Jat, S. K. Mukerjee, S. C .Parida. **J. Phys. Chem. C**. 119 (2015) 10314–10320.

(4) Thermodynamics and kinetics of hydrogen/deuterium absorption–desorption in $Pd_{0.77}Ag_{0.23}$ alloy. N. S Anand, **Subhasis Pati**, R. A. Jat, S. C. Parida and S. K. Mukerjee. **Int. J. Hydrogen Energy.** 40 (2015) 444-450.

Conferences: 05

(1) Hydrogen/Deuterium absorption kinetic studies on $Pd_{0.77}Ag_{0.23}$ alloy. **Subhasis Pati**, N. S. Anand, Ram Avatar Jat, S. C. Parida, S. K. Mukerjee. DAE-BRNS 5th Interdisciplinary Symposium on Material Chemistry (ISMC-2014), Dec 9-13, 2014, Mumbai, pp-321.

(2) Pressure-Composition- Temperature studies on $Pd_{0.77}Ag_{0.23}$ –H_2/D_2 Systems. N. S Anand, **Subhasis Pati**, R. A. Jat, S. C. Parida, S. K. Mukerjee. DAE-BRNS 5th

Interdisciplinary Symposium on Material Chemistry (ISMC-2014), Dec 9-13, 2014, Mumbai, pp-319.

(3) Thermal expansion studies of $Pd_{0.77}Ag_{0.23}$ alloy using high temperature X-ray diffraction technique. **Subhasis Pati**, Ram Avtar Jat , S.C. Parida, S. K. Mukerjee. DAE, BRNS Symposium and Workshop on Thermal Analysis (THERMANS-2016), pp-57.

(4) Pressure-Composition-Temperature studies on $Pd_{0.90}Cu_{0.10}$ –H_2/D_2 Systems. N. S Anand, **Subhasis Pati**, R. A. Jat, S. G. Sawant, S. C. Parida, S. K. Mukerjee. DAE, BRNS, Symposium and Workshop on Thermal Analysis (THERMANS-2016), pp-56.

(5) Synthesis and characterization of Pd-Ag alloy by electroless plating method. **Subhasis Pati**, R. A Jat, S. C. Parida. DAE-BRNS 6th Interdisciplinary Symposium on Material Chemistry (ISMC-2016), Dec 6-10, 2016, Mumbai, pp-194.

Subhasis Pati.

Subhasis Pati

Dedicated to My
Parents

ACKNOWLEDGEMENTS

I take this opportunity to express my feelings and gratitude to those people of eminence, whose help and support enabled me to complete this work. First of all, I am immensely indebted to my supervisor Dr. S. C. Parida, whose encouragement and interest has been a continuous source of stimulation for me throughout this work. Words cannot express how grateful I am. It is a great honour for me to be his student.

I would like to acknowledge Prof. S. K. Mukerjee, Ex-Head, PDD and Prof. B.S. Tomar Director RC & I Group for providing necessary facilities and encouraging me to carry out research work.

My gratitude also goes to all the doctoral committee members for their invaluable suggestions and encouragements to complete the work. I sincerely acknowledge Dr. Ram Avtar Jat for his guidance and assistance during my work. I would also like to take this opportunity to thank J. D. Derose, N. S. Anand, S.G. Sawant, K. B. Modi, Pradeep Samui, D. Chattaraj and all the members of PDD for their kindness and gracious assistance. My special thanks to all the members of workshop of PDD and glassblowing unit. I wish to thank Dr. V. Venugopal and Srikant Sahoo for their invaluable help during my stay in Mumbai. I am also thankful to my friends and well wishers for their inspiration.

I would like to extend my heartiest thanks to my two brothers and only sister, who provide me a source of encouragement to move forward in life. I would like to acknowledge the most important persons in my life, my parents "Your blessings for me was what sustained me this far". Heartfelt thanks goes to my grandmother for her unconditional love and blessings in my life. Finally, all thanks and praises to the God almighty for blessing me in this endeavor.

CONTENTS

SYNOPSIS

The purification of hydrogen isotopes attracted considerable interest in the last few decades because of increasing demand of ultrapure gases for fuel cell and fusion reactor applications. Classically, palladium membrane is in use for the purification of hydrogen isotopes to produce ultrapure gases due to high temperature compatibility and high hydrogen flux. However, surface poisoning of pure Pd membrane decreases the hydrogen flux whereas hydrogen embrittlement results in membrane cracking. Similarly, high cost of pure Pd limits its use in commercial scale. Hence, there is a need to overcome these issues for industrial application of Pd membranes for hydrogen purification. Alloying Pd with suitable elements such as Ag, Cu, Au etc. in required proportion is thought to overcome these issues.

This thesis work is aimed at developing Pd-based dense metallic membranes for purification of hydrogen isotopes. The preparation of Pd alloy membranes by conventional metallurgical route and supported membranes through electroless plating method were employed in this study. The membranes were characterized by using different techniques such as XRD, TXRF, SEM and EDS. Thermal expansion of these alloys were measured by using high-temperature X-ray diffraction technique. Membrane module with an ultra-high vacuum gas manifold was fabricated and hydrogen permeation experiments were carried out to derive permeation parameters. The H_2 and D_2 flux were measured at different temperatures and trans-membrane pressures. Thermodynamics and kinetics of hydrogen and deuterium sorption studies on these alloys were investigated. The thesis work results in development of a suitable Pd-Ag-Cu alloy membrane having higher hydrogen flux than the conventional Pd metal membrane. This thesis is divided into four chapters as outlined below.

Chapter 1: Introduction; Chapter 2: Experimental methods; Chapter 3: Results and Discussion and Chapter 4: Summary and Conclusion. A brief outline of each chapter is described below.

Chapter 1: Introduction.

The technology of hydrogen purification utilizing dense metallic membranes such as Pd and its alloys dates back over 50 to 60 years [1-2]. The increased demand of ultra-pure hydrogen for various applications propelled the field of metal membrane research in recent years [3-4]. Parallel to this, the development of fusion reactor through International Thermonuclear Research Reactor (ITER) initiative has demanded the utilization of dense metallic membrane for purification of the heavier hydrogen isotopes, namely deuterium and tritium [5-7]. Pd-based dense metallic membranes find application for both the purposes. The same membrane material can be used for both the applications; however, the process requirements are different. In the purification process of industrially produced hydrogen by steam reforming process, the impurities in the feed gas are mainly CO_2, CO, H_2O and unreacted hydrocarbons. In order to purify hydrogen from these impurities with a reasonably high permeation rate, the trans-membrane pressure is usually kept high (> 3 bar) at moderate temperature (500-800 K). Cost effective and supported composite membranes having lower noble metal inventory with moderate hydrogen perm-selectivity (500 to 1000) are being extensively explored for this application.

On the other hand, in the fusion reactor, the plasma exhaust stream mostly contains hydrogen isotopes (Q_2: Q = H, D, T) with a few to possibly 20% impurities such as: CQ_4, CO_2, CO, O_2, Q_2O, N_2, NQ_3 and He [6]. These impurities degrade plasma conditions and hence need to be removed before further processing in the fusion fuel cycle. Other gaseous streams which will require purification of hydrogen isotopes include neutral beam, pellet injector and blanket tritium recovery (BTR) gases [6]. In the BTR system, tritium will be extracted from the breeder material by passing helium sweep gas though the blanket [8]. The sweep gas with released tritium will be sent to a BTR system for tritium separation. Pd-based membrane reactor coupled to a Pd-based membrane diffuser, where low concentration of Q_2 needs to be recovered, is proposed for this application [8]. In all these applications, the transmembrane pressure is kept low (approximately 100 kPa) and the Q_2 partial pressure in the feed gas varies from 1 Pa to 100 kPa. The membrane temperature is preferred to be within 500-700 K to minimize tritium losses due to permeation through reactor walls. Radiation resistant membranes with infinite hydrogen perm-selectivity are the prime requirement for this application.

The present thesis deals with development of palladium based alloy for both the above applications. Pd-Ag and Pd-Ag-Cu alloy membranes were prepared by conventional metallurgical route as well as by electroless plating method. In the metallurgical route, membranes were prepared by arc melting followed by cold rolling and annealing. In this method, membranes of 100 μm thickness were prepared. In the electroless plating method, Pd-Ag and Pd-Ag-Cu alloy membranes were prepared by electroless deposition of constituent elements on porous stainless steel support. In this method, membranes of approximately 30 μm thickness were prepared. The alloy membranes prepared by both the methods were characterized for composition by TXRF and EDS, phase by XRD, morphology by SEM. Hydrogen and deuterium permeation experiments on membranes prepared by metallurgical route were carried out at different temperatures. Thermodynamics and kinetics of hydrogen and deuterium sorption on Pd-Ag, Pd-Ag-Cu alloys were carried out by employing Sievert's type volumetric apparatus. Further, the applicability of this membrane configuration was explored for purification of ^{3}He from traces of tritium.

Chapter 2: Experimental

Pd alloys of compositions $Pd_{0.77}Ag_{0.23}$ and $Pd_{0.77}Ag_{0.10}$ $Cu_{0.13}$ were prepared by arc melting method. Alloy foils of 100 µm thickness were prepared by cold rolling method followed by surface cleaning and intermediate annealing. These membrane foils were utilized for permeation experiments and thermal expansion studies. $Pd_{0.77}Ag_{0.23}$ foil was also used for measurement of kinetic parameters of H_2 and D_2 absorption reaction. Powders of $Pd_{0.77}Ag_{0.10}Cu_{0.13}$ alloy was prepared by filing the alloy ingot with a diamond file followed by annealing in a reduced atmosphere. These powder samples were used for thermodynamic and kinetic measurements of H_2 and D_2 sorption reactions. Compositional analysis of all these alloys was carried out by TXRF and EDS. Phase analysis of all these alloys were carried out by XRD. The thermal expansion of Pd, $Pd_{0.77}Ag_{0.23}$ and $Pd_{0.77}Ag_{0.10}Cu_{0.13}$ foils were measured using high-temperature XRD measurements.

Further, Pd, Pd-Ag and Pd-Ag-Cu alloy membranes were synthesized by electroless plating method over porous stainless steel (PSS) substrate. Sequential and co-deposition procedure was adopted for deposition of alloys followed by annealing in inert and hydrogen atmosphere. The plated membrane was characterized by XRD, SEM and EDS for phase, morphology and compositional analysis before and after annealing. Thickness of metal deposited was calculated from the mass gain after plating.

H_2/D_2 permeation behavior of 100 µm thick $Pd_{0.77}Ag_{0.23}$ and $Pd_{0.77}Ag_{0.10}Cu_{0.13}$ alloy membranes were investigated at different trans-membrane pressures of 50-150 kPa in the temperature range of 523-673 K. The annealed foils were vacuum brazed with a solid SS 316 L tube. The performance of the membrane was tested using a re-circulatory gas permeation setup. The hydrogen selectivity of the membrane was found out by analyzing the permeate gas using a residual gas analyzer (RGA). During isothermal permeation experiments, the partial pressure of H_2/D_2 in the feed side was maintained constant and the permeate side was maintained under vacuum by continuously absorbing the permeate gas in the uranium getter trap. The H_2 and D_2 flux was calculated by metering the amount of gas permeated through the membrane using a mass flow meter in the permeate side.

Kinetics of H_2/D_2 absorption on $Pd_{0.77}Ag_{0.23}$ alloy foil was investigated using a Sieverts' type volumetric apparatus in the temperature range of 335-394 K. Isotopic effect on thermodynamics and kinetics of hydrogen and deuterium sorption reactions on $Pd_{0.77}Ag_{0.10}Cu_{0.13}$ alloy powders were investigated using the same apparatus. The pressure-composition-isotherms (PCIs) for desorption reaction of $Pd_{0.77}Ag_{0.10}Cu_{0.13}$-$H_2/D_2$ systems were generated in the temperature range of 313-393 K and the constant volume kinetic measurements for absorption of hydrogen/deuterium on $Pd_{0.77}Ag_{0.10}Cu_{0.13}$ alloy was carried out in the temperature range of 303-333 K.

Chapter 3: Results and Discussion

Preparation and characterization of alloy by metallurgical route

TXRF analysis of composition of alloys prepared by metallurgical route confirmed their compositions to be $Pd_{0.77}Ag_{0.23}$ and $Pd_{0.77}Ag_{0.10}Cu_{0.13.}$ The XRD analysis confirmed the formation of single f.c.c phase and it was found out that Ag addition expands the lattice whereas Cu addition contracts the lattice. The calculated lattice parameters of Pd, $Pd_{0.77}Ag_{0.23}$ and $Pd_{0.77}Ag_{0.10}Cu_{0.13}$ were compared with those based on Vegard's law which shows that the alloys follow negative deviation from Vegard's law. The average values of coefficient of linear thermal expansion (α_T) for Pd, $Pd_{0.77}Ag_{0.23}$ $Pd_{0.77}Ag_{0.10}Cu_{0.13}$ obtained in this study are 12.65×10^{-6}, 10.24×10^{-6} and 9.32×10^{-6} K^{-1}, respectively, which follows the trend: $\alpha_T(Pd) > \alpha_T(Pd_{0.77}Ag_{0.23}) > \alpha_T(Pd_{0.77}Ag_{0.10}Cu_{0.13})$. Debye temperatures of $Pd_{0.77}Ag_{0.23}$ and $Pd_{0.77}Ag_{0.10}Cu_{0.13}$ calculated from high temperature XRD data are found to be 225 ± 10 K and 165 ± 10 K, respectively.

Preparation and characterization of alloys by electroless plating method

The electroless plating of palladium and its alloys were carried out on PSS support. For effective utilization of these membranes in hydrogen permeation experiments, the PSS was required to be joined to non-porous SS pipe which was achieved by lased welding. The PSS substrate was activated using acidic solution of $PdCl_2$ and $SnCl_2$. A hydrazine based plating bath was used to deposit Pd, Pd-Ag and Pd-Ag-Cu alloy. XRD patterns of the annealed deposits show the formation of single phase alloy having f.c.c crystal structure. SEM pictures show that the supported membranes were defect free.

Hydrogen and deuterium permeation of alloy prepared by metallurgical route

For permeation experiments, a mixture of He and H_2/D_2 gas was used in the feed side. Analysis of the permeate gas using RGA shows that the He is absent in the permeate side which confirmed that the membrane has infinity selectivity for hydrogen. The Q_2 flux at different temperatures shows a linear relationship with square root of partial pressure of Q_2 which suggests that diffusion through the bulk of the alloy is the rate determining step. The flux was found to increase with increase in H_2/D_2 partial pressure in the feed side and the increase in temperature. The permeability (P_e) of hydrogen isotopes in both alloy membranes follows the order: $P_e(H_2) > P_e(D_2)$. Hence it can be expected that P_e for T_2 will be even smaller. However, the permeability of H_2 and D_2 was found to be higher for $Pd_{0.77}Ag_{0.10}Cu_{0.13}$ than $Pd_{0.77}Ag_{0.23}$ at all experimental temperatures and trans-membrane pressures. These results show the favourable effect of replacement of silver with copper on permeability of hydrogen isotopes. The average values of apparent activation energies for H_2 permeation in both alloys are higher than D_2 permeation. Further, $Pd_{0.77}Ag_{0.10}Cu_{0.13}$ alloy membrane was used for the separation of He from a synthetic gas mixture containing He + 1% H_2. It was found that the membrane was efficient to produce high pure helium of 99.9% purity. This experiment demonstrated that $Pd_{0.77}Ag_{0.10}Cu_{0.13}$ alloy membrane can be suitably utilized in purification of ^{3}He from tritium contamination.

Thermodynamic and kinetic studies on $Pd_{0.77}Ag_{0.10}Cu_{0.13}$ – H_2/D_2 and $Pd_{0.77}Ag_{0.23}$ – H_2/D_2 systems

The H_2/D_2 desorption pressure-composition-isotherms (PCIs) for $Pd_{0.77}Ag_{0.10}Cu_{0.13}$ alloys shows a sloping but distinct plateau. The equilibrium pressure (P_{eq}) was found to follow the trend $P_{eq}(D_2) > P_{eq}(H_2)$ at all experimental temperatures. van’t Hoff plot (plot of ln P_{eq} vs. $1/T$) was constructed to evaluate the enthalpy ($\Delta_r H^o$) and entropy ($\Delta_r S^o$) of H_2/D_2 desorption reactions. The $\Delta_r H^o$ was found to be 37.2 ± 0.3 (kJ/mol H_2)

for hydride and 34.7 ± 0.2 (kJ/mol D_2) for deuteride. Similarly $\Delta_r S^o$ for hydride was found to be 95.4 ± 0.4 (J/(mol H_2·K)) and that of deuteride was 98.6 ± 0.3 (J/(mol D_2·K)). The difference in magnitude of enthalpy for the corresponding pair of hydrogen isotopes, $|\Delta_r H^o|_{(X = H)} - |\Delta_r H^o|_{(X = D)} > 0$, which suggest that hydrogen has more affinity to remain associated with the alloy in the condensed phase than deuterium thus showing normal hydrogen-isotope effect. Isotope separation factor (α) for plateau region of a particular isotherm was calculated from the experimental PCIs. The value of α at room temperature was found to be 2.00 $Pd_{0.77}Ag_{0.10}Cu_{0.13}$-$H_2/D_2$ which is comparable to those values of 2.27, 1.93 and 2.02 for Pd-H_2/D_2, Pd-Ag-H_2/D_2 and Pd-Cu-H_2/D_2 systems.

The constant volume kinetic data for H_2/D_2 absorption reaction for $Pd_{0.77}Ag_{0.23}$ alloy foil and $Pd_{0.77}Ag_{0.10}Cu_{0.13}$ alloy powders were generated and the experimental data were fitted with different kinetic models. For $Pd_{0.77}Ag_{0.23}$ alloy the model equations proposed by Fernandez et al. [9] pertaining to chemisorption as the rate limiting step best fits to the experimental data. Similarly, the pressure and concentration dependent model proposed by Wang and Suda [10] suggesting diffusion of H/D through the hydride or deuteride phase as the rate limiting step best fits the experimental kinetic data for $Pd_{0.77}Ag_{0.10}Cu_{0.13}$ alloy. The kinetic parameters are evaluated for the bi-phasic region where the hydride phase (β) co-exists with the dilute phase. An Arrhenius plot, ln k versus $1/T$, was constructed and the activation energies (E_a) for the absorption of H_2 and D_2 were derived. The corresponding values of E_a for absorption reaction are found to be 6.9 ± 0.2 (kJ/mol H_2) and 19.5 ± 0.6 (kJ/mol D_2) for $Pd_{0.77}Ag_{0.23}$ alloy and 25.8 ± 0.2 (kJ/mol H_2) and 50.2 ± 1.6 (kJ/mol D_2) for $Pd_{0.77}Ag_{0.10}Cu_{0.13}$ alloy. It is observed that deuterium absorption kinetics is slower than hydrogen, indicating higher activation energy of deuterium in both the alloys.

Chapter 4: Summary and Conclusion

The alloy membranes prepared by arc melting and cold rolling method were found to have single f.c.c phase over a temperature range of 298-1023 K. The coefficient of liner thermal expansion derived from the high temperature XRD analysis data shows the trend: $\alpha_T(\mathrm{Pd}) > \alpha_T(\mathrm{Pd_{0.77}Ag_{0.23}}) > \alpha_T(\mathrm{Pd_{0.77}Ag_{0.10}Cu_{0.13}})$. Debye temperature estimated from X-ray diffraction data of $Pd_{0.77}Ag_{0.10}Cu_{0.13}$ was found to be lower than that of $Pd_{0.77}Ag_{0.23}$.

Laser welding and low energy electron beam welding were found to be efficient techniques for joining porous SS substrate to non-porous SS pipe for preparation of permeation assembly. In the electroless plating experiments, surface cleaning and activation of the substrate, temperature and pH of the plating bath plays an important role for homogenous plating. Repeated plating and annealing in hydrogen atmosphere was found to be efficient for the formation of alloy membrane with improved hydrogen selectivity.

Membrane module was fabricated using vacuum brazing technique and found to have infinite selectivity towards hydrogen isotopes. Q_2 flux through these dense metallic membranes followed Sieverts' law, and diffusion through bulk was found to be the rate limiting step. Permeability of D_2 through both the alloy membranes was found to be lower than that of H_2 at all experimental temperatures and trans-membrane pressures. Permeability of Q_2 for $Pd_{0.77}Ag_{0.10}Cu_{0.13}$ alloy was found to be higher than

$Pd_{0.77}Ag_{0.23}$ alloy at all experimental conditions. Owing to the higher permeability of $Pd_{0.77}Ag_{0.10}Cu_{0.13}$, it can be a potential membrane material for efficient purification and recovery of hydrogen isotopes in the fuel cleanup system and blanket tritium recovery system of fusion fuel cycle. Further, infinite hydrogen selectivity for hydrogen in $Pd_{0.77}Ag_{0.10}Cu_{0.13}$ alloy foil membrane was found to be suitable for separation of decay product ^{3}He from tritium.

The PCIs for the desorption reaction of $Pd_{0.77}Ag_{0.10}Cu_{0.13}$-$H_2/D_2$ system reveals higher equilibrium plateau pressure for D_2 than H_2 at all experimental temperature. The enthalpies and entropies of desorption equilibrium reactions in the (α+β) region were found to be: $\Delta_r H^o = 37.2 \pm 0.3$ (kJ/mol H_2) and 34.7 ± 0.2 (kJ/mol D_2); $\Delta_r S^o = 95.4 \pm 0.4$ (J/(mol H_2·K)) and 98.6 ± 0.3 (J/(mol D_2·K)). Analysis of kinetic data for $Pd_{0.77}Ag_{0.10}Cu_{0.13}$-$H_2/D_2$ absorption reaction suggests that diffusion of H/D through the hydride/deuterides phase is the rate limiting step. Further, the analysis of data for $Pd_{0.77}Ag_{0.23}$-H_2/D_2 absorption reaction shows that in the bi-phasic (α+ β) region, dissociation and chemisorption is the rate-limiting step for H_2/D_2 absorption. However in both the cases the E_a of D_2 absorption was found to be higher than that of H_2 absorption. The overall study in this thesis shows that the ternary alloy $Pd_{0.77}Ag_{0.10}Cu_{0.13}$ is superior to the binary alloy $Pd_{0.77}Ag_{0.23}$ for hydrogen purification applications.

References:

[1] G. J. Grashoff, C. E. Pilkington, C. W. Corti, The purification of hydrogen, Platinum Metals Rev. 27 (1983) 157-169.

[2] S.N. Paglieri, J.D. Way. Innovations in palladium membrane research. Sep Purif. Rev. 31 (2002) 1-169.

[3] M. J. Cole, The generation of pure hydrogen for industrial applications, Platinum Metals Rev. 25 (1981**)** 12-13.

[4] P. P. Edwards, V. L. Kuznetsov, W. I. F. David, N. P. Brandon, Hydrogen and fuel cells: Towards a Sustainable Energy Future, Energy Policy, 36 (2008**)** 4356–4362.

[5] H. Yoshida, S. Konishi, Y. A. Naruse, Design study of a palladium diffuser for a D-T fusion fuel clean-up system, J. Less-Common Met. 89 (1983**)** 457- 464.

[6] R. S. Willms, S. Konishi, Fuel cleanup systems for fusion fuel processing, Fusion Eng. Des. 18 (1991) 53-60.

[7] Y. Shi, Y. J. Wei, Y. J. Su, Experimental studies on the hydrogen isotope recovery using low-pressure palladium membrane diffuser, J. Memb. Sci. 322 (2008) 302-305.

[8] Y. Kawamura, M. Enoeda, T. Yamanishi, M. Nishi, Feasibility study on the blanket tritium recovery system using the palladium membrane diffuser, Fusion Eng. Des. 81(2006) 809-814.

[9] G. E. Fernández, D. Rodríguez, G. Meyer. H_2 absorption kinetics of $MnNi_{4.7}Al_{0.3.}$ Int J Hydrogen Energy. 23 (1998) 1193-1196.

[10] X. L. Wang, S. A. Suda, Dehydriding kinetic study of $LaNi_{4.7}Al_{0.3}$ hydride by a stepwise method. J. Less-Common Met. 159 (1990) 109-119.

LIST OF FIGURES

LIST OF TABLES

CHAPTER 1

INTRODUCTION

Chapter 1. Introduction

The global energy demand is increasing day by day. In the present scenario, the main source of energy is based on fossil fuels such as coal, petroleum, natural gas, gasoline etc. The reserves of fossil fuels are limited and it is also decreasing day by day with the huge human consumption. Furthermore, the carbon released into the atmosphere due to the burning of these fossil fuels, in the form of CO_2 possess potential hazard for global climate change [1, 2]. Hence, alternative energy sources will eventually be required to fulfill the world's ever increasing energy demand [3, 4]. Hydrogen is one of the alternative energy sources which has a potential to meet the global energy demand and has less impact on global climate change [5].

1.1. Hydrogen as an energy carrier

Hydrogen is the first element in the periodic table and is the most abundant element in the solar system. It has three naturally occurring isotopes ^1H = Protium, ^2H = Deuterium and ^3H = Tritium, out of which the heaviest one (^3H) is radioactive in nature. Hydrogen (H_2) being a clean alternative energy carrier has potential to play an important role in the future energy scheme reducing the dependence on fossil fuel. Hydrogen energy can be harnessed mainly by two ways:

(a) *production of energy from hydrogen using fuel cell technology and*

(b) *from hydrogen isotopes (deuterium and tritium) using nuclear fusion technology.*

Fuel cells are electrochemical devices that can generate power with high efficiency and low environmental impact. A fuel cell operates at an efficiency of 50-60% while the efficiency for steam power plant is approximately 35% [6]. Therefore the use of H_2 in fuel cells could also prolong the life of fossil fuels available today and reduce the greenhouse gas emission. In addition, the nuclear fusion reactors are also capable to meet the global energy demand by utilizing the energy released from D-T fusion cycle in a controlled manner [7]. The prime fuel in fusion reactors is deuterium and tritium. The production of energy from the fusion reactors involves no hazardous chemical and less radioactive waste emission to the environment.

Besides this, hydrogen is also used in internal combustion engines to power vehicles, propulsion of spacecraft and for passenger vehicles and aircraft. In addition to energy applications, pure hydrogen is a valuable industrial material and is consumed in the order of billions of cubic meters per year. Hydrogen is used for hydrogenations in the chemical process industry, iron ore reduction, as a blanket gas for brazing [8, 9]. It also finds application as a reducing gas during the sintering and annealing of metals to prevent oxidation and nitriding and as a coolant for power station. In semiconductor industry, it acts as generators and as a carrier gas during the doping of silicon wafers or chemical vapour deposition (CVD) [10]. Presently, a major hydrogen sink is the hydro-desulfurization of fuels [11, 12]. It is also used in scientific and military balloons and as a rocket fuel. *However, all these applications demand high pure hydrogen for better efficiency and durability of the process.*

1.1.1. Hydrogen energy using fuel cell technology

Fuel cell is a device that electrochemically converts the chemical energy contained in a fuel into electrical energy. All fuel cells are based around a central design [13] using two electrodes separated by a solid or liquid electrolyte that carries electrically charged particles between them. Hydrogen is the basic fuel in most of the fuel cells which is supplied from an external source to the anode and oxygen/air is used as an oxidant at the cathode. The oxidation of the hydrogen takes place electrochemically to form water [14]. The general reaction taking place in most of the fuel cell is represented as:

$$H_2 + ½O_2 \rightarrow H_2O + \text{electric energy} + \text{heat} \qquad (1\text{-}1)$$

During this process, electrons are released and flow through an external circuit as an electric current. A catalyst is often used to speed up the reactions at the electrodes. A schematic representation of fuel cell is given in Figure 1.1. Fuel cells are generally classified according to the nature of the electrolyte used. The different types of fuel cells include: (1) polymer electrolyte membrane fuel cell (PEMFC), (2) alkaline fuel cell (AFC), (3) phosphoric acid fuel cell (PAFC), (4) molten carbonate fuel cell (MCFC), and (5) solid oxide fuel cell (SOFC).

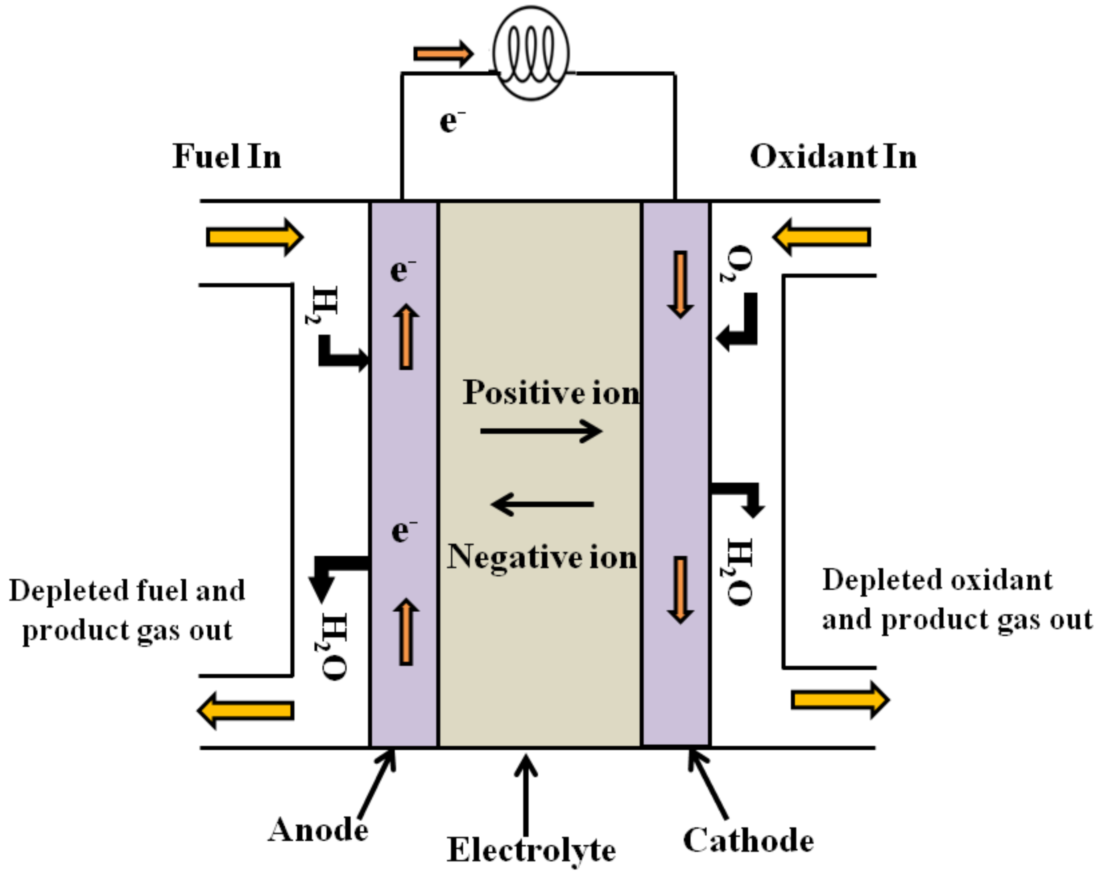

Figure 1.1. Schematic representation of a fuel cell

The physicochemical and thermo-mechanical properties of materials in the cell components (electrodes, electrolyte etc.) indicate the life of the cell [15]. The presence of impurities in the fuel affects the cell components thereby decreasing the performance and durability of a fuel cell. Therefore most of the fuel cells like alkaline fuel cell, polymeric-electrolyte-membrane fuel cell and phosphoric-acid fuel cell require ultra pure hydrogen to be supplied to the anode.

It has been reported that presence of a ppm level impurity in the fuel (H_2) decreases the performance and durability of the fuel cells [16]. The presence of impurities interferes in the electrochemical reaction of the fuel cells and affects its kinetics [17]. Depending on the trace substances in fuel (CO, CO_2, H_2S, NH_3 etc.) they can poison the catalyst or restrict the mobility of the ions in the electrolyte material by reacting with it. Some of the examples of performance loss of fuel cells due to the presence of impurities in fuels are given below.

(a) *The presence of* CO_2 *in the fuels of AFCs results in a considerable performance loss. The negative impact of* CO_2 *arises from its reaction with* $OH^{(-)}$ *ions*:

$$CO_2 + 2OH^{(-)} \rightarrow CO_3^{(2-)} + H_2O \qquad (1\text{-}2)$$

The above reaction produces following effects [18]:

(i) Considerable reduction in $OH^{(-)}$ concentration which affects the reaction kinetics.

(ii) The formation of carbonate increases the viscosity of the electrolyte resulting in lower diffusion rate, lower limiting current and reduced electrolyte conductivity.

(iii) The precipitation of carbonate salts in the porous electrode reduces the mass transport phenomena.

The cumulative effect of all these affects the overall performance of the fuel cell [19].

(b) Similarly, the presence of CO and S-containing compounds in a H_2-rich fuel of PEMFCs and PAFCs has a significant effect on the performance of anode.

(i) CO poisons Pt electrode by blocking the active sites. The absorption of two molecule of CO replaces one H_2 molecule. The blocking of active sites by CO has a major influence on the oxidation of hydrogen [20-21].

(ii) The presence of hydrogen sulfide (H_2S) in fuel gas can also poison the fuel cell catalyst [22] and rapid cell failure occurs when fuel gas contains more than 50 ppm H_2S. Experimental studies by Chin et al. [23] indicate that H_2S adsorbs on Pt electrode and blocks the sites available for H_2 oxidation. Following reactions are proposed for H_2S reaction on Pt electrode surface.

$$Pt + HS^- \rightarrow Pt\text{-}HS_{ads} + e^- \tag{1-3}$$

$$Pt\text{-}H_2S_{ads} \rightarrow Pt\text{-}HS_{ads} + H^+ + e^- \tag{1-4}$$

$$Pt\text{-}HS_{ads} \rightarrow Pt - S_{ads} + H^+ + e^- \tag{1-5}$$

The extent of catalyst masking by H_2S increases with increasing H_2S concentration, electrode potential, and exposure time. A synergistic effect between H_2S and CO negatively impacts cell performance.

(c) Other than CO and H_2S, nitrogen compounds (e.g., NH_3, HCN, NO_X) are also harmful for PAFCs.

Nitrogen present in the fuel may react with the hydrogen in presence of the catalytic surface to form NH_3. The formed NH_3 or residue present in the fuel or oxidant gases reacts with H_3PO_4 to form a phosphate salt, $(NH_4)\ H_2PO_4$, which decreases the O_2 reduction [24].

$$H_3PO_4 + NH_3 \rightarrow (NH_4)H_2PO_4 \tag{1-6}$$

(c) Sulphur compounds and halides in low ppm concentrations in fuel gas are detrimental to MCFCs.

The principal sulphur compound that has an adverse effect on cell performance is H_2S. The adverse effects of H_2S and the halide compounds occur because of:

(i) Chemisorption of H_2S on Ni surfaces to block active electrochemical sites.

(ii) Oxidation of H_2S to SO_2 in a combustion reaction, and subsequent reaction with carbonate ions in the electrolyte.

(iii) Halogen-containing compounds can lead to severe corrosion of cathode material.

(iv) Reaction of HCl and HF with molten carbonates (Li_2CO_3 and K_2CO_3) forms CO_2, H_2O, and the respective alkali halides, which are responsible for the decrease in the current drawn from the cell.

The foregoing examples suggest that presence of impurities in H_2 has a negative influence on the performance and the functionality of the fuel cells. Thus, fuel cell requires ultrapure hydrogen to prevent catalyst poisoning while enhancing its durability and efficiency.

1.1.2. Hydrogen energy using fusion reactor- International thermonuclear experimental reactor (ITER)

Advanced nuclear technology like nuclear fusion is considered as an alternative resource of nuclear energy. Nuclear fusion reactor has less environmental impact and safe in waste management. Hence, it is fetching global attention in recent years [25].

Fusion is a process of combination of two lighter nuclei to form one or more different heavier nuclei and subatomic particles (neutrons and/or protons). The difference in mass between the products and reactants is manifested in the form of energy according to Einstein’s relation:

$$E= mc^2 \tag{1-7}$$

where, m is the mass defect and c is the velocity of light. Fusion reactions constitute the fundamental energy source of stars, including the Sun [26]. The energy generated during a nuclear fusion process is quite higher than that of fission and other mode of energy production process. Reactions between deuterium and tritium are the most important fusion reactions for controlled power generation [27].

$$D + T \rightarrow \alpha + n \qquad Q = 17.6 \text{ MeV} \tag{1-8}$$

The D-T fusion has high reaction cross section and energy yield of the reactions is 17.6 MeV. Helium and neutron are produced from the fusion reaction and the total energy is shared between the products (He = 3.5MeV and n = 14.1MeV). Other fusion reactions involving elements with an atomic number above two can be used, but only with much greater difficulty due to increase in Coulomb barrier. A schematic representation of a D-T fusion is shown in Figure 1.2. International Thermonuclear Experimental Reactor (ITER) has been proposed to study the feasibility of D-T fusion reaction to produce energy [28]. The mega project ITER, is an experimental fusion reactor being constructed at Cadarache, France.

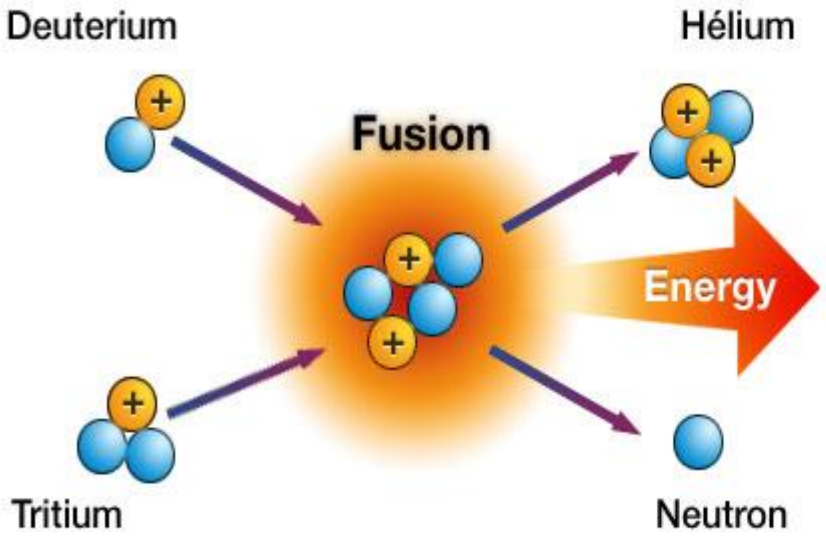

Figure 1.2. Schematic of D-T fusion reaction

ITER will be the first fusion device to produce energy from D-T fusion, maintaining fusion for long periods of time. The specific technical objectives of ITER science and technology programme include [29]:

a) Produce 500 MW of fusion power from input power of 50 MW.
b) Demonstrate the availability and integration of essential fusion technologies for fusion reactor.
c) Achieve self-sustainable D-T plasma (fuelling and fuel processing).
d) Test tritium breeding module concept.
e) Safe operation of the fusion reactor.

The various features such as steam generator, turbine and current generator will be the same as in conventional nuclear fission or fossil-fuelled power plants, except the use of fusion reactions to generate heat. A schematic diagram of the proposed fusion power plant is shown in Figure 1.3. The reactor is composed of a support structure, a cryostat with superconducting magnet, a vacuum vessel and the first wall being an integrated blanket. The blanket includes structural materials, a neutron absorber, and high heat flux. In the plasma confinement zone, the deuterium and tritium fuel will burn and the energy will be released in the form of heat. The heat energy will be utilized to generate electricity in the conventional method. To sustain the fusion reaction, it is required to supply deuterium and tritium to plasma. Deuterium has a natural abundance of approximately 0.0156% (or on a mass basis 0.0312%) of all the naturally occurring hydrogen in the oceans. It can be produced from heavy water by electrolysis.

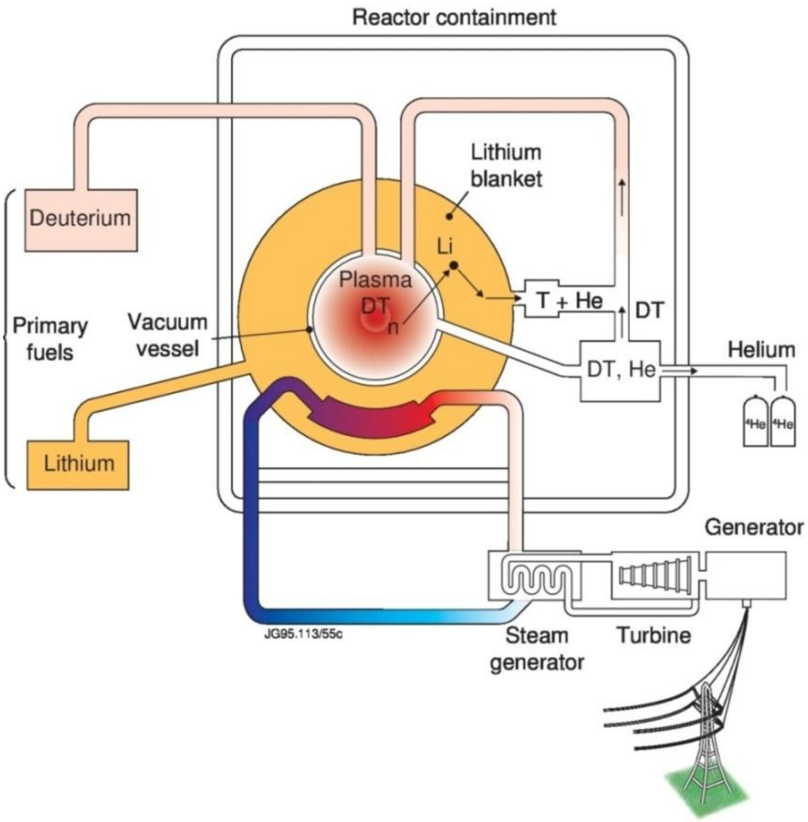

Figure 1.3. Schematic of proposed nuclear fusion power plant based on D-T fusion (Reprinted with permission from [30] © EUROfusion)

The heavy water is produced from normal water by the Girdler sulphide process, ammonia-hydrogen process, distillation methods. However, the natural abundance of tritium is very low (i.e. 1TU which is 1 atom per 10^{18} atoms of hydrogen) [31]. Hence, in the proposed design of ITER, tritium will be produced in situ in the fusion reactor by the interaction of the neutrons escaping the plasma with the breeder blanket material. However, the breeder blanket has two roles to breed tritium and to convert neutron energy to heat [32]. Lithium based ceramic materials has been identified to breed tritium. The low nuclear binding energy makes lithium a suitable material for tritium breeding [33]. The tritium production nuclear reaction is given below:

$$^{6}Li + n = {}^{4}He + {}^{3}H + (4.8\ MeV) \quad (1\text{-}9)$$

$$^{7}Li + n = {}^{4}He + {}^{3}H + n \quad (1\text{-}10)$$

A schematic diagram of fusion fuel cycle is shown in Figure 1.4. The main processes involved in fusion fuel cycle are [34]: a) storage and delivery of deuterium and tritium, b) fuelling deuterium and tritium to the plasma chamber, c) tritium extraction from the breeder, d) plasma exhaust treatment, e) isotope separation and f) water detritiation.

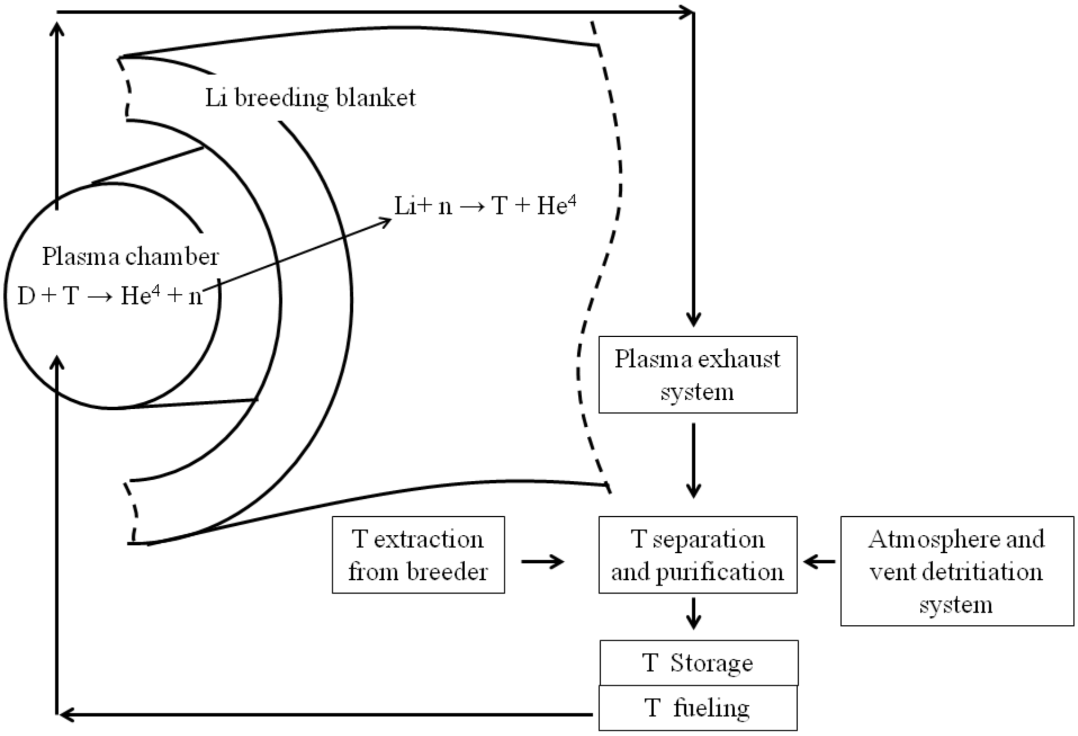

Figure 1.4. Schematics of fusion fuel cycle [34]

The tritium breed in the solid breeder blanket material (Li_4SiO_4) will be extracted by passing H_2 (0.1%) added helium sweep gas through the blanket. Hydrogen gas will be added to the helium sweep gas to enhance the tritium release by isotopic exchange. The sweep gas containing the bread tritium will be sent to the blanket tritium recovery system (BTR), and tritium will be separated from sweep gas [35]. On the other hand, un-reacted fuel and helium produced by nuclear fusion reaction are exhausted from the plasma exhaust. Thus, the plasma exhaust stream mostly contains hydrogen isotopes (Q_2: Q = H, D, T) with a few to possibly 20% impurities such as: CQ_4, CO_2, CO, O_2, Q_2O, N_2, NQ_3 and He [36]. These gases are generated from the interactions of plasma with the first wall of the chamber. *These impurities present in the fuel degrade plasma conditions and hence need to be removed before further processing in the* *fusion fuel cycle. Therefore hydrogen purification technologies have immense importance for the extraction of tritium from the breeding blanket, plasma exhaust treatment and water detritiation in fusion fuel cycle.*

1.2. Hydrogen purification methods

Owing to the large demand of high pure H_2 in the fuel cells, hydrogen isotopes in fusion fuel cycle and several large scale industrial applications, an efficient hydrogen purification system is required. Together with the hydrogen production, purification is also important for proper implementation of future energy scheme [37].

Hydrogen is produced industrially from coal or biomass using the steam-methane reforming (SMR). Steam reforming reaction is the endothermic conversion of methane and water vapour into hydrogen and carbon monoxide. The process typically occurs at temperatures of 350^{o} C. Similarly, hydrogen is also produced from partial oxidation of natural gas and gasification of coal. Each of these product gases contains CO, which can be further converted to CO_2 and H_2 through the water-gas shift reaction at 200^{o} C [38-42].

Steam methane reform reaction: $CH_4 + H_2O + \text{heat} \rightarrow CO + 3H_2$ (1-11)

Partial oxidation of natural gas: $CH_4 + 1/2O_2 \rightarrow CO + 2H_2 + \text{heat}$ (1-12)

Coal gasification: $C(s) + H_2O + \text{heat} \rightarrow CO + H_2$ (1-13)

Water gas-shift reaction: $CO + H_2O \rightarrow CO_2 + H_2 + \text{heat}$ (1-14)

Table 1-1 summarizes the various hydrogen production sources and impurities in the product stream. Regardless of the method used for hydrogen production, there will be demand for a cost effective and efficient means to separate it from impurities. There are several techniques available for separation and purification of hydrogen depending upon the process requirement, scale of production, nature of feed gas etc.

Table 1-1. Impurities in hydrogen production process

Hydrogen Source	Impurities
Electrolysis of water	O_2, N_2
Steam reforming gas	CO, CO_2, CH_4
Petroleum refining	CO_2, CH_4 and higher hydrocarbons
Ammonia purge gas	NH_3, N_2
Coke oven gas	N_2, CO, CO_2, O_2, hydrocarbons

Hydrogen can be purified through one or a combination of the methods depending upon the requirement: Four major techniques for purification of hydrogen are:

a) Pressure swing adsorption (PSA)

b) Fractional/cryogenic distillation

c) Metal hydride separation

d) Membrane separation

PSA and fractional/cryogenic distillation and membrane purification technologies are widely used in commercial operation scale for purification of hydrogen and its isotopes from impurity gas stream. A brief description of each process is given below.

1.2.1. Pressure swing adsorption

Pressure swing adsorption (PSA) is a well-known gas purification technology. It is based on differences in the physical binding forces of gas molecules to adsorbent material such as active carbon and zeolite. The bonding force between the gas molecules and the adsorbent material is dependent on the nature of gas, partial pressure of the gas, nature of adsorbent material used and temperature of operation etc

[43]. A gas having low polarity like hydrogen is non-adsorbable as compared to molecules like N_2, CO, CO_2, hydrocarbons and water vapour with the binding material. Consequently, these impurities can be adsorbed from a hydrogen containing stream and high pure hydrogen is recovered. The PSA process works under isothermal condition and uses the effect of alternating pressure and partial pressure of gases to perform adsorption and desorption. The common gas streams containing hydrogen and various impurities used in this application are [44-46]:

(a) The steam-methane reformer and water-gas shift reactor gas containing 70–80% H_2, 15–25% CO_2, 3–6% CH_4, 1–3% CO, and trace N_2.

(b) The refinery off-gas containing 65–90% H_2, 3–20% CH_4, 4–8% C_2H_6, 1–3% C_3H_8 and PPM level H_2S).

PSA is a robust and regenerative technology. It is the most used process in the refineries for the large scale production of pure hydrogen. A continuous flow of hydrogen with no pressure fluctuations or pulsing effects can be achieved. However, the limitations are the high cell replacement cost and huge quantity of hydrogen loss during the regeneration of the molecular sieves.

1.2.2. Cryogenic Separation

Cryogenic distillation is a promising method for separation of hydrogen from the gas mixture containing CO_2, CH_4, H_2O, CO etc. It is the process of selectively purifying gases by liquefying the gases at various liquefaction temperatures [47]. The process requires small heat exchangers to turn any liquid input into a gas before it went through separation. This process of separation of impurities from the feed stock operates on the basis of cryogenic adsorption of gases. Hydrogen gas is passed into the system at high pressure and enters a series of heat exchangers and adsorbent beds to produce pure hydrogen gas. Silica gel is the main adsorbent material used, which is submerged in liquid nitrogen during the process. Cryogenic separation can tolerate a wider range of hydrogen content in the feed gas. The main drawback of this process is consumption of much liquid nitrogen. Huge amount of energy is also required to compress the gases which, enhances the operation cost.

1.2.3. Metal hydride separation

Metal hydrides have been widely studied for storage of hydrogen and its isotopes but they can also be employed for the efficient purification of hydrogen isotopes from a mixture. The process of purification using metal hydrides is based on the selective adsorption of hydrogen by several metals used for hydrogen storage [48]. Some of the properties such as, hydrogen storage capacity, distinct plateau pressure, faster reaction kinetics, anti-poisoning property, long cycle life of the material are crucial for their application in hydrogen purification [48]. Metal hydride separation method can be used if the hydrogen content in the feed gas stream is greater than 50 to 60%. The composition of feed gas and its impurities content have a great impact on the efficiency of hydrogen purification using metal hydrides [49]. Even a small amount of poisoning gas in the feed will change the rate of hydrogen absorption kinetics thereby reducing the efficiency of the reactor. The hydrogen product purity of 99.9% and recovery of about 81 ~ 86% can be achieved using the metal hydrides. However, the use of metal hydrides is limited to a certain feed gases only. For example the coke oven gas contains a variety of impurities, which may lead to metal hydride poisoning. Hence, its purification by metal hydride is limited. Hydrogen produced by electrolysis of water has an original purity of about 98%, becomes ideal feed gas for the metal hydride separation process. Though the process is utilized for purification of hydrogen but low recovery rate and limited use of feed gas limits its wide spread use [48, 50].

1.2.4. Membrane separation

Membrane purification processes are considered to be one of the most promising technologies for the production of high-pure hydrogen. This process is energy efficient and continuously operated process. This technique is important because, hydrogen production could be coupled with membrane reactor so that the reversible reforming reaction shifts to the right, increasing hydrogen conversion [51].

In a broad sense, membrane is a physical barrier which selectively allows certain components to pass through it by resting the others. A typical membrane separation process is given in Figure 1.5.

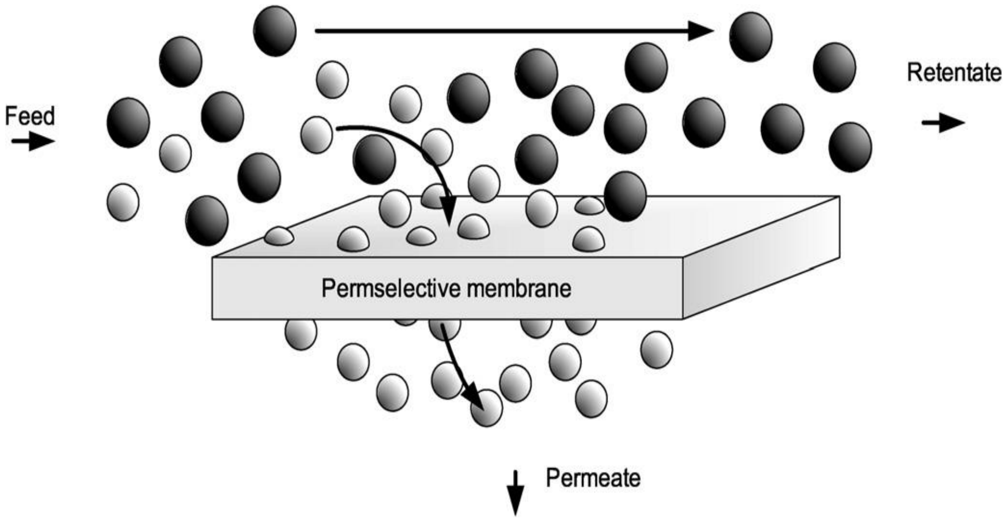

Figure 1.5. Membrane separation process

Considering purification of gaseous H_2, either H_2 molecules or impurities will be selectively permeated through the membrane. The membrane diffusion or separation is governed by any of these five mechanisms [52]: (a) Knudsen diffusion, (b) surface diffusion, (c) capillary condensation, (d) molecular sieving and (e) solution diffusion mechanism. The contribution of these mechanisms in a specific material culminates the overall performance and efficiency of the membrane. An ideal membrane is required to have high hydrogen permeability, high thermal and mechanical stability, excellent hydrogen selectivity, improved cyclic life, wide range of temperature and pressure operation, and cost effective way of fabrication [53]. Each of these processes has advantages and disadvantages for purification of hydrogen isotopes. However the most promising method is the membrane separation due to its ease of operation, high purification efficiency, and independent of the feed gas composition. A comparison of different types of hydrogen purification systems is given in Table 1-2.

Table 1-2. Comparison of different types of hydrogen purification techniques

Separation Techniques	Principle of operation	Feed gas composition	Produced gas purity (%)	Recovery	Comments
Pressure swing adsorption	Selective adsorption of impurities from gas stream	Any gas stream containing hydrogen	99.99	70-85	Recovery is low as hydrogen is lost during purging
Cryogenic distillation	Partial condensation of gas mixtures at low temperatures	Petrochemical and refinery off gases	90-98	95	Purification step necessary to remove CO_2, H_2S and H_2O
Metal hydride separation	Reversible reaction of hydrogen with metals to form hydrides	Ammonia purge gas and hydrogen produced from electrolysis of water	99.9	75-95	Hydrogen absorption and poisoned by O_2, CO and S
Metallic membrane separation	Selective diffusion of hydrogen through a palladium alloy membrane	Any hydrogen rich feed gas	99.999	~99	Sulphur containing compound impair the permeability
Solid polymer electrolytic cell	Electrolytic passage of hydrogen ions across a solid polymer membrane	Refinery off gases and ammonia purge gas	99.8	95	Sulphur containing compound poison the electro-catalysis

1.3. Membrane separation methods

The membranes can be classified in to several categories depending on the composition of the membrane material as: Polymeric membranes, Carbon membranes, Inorganic porous membranes (zeolites, glasses, and ceramics), dense metallic membranes (pure metals or alloys). Depending upon the morphology of the membrane the transport mechanism, and selectivity varies. A comparison of different types of membrane separation techniques is given in Table 1-3.

Table 1-3. Properties of hydrogen selective membranes

Properties/ membrane process	Polymeric membrane	Inorganic porous membranes	Dense metallic membranes	Porous carbon Membranes
Temperature range (K)	298-393	673-873	473-873	873
H_2 selectivity	Low	5-139	> 1000	4-20
Stability Issues	Swelling, compaction,	Stability in H_2O	-	Brittle, oxidizing
Poisoning Issues	HCl, SO_x, CO_2	H_2S, HCl, CO	H_2S	Organic vapours
Materials	Polymers	Silica, alumina, zirconia, zeolites	Palladium alloy	Carbon
Transport Mechanism	Solution diffusion	Molecular sieving	Solution diffusion	Surface diffusion; Molecular sieving

1.3.1. Polymeric membranes

Polymeric membrane technologies are successfully used for large-scale recovery of hydrogen from the feed gas containing impurities. Polymeric membranes can be divided into two major classes: porous and nonporous. Hence the transport of gases through these membranes can occur by different mechanisms. In a porous membrane, molecular diffusion takes place via Knudsen diffusion, surface diffusion, capillary condensation, and molecular sieving. The process of diffusion is largely dependent on the pore size of the membrane and the size of the diffusing molecule. Whereas in nonporous membranes transport through the membrane is controlled by the solution-diffusion mechanism. In this transport process the molecules dissolve in the membrane and then diffuse through the membrane. The diffusion of molecules through the membrane is driven by a gradient of chemical potential across the membrane. Since the process is controlled by solution-diffusion mechanism, the permeability is dependent on both the diffusivity and solubility of the molecules in the membrane. The major concern in polymeric membranes is their selectivity. Membranes with improved selectivity and productivity are always desired. Although the polymeric membrane is able to deliver hydrogen with a reasonable rate and cost effective mode, the selectivity and recovery is poor. Mixed-matrix membranes that incorporate inorganic, highly selective particles into a polymeric membrane improve the performance of the polymer. However the polymeric membranes cannot be applied at high temperature applications. Operating temperatures are limited to 90-100°C. Another major problems associated with the polymeric membranes is their low chemical resistance to HCl, SOx, CO_2. These membranes have very week mechanical strength, and high sensitivity to swelling and compaction [54].

1.3.2. Carbon membranes

Carbon membranes are of two types: carbon molecular sieving (CMS) and surface diffusion membranes. Molecular sieving membranes are promising both in terms of separation properties and stabilities. In the presence of some trace amount of organic vapours or strong adsorbing species in the feed gas, the performance of these membranes deteriorates. Carbon membranes can be used in non-oxidizing environments with temperatures in the range of 500-900°C. A disadvantage of carbon membranes is that they are brittle and therefore difficult to package if the membrane surfaces become larger.

1.3.3. Inorganic porous membranes (zeolites, glasses, and ceramics)

These membranes can be porous ceramic membranes, thin zeolite sheets or porous glass membranes. Porous ceramic membranes are usually made of alumina, zirconia, titania, or silica. Depending on the components to be separated, the selectivity can reach values up to 140. Operating temperatures for the porous ceramic membranes are within the range 200-600 °C. One of the issues is limited stability in atmospheres containing steam, CO_2, H_2S [55]. Membranes made up of zeolite have channels inherent in their crystal structure and act as natural molecular sieves. However, achievable separation of small molecules is limited and fabrication of large thin zeolite plates is difficult. Depending on the pore size, glass membranes can be subdivided into micro porous (pores below 2 nm) and mesoporous (pores 2-5 nm). Micro porous membranes have higher selectivity yet lower fluxes. Both membrane types are usually produced from silica using the leaching manufacturing process. Glass membranes are not preferable for hydrogen separation due to their low selectivity.

1.3.4. Dense metallic membranes

Dense metallic membrane technology is the best ever technique for purification of hydrogen isotopes. The metals which are most suitable for H_2 separation membranes typically have high H_2 permeability, high diffusivity or solubility, and good thermal stability at elevated temperatures. Most of the used metallic membranes are based on palladium and its alloys [56].

1.4. Hydrogen permeation through palladium based metallic membranes

For the first time in 1866, Thomas Graham demonstrated the diffusion of hydrogen through heated palladium tubes [57]. Successively, several attempts were made to explore the utilization of selective permeability of hydrogen in palladium membranes in industrial process. Both supported composite and unsupported membranes have been extensively explored for the purification of hydrogen and its isotopes in several applications. Pd-based membranes have been used in the membrane reactors for production of high pure hydrogen in biomass reform reactions. Besides Pd, several other pure metals have been investigated for H_2 permeability measurements [58, 59]. Pure Rh and Ir membranes showed H_2 permeability comparable with pure Pd [59]. Similarly V and Ta foils have higher permeability compared to Pd. However the surface oxidation of these metals under ambient conditions retards the H_2 permeability thus limits their practical applications in membrane purification systems.

1.4.1. Theory of metal-hydrogen interaction

Hydrogen interacts with almost all metals in the periodic table due to the presence of an unpaired electron. The metal react with hydrogen under certain temperature and pressure to form metal hydride. Reaction between metal and hydrogen is a complex heterogeneous gas-solid reaction. The overall reaction can be expressed as:

$$M(s) + x/2\ Q_2\,(g) = MQ_x(s) + \Delta H \qquad (1\text{-}15)$$

where, M denotes the metal, Q denotes the hydrogen isotopes (H, D and T), and ΔH is the heat of reaction. The forward reaction i.e. formation of metal hydride is exothermic whereas the backward reaction i.e. dehydriding reaction is endothermic. However, the reaction takes place in a number of steps and each step has its own physical significance. The metal-hydrogen reaction takes place by a physisorption followed by a dissociative chemisorption. After hydrogen atom is chemisorbed on the surface of metal it diffuses to the bulk forming a hydride phase. In 1932 Lennard-Jones proposed a one dimensional potential energy diagram [60] for the dissociative adsorption of hydrogen molecule on the metal surface shown in Figure 1.6. The curve leveled as II in the figures represents the potential energy of hydrogen molecule as a function of distance from the surface. The zero reference is taken when the molecule is at infinite distance from the surface as there is no interaction between the metal and hydrogen. The curve leveled as I is the potential energy curve as a function of distance for hydrogen atom. It can be seen from the Figure 1.6. that even at infinite distance from the surface, hydrogen atom possess a finite amount of potential energy. The difference between the potential energy between the H_2 molecule and H-atom is equal to the dissociation energy of hydrogen molecule, 436 kJ/mol H_2 [31]. As the H_2 molecule comes closer to the metal surface there is a small potential well representing the physisorption of the molecule on the surface. This is caused by van der Walls force of attraction and is characterized by a low heat of adsorption in the range of 0-40 kJ/mole H_2. This leads to physisorbed state of hydrogen, at around one molecular hydrogen radius distance (~ 0.2 nm) from the metal surface. If the molecule moves closer to the surface, the potential energy will increase due to repulsion. At some point, the potential energy of the H_2 molecule will intersect with the potential energy of the H-atom. The point of intersection is termed as the activation barrier from physisorbed state to chemisorbed state. Hence, the hydrogen molecule has to overcome an activation barrier for dissociation of H-H bond and formation of the metal-hydrogen bond. The height of the activation barrier depends on the surface elements involved. If intersection is at a potential energy larger than zero relative to gas phase H_2, dissociation is said to be non-activated and the height determines the activation barrier shown in Figure 1.6(a). In this case, only the fraction of H_2 molecules having the energy larger than the activation barrier will be able to dissociate. If intersection is located at approximately zero potential energy, dissociation is said to be activated shown in Figure 1.6 (b). After dissociation, the hydrogen atoms find a potential energy minimum which corresponds to the H atoms being bonded to the metal surface (chemisorption). The nature of chemisorption depends on the relative bond strength of H-H and M-H bonds.

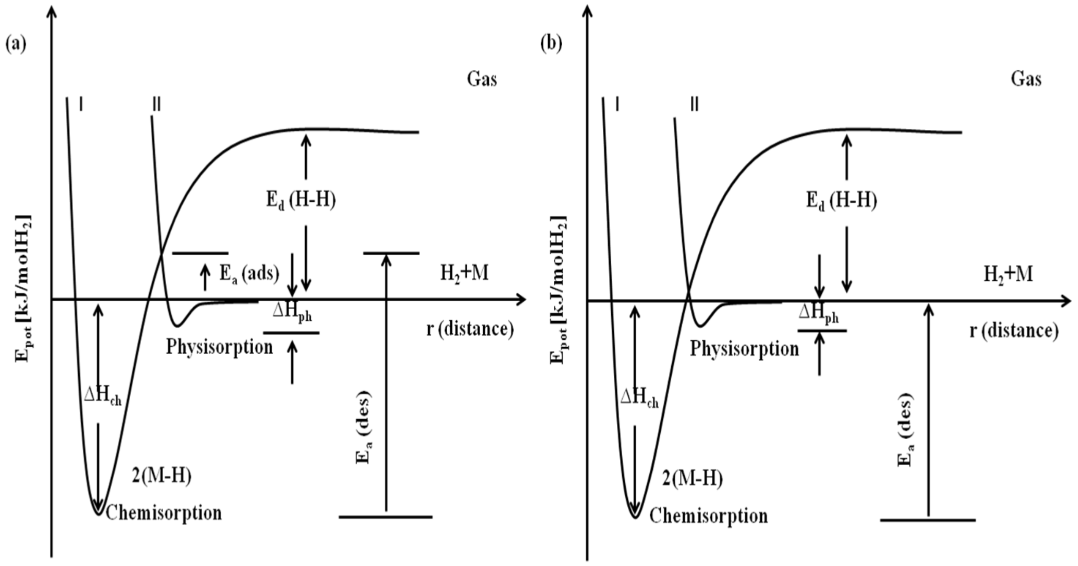

Figure 1.6. Schematics of Lennard-Jones potential energy diagram for metal hydrogen interaction, (a) non activated adsorption, (b) activated adsorption

This process is said to be exothermic if the H-M bond is stronger than the H-H bond and endothermic if the H-H bond is the stronger. After chemisorption, the hydrogen atoms can penetrate the first metal atomic layer into the subsurface through an activated process from which it can diffuse into the bulk of the metal.

1.4.2. Thermodynamics of Metal-Hydrogen interaction

Thermodynamic properties of metal-hydrogen systems are of great importance for their practical applications. The thermodynamic aspect of hydride formation in metals is best represented by a pressure-composition isotherm (PCI). Combination of several PCIs at different temperatures is known as PCT. Schematic representation of a PCT is shown in Figure 1.7.

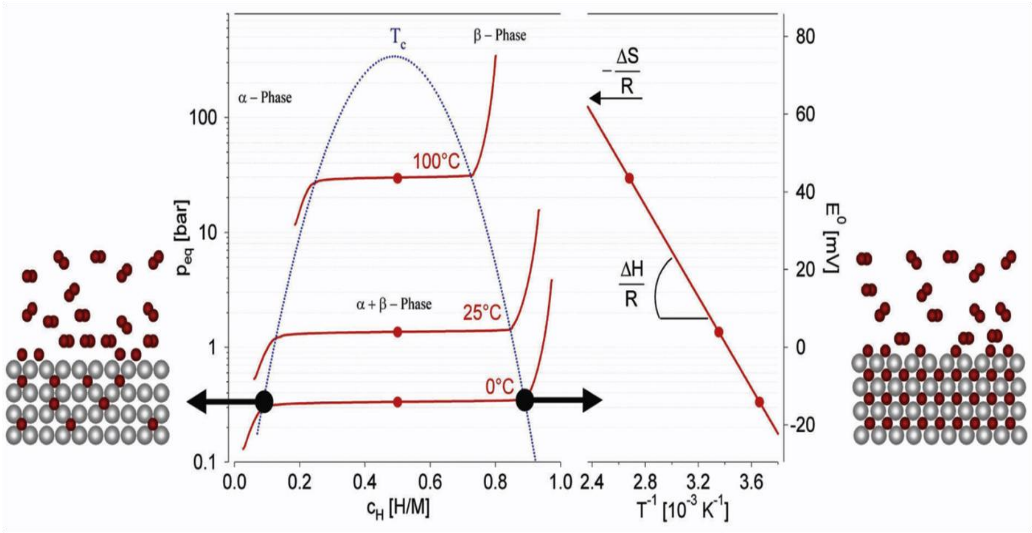

Figure 1.7. Schematic of pressure-composition isotherms (PCIs) and van't Hoff plot [61]

In the PCT diagram, each PCI shows three distinct phases namely α-phase, α + β phase and β-phase. When some hydrogen is dissolved in the host metal, it forms a solid solution, known as the α-phase. When, the maximum solubility of hydrogen in the α-phase is reached, nucleation and growth of the hydride phase (β-phase) occurs [62]. The region in a PCI where both the α-phase and β-phase co-exist is known as the plateau region. The plateau continues as long as there are two distinct phases, according to Gibbs phase rule [63].

$F = C - P + 2$ (1-16)

Where, C is the number of components and P is the number of phases. The three metal-hydrogen equilibrium phases is described by three different reactions:

$M(s) + x/2\ Q_2\ (g) = MQ_x\ (s)$ (1-17)

$MQ_x\ (s) + (y-x)/2\ Q_2(g) = MQ_y\ (s)$ (1-18)

$MQ_y + \delta/2\ Q_2\ (g) = MQ_{y+\delta}\ (s)$ (1-19) where, M denotes the metal, Q denotes the hydrogen isotopes (H, D and T). With increase in temperature, hydrogen solubility range of α and β phases increases. And the miscibility gap between the two phases becomes narrow. At a certain critical temperature (T_c) the miscibility gap disappears and the α-phase continuously coverts to β-phase. Above the critical temperature the plateau region disappears. The pressure corresponding to the α + β phase region is called as equilibrium plateau pressure. This plateau pressure strongly depends on temperature and is related to the changes in enthalpy and entropy of the metal-hydrogen reaction. Thermodynamics of formation of a metal hydride is calculated from the equilibrium pressure corresponding to α + β phase region using van't Hoff relation [64]. In most of the metal-hydrogen systems, the PCIs show a sloping plateau. This phenomenon may be arising due to surface heterogeneities, impurities, particle size and stresses in the system [65]. Hysteresis is observed in many of the metal hydrogen systems where, the plateau pressure corresponding to absorption is higher than that of desorption PCI.

The thermodynamic parameters of a metal hydride system are calculated from the equilibrium plateau pressure data. The Gibbs energy change and the equilibrium partial pressure are related by the equation:

$$\Delta_r G_Q = \Delta_r G^o_Q + RT \ln K_P \qquad (1\text{-}20)$$

For bi-phasic (α + β) region at equilibrium, $\Delta_r G_Q = 0$, which implies that:

$$\Delta_r G^o_Q = - RT \ln K_P \qquad (1\text{-}21)$$

K_P for M-Q reaction is given as:

$$K_P = 1/\left(P_{eq}\left(Q_2\right)\right)^{x/2} \qquad (1\text{-}22)$$

We know, $\Delta_r G^o_Q = \Delta_r H^o_Q - T\Delta_r S^o_Q$ (1-23)

Substituting the value of $\Delta_r G^o_Q$ and rearranging for one mole of hydrogen the relation can be written as:

$$-RT \ln P_{eq}(Q_2) = \Delta_r H^o_Q - T\Delta_r S^o_Q \qquad (1\text{-}24)$$

$$\text{Or, } \ln P_{eq}(Q_2) = -\Delta_r H^o_Q / RT + \Delta_r S^o_Q / R \qquad (1\text{-}25)$$

where, R is the gas constant (8.314 J/mole·K) and T is the absolute temperature. The equilibrium plateau pressures at different temperatures are used to construct the van't Hoff plot ($\ln P$ vs $1/T$). The enthalpy ($\Delta_r H^o$) and entropy $\Delta_r S^o$ of reaction can be evaluated from the slope and intercept of van't Hoff plot. [64].

1.4.3. Hydrogen permeation through metallic membranes and factors affecting permeation.

Hydrogen permeation through the metallic membranes takes place by solution-diffusion mechanism. This proceeds via the formation of M-H_x solid solution. The permeation of Q_2 (Q=H, D, T) through these membranes is a concentration driven process and takes place in several steps [66]:

a) physisorption of H_2 molecule on the surface of the metal;
b) irreversible dissociative chemisorptions of H_2 on the metal surface;
c) dissolution of atomic hydrogen in the bulk of the metal;
d) diffusion of atomic hydrogen through the interstitial sites toward the opposite side;
e) recombination of atomic hydrogen to form hydrogen molecules at the gas/metal interface;
f) desorption of hydrogen molecules to the gas phase from the surface.

The diffusion of hydrogen in the metallic membranes takes place by quantum mechanical hooping of atomic hydrogen from one interstitial site to other. In case of

Pd/Pd-alloy membranes having f.c.c crystal structure hydrogen atom preferentially occupies the octahedral site. Hence the diffusion of H in these membranes is mostly due to the octahedral-octahedral jump [67].

Diffusion of hydrogen through these membranes follows Fick's law. At a fixed temperature, the hydrogen permeation flux through a dense membrane can be expressed by Fick's law as:

$$J = -D \times (\Delta C) / L \qquad (1\text{-}26)$$

where, D is the diffusion coefficient (m^2/s) and ΔC is the concentration gradient, and L is the thickness of the membrane.

The concentration dependency on partial pressure of hydrogen is expressed by Sieverts' law [68]:

$$C = K_s p^n \qquad (1\text{-}27)$$

where, K_s is the Sieverts' constant or solubility. When the concentration in Sieverts' law is substituted into Fick's first law, the flux becomes:

$$J = -(D.K_s.\Delta p^n) / L \qquad (1\text{-}28)$$

Or, $J = P_e\,(p_f^n - p_d^n) / L$ (1-29)

where, P_e is the permeability (mol $m^{-1}s^{-1}Pa^{-0.5}$) which is the product of solubility and diffusivity of hydrogen in the metal. In Sieverts' law, solubility of atomic hydrogen in the lattice is taken constant assuming dilute solution and no interaction between hydrogen atoms [68]. However, the hydrogen solubility varies with temperature and pressure. Therefore the value of pressure exponent varies from 0.5-1 depending upon the material and operation condition.

Several factors affect the rate of permeation through the Pd-membranes. The parameters which affect any of the steps involved in hydrogen permeation will have influence on the rate of permeation.

1.4.3.1. Effect of contaminations

Several poisoning species contaminate the surface of the membrane and decreases the rate of permeation. These materials block the active sites available for catalytic dissociation of hydrogen on the surface of the metal and thus slow down the permeation rate. The contaminants include carbon containing compounds, sulphur compounds, chlorine, ammonia, etc. [69]. Sulphur and carbon can segregate on the palladium surface at high temperatures and decreases hydrogen uptake [70]. Hydrocarbons inhibit permeability by either adsorbing on the surface or reacting to form carbonaceous layers on the surface at higher temperatures. In many cases hydrogen sulphide in a high concentration reacts with metals to form metal sulphides on the surface, which is impermeable to hydrogen. Chemisorbed species on the surface increases the activation energy for hydrogen dissociation [71]. One impurity atom may block multiple hydrogen adsorption sites [72, 73]. Unsaturated organic compounds have more effect on hydrogen permeation behavior than other carbon compounds. Chabot et al. [74] found that carbon dioxide and methane had limited effect on the hydrogen permeation rate through a palladium membrane, while Chen et al. [75] observed a 10% reduction in flux in the presence of CH_4 or C_2H_4. Exposure of membrane to certain metallic vapours or chlorine compounds can irreversibly poison palladium, severely decreasing hydrogen permeability [76, 77]. Mercury from a diffusion pump or metals volatilized during thermal treatment of a catalyst can permanently reduce the hydrogen permeability of a membrane by adsorbing on the surface or diffusing into the bulk palladium membrane [78]. Any metallic impurity present or contaminated to the membrane during metal processing or deposition affects the permeability by changing the hydrogen solubility in the matrix.

1.4.3.2. Influence of microstructure on hydrogen permeability

The metal microstructure has a great influence on the hydrogen permeability [79, 80]. Diffusivity of hydrogen through the nano-structured materials (grain size < 50 nm) is greater than the poly crystalline metallic foils. This is because of the higher volume fraction of grain boundaries in the nano-crystalline materials. Some researchers have found that, dislocations, vacancies, and voids in the lattice offer increased resistance to hydrogen permeation [73]. Lattice defects, grain boundaries, and voids acts as traps which, slowdown the hydrogen permeation by increasing the activation energy for diffusion [81-83]. Cold working, phase transition, annealing conditions also causes deformation and strain in the lattice. Metal films deposited by different techniques can be expected to have varying permeation characteristics. Because, different deposition techniques forms films of different microstructure having variation in lattice defects and grain boundaries [84]. Film structure and texture also affects the hydrogen permeation behavior. The texture generated as a result of cold working of the metal can affect hydrogen permeability [85]. Adsorption enthalpy and diffusion of hydrogen through the Pd-membrane depends upon the orientation of the atomic planes. During annealing or hydrogen absorption, rearrangement of planes may occur. Hence, annealing condition, number of hydrogen absorption cycles of the membrane affects its hydrogen permeability [86-89]. Therefore, researchers often encounter an increase or decrease in the hydrogen flux through palladium membrane during start up.

1.4.3.3. Effect of temperature and pressure

Temperature of operation largely affects the hydrogen permeation through Pd-base membranes by affecting the solubility and diffusivity of hydrogen in the metal/alloy. Solubility of hydrogen decreases with increase in the temperature, whereas the diffusivity increases with temperature [66, 90]. The diffusion phenomena predominate over solubility at higher temperature. Hence the rate of permeation which is the combination of solution and diffusion increases with temperature. The permeation of hydrogen through palladium membranes shows Arrhenius type temperature dependency. The permeability with temperature can be expressed as

$$P_e = P_o \exp(-E_a/RT) \qquad (1\text{-}30)$$

Where, P_o is the pre-exponential factor, E_a is the activation energy of permeation, T is the temperature and R is the universal gas constant.

Similarly the pressure on the feed side and permeate side of the membrane are the determining factor of hydrogen permeation. With increase in pressure the solubility of hydrogen in Pd/ Pd-alloy increases. However, at higher pressure the solubility of hydrogen in the metal-hydrogen system shows a non-ideal behavior [91]. Hence, the permeability increases with increase in pressure but follows a non-ideal behaviour at higher pressure.

1.4.3.4. Isotope effect on hydrogen permeation through metallic membranes

Hydrogen isotope effects are more pronounced due to the large difference in relative masses of hydrogen isotopes, as compared to other elements of periodic table. The large isotopic effect in the metal hydrogen system is observed due to the difference in the zero point energies of the three isotopes. The schematic of potential energy curve for hydrogen isotope molecules is shown in Figure 1.8.

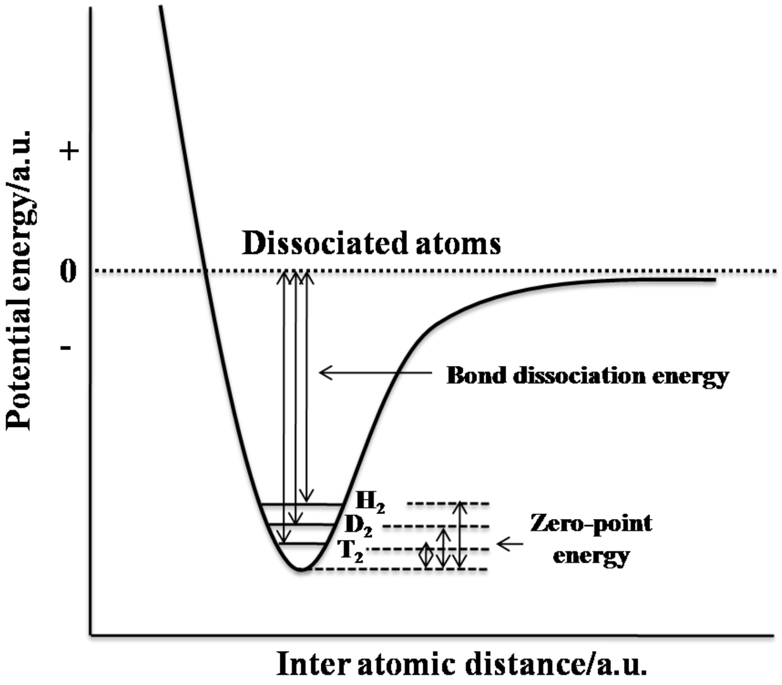

Figure 1.8. Schematic potential energy curve for the hydrogen molecules [38]

It is evident from the figure that heavier isotope (^{3}T) has the lowest zero-point energy whereas that of the lightest (H) is highest, which is in consistence with their reduced masses.

Hydrogen occupies tetrahedral or octahedral interstitial sites in the metal. Hydrogen isotopic effect in metal hydrogen system is best understood by considering the potential wells of gas phase hydrogen/isotopes and hydrogen/isotopes in the in tetrahedral/octahedral interstitial sites of metals/alloys. A schematic comparison of zero-point vibration energies of hydrogen isotopes (H_2 and D_2) in tetrahedral/octahedral positions with that of gas phase molecules is shown in Figure 1.9.

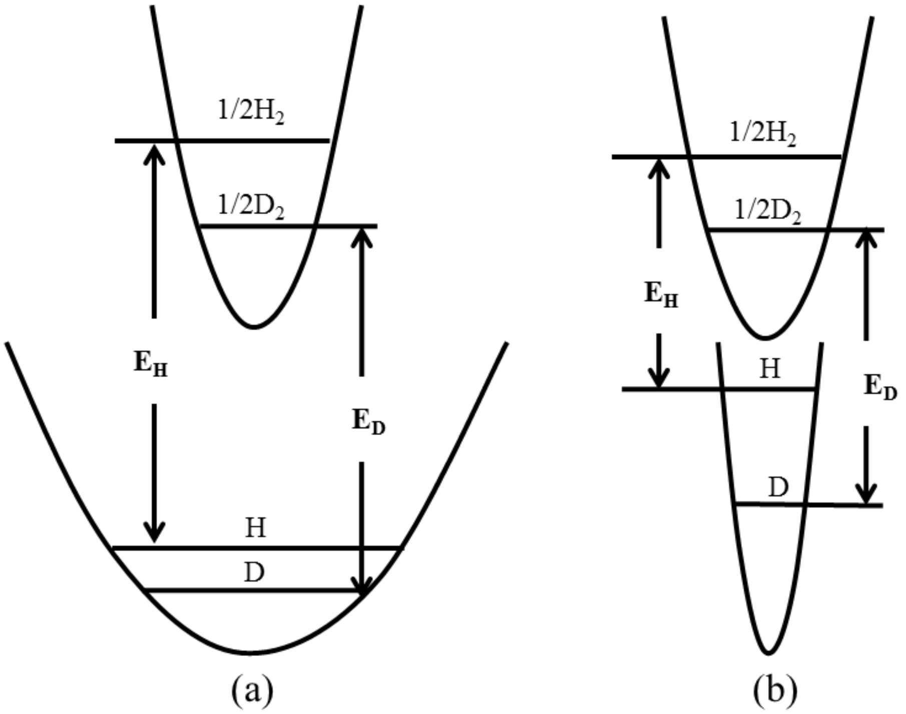

Figure 1.9. The Schematic comparison of the zero-point vibrational energies of hydrogen isotopes in (a) octahedral and (b) tetrahedral interstitial position with that of gas phase molecules (Reprinted from [92], Copyright (1984), with permission from Elsevier)

It can be seen from the figure that the potential energy diagram of hydrogen in octahedral site is broad and flat compared to the potential well of hydrogen in tetrahedral site. This is in accordance with the space of octahedral and tetrahedral interstitial sites [92]. Hence, the zero point energy of the hydrogen atom in the tetrahedral hole is much higher than that in the octahedral hole. The relative stability of metal-hydrides/deuterides depends on the occupancy of hydrogen in octahedral or tetrahedral voids. When octahedral site is occupied, the difference between the zero-point energies in the gaseous and solid phases for protium is lower than that for deuterium. Whereas the difference between the zero-point energies in the gaseous and solid phases for protium is higher than the deuterium if tetrahedral sites are occupied. Hence, the heavier isotope gets stabilized in the tetrahedral hole compared to the octahedral hole. This implies the heavy isotopes have a relatively high solubility in tetrahedral holes and lighter isotope has higher stability in octahedral hole. In case of Pd/Pd-alloys having f.c.c crystal structure the hydrogen isotopes preferentially occupies octahedral site [67]. Therefore, in these systems, solubility of hydrogen decreases with increase in isotopic mass.

Isotopic effect is also observed in the diffusion of hydrogen is the metals. Hydrogen diffuses through the metal lattice by a quantum mechanical hooping mechanism from one interstitial site to the other. A schematic diagram of comparison between ground state and transition state potential profiles of octahedral-octahedral jump and tetrahedral-tetrahedral jump is shown in Figure 1.10. From the figure, it can be seen that in octahedral-octahedral jumping the difference between the energy levels of ground state and activated state decreases with increase in isotopic mass. However, it increases with increase in isotopic mass in case of tetrahedral–tetrahedral jump. This illustrates that the diffusion of hydrogen isotopes increases with increase in isotopic mass in octahedral-octahedral jump and decreases in tetrahedral-tetrahedral jump. Hence, in case of palladium based metallic membranes it is expected that the diffusion of hydrogen isotopes increases with increase in isotopic mass.

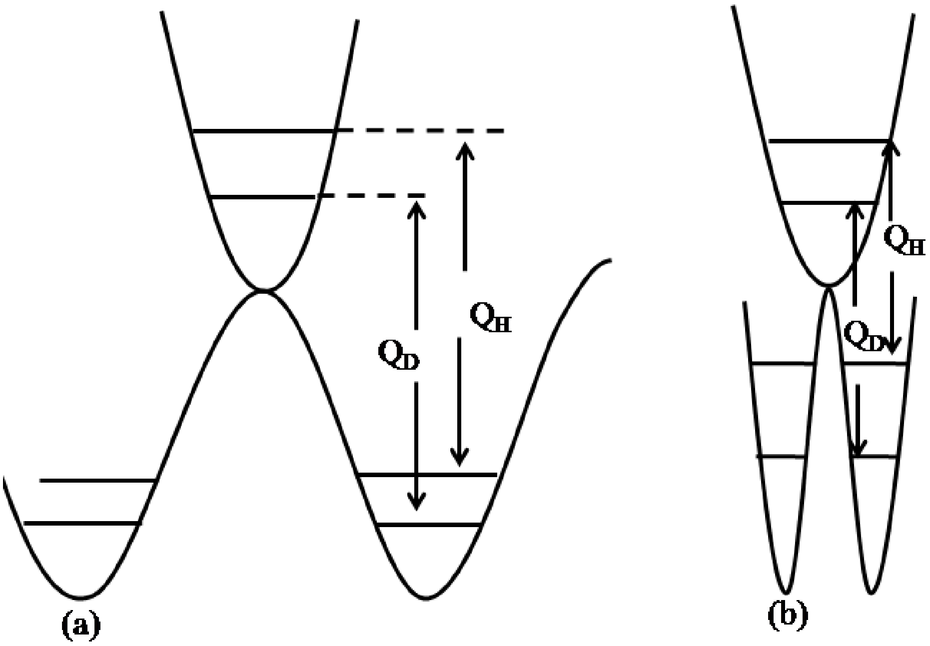

Figure 1.10. Schematic diagram of the potential profile for (a) octahedral-octahedral jumps and (b) tetrahedral-tetrahedral jumps. (Reprinted from [92], Copyright (1984), with permission from Elsevier)

1.5. Dense metallic membrane fabrication methods

A variety of methods have been employed in the preparation of dense metallic membranes. The most common methods are: metallurgical route of synthesis, chemical vapor deposition (CVD), physical vapour deposition (PVD), electro deposition (ED) and electroless plating (ELP) [93-98]. Metallurgical route is the conventional method of preparation of Pd-based dense metallic membranes. These membranes give excellent hydrogen flux and infinite hydrogen selectivity. Fabrication of ultra-thin membrane is always desirable to reduce the noble metal cost and enhance the hydrogen flux for their industrial applications [99]. However, ultra-thin membranes are difficult to prepare by the metallurgical route. Hence, several Pd based supported composite membranes have been prepared using different deposition techniques. The support materials are porous substrates made up of stainless steel, alumina or vychor glass, which gives a mechanical support to the membrane [98, 100].

1.5.1. Metallurgical route

This is the most classical and conventional way of membrane synthesis. In this method, the metal/alloy is prepared by melting the individual components. The cast metal/alloy is annealed and cold rolled in subsequent steps to prepare thin membrane sheets. Alloy tubes can also be prepared directly from the cast alloy or diffusion bonding of the thin foils [93, 96]. Annealing in between the metal processing (cold rolling or metal blasting) steps is necessary because of hardening of the materials during metal processing. The number of cold rolling steps varies depending upon the thickness of the foil to be prepared and hardness of the material.

Several Pd and Pd-alloy membranes of different thickness and geometry have been prepared by this method by Tosti et al. [93]. The membrane produced by this method often shows very high hydrogen selectivity. However, very thin membranes < 25µm thickness is difficult to prepare by this method.

1.5.2. Chemical vapour deposition (CVD)

Chemical vapour deposition (CVD) is a method for depositing thin films on a substrate by the thermal decomposition of one or several volatile precursors. This method is attractive technique for obtaining thin layer of palladium on substrate surface [94]. Highly volatile organometallic Pd-precursors such as $Pd(C_3H_5)_2$, $Pd(C_3H_5)(C_5H_5)$ and $Pd(C_5H_5)_2$ are available for the fabrication of Pd films by MOCVD (metallo organic CVD). CVD technique often results in better film quality. However, the disadvantages of CVD include contamination of the film with carbon from the organometallic complex and use of costly high vacuum components. Another problem associated with CVD is that the organometallic precursors are costly and difficult to synthesize [94].

1.5.3. Physical vapour deposition (PVD)

Physical vapour deposition (PVD) is evaporation of the precursor with a high energy beam of electrons or ions in a vacuum and condensation at the target metal surface. The process is similar to CVD; however no chemical decomposition reactions are involved in this process. This is because the precursors are usually pure metals in the elemental state, whereas in CVD, the precursors are chemical compounds in a vaporized state [94]. A representative technique in PVD is the magnetron sputtering method. The target is atomized by collisions of Ar ions excited by plasma and gets deposited on the substrate surface. In comparison to electroless plating, the sputtering technique allows better control of the film composition, phase and thickness. However, the equipments used in this process are costly due to use of high vacuum chambers, clean conditions, high current density to evaporate the target and expensive metal alloy targets. Another drawback is that substrates in any geometry cannot be coated; for instance the inside of a tube cannot easily be coated [96].

1.5.4. Electroplating

Electroplating is an electrochemical method in which metal ions are transported by the action of an electric potential and deposited on a substrate material in the other electrode. The substrate is a cathode and the positive metallic ions in the solution are reduced to metal and deposited on the substrate. The advantages of this technique are that it can be carried out with simple equipment and films of desired thickness can be deposited by controlling time or current density [97]. However, this method is limited to use of conducting support materials non conducting supports cannot be deposited in this method.

1.5.5. Electroless plating (ELP)

Electroless plating (ELP) is a method for deposition of metallic membranes by the reduction of meta-stable metal complex using a reducing agent. No external electric field is applied in this method. The advantages of ELP over other preparation methods include ease of coating on materials having any shape, independent on nature of material (metallic or non-metallic), low cost, and use of very simple equipment [98]. Conventional electroless plating is a two-step process and involves seeding a surface with Pd precursor particles and plating of the metal layer on top of the activated surface [101]. The activation is a preliminary step before all plating experiments. In this process, small grains of palladium nuclei are deposited on the substrate surface which catalyzes the further deposition of metal and also increases the adherence of plating [102]. The surface activation process is governed by a redox reaction. In this process, Sn(II) ions are oxidized to Sn(IV) and generated electrons reduces Pd(II) to palladium metal according to the following reactions.

Anodic reaction: $Sn^{2+} \rightarrow Sn^{4+} + 2e^-$ (1-31)

Cathodic reaction: $Pd^{2+} + 2e^- \rightarrow Pd$ (1-32)

Over all reaction: $Sn^{2+} + Pd^{2+} \rightarrow Sn^{4+} + Pd$ (1-33)

The Sn^{2+} is adsorbed on the surface in a hydrolytic form after the rinsing step and is replaced by Pd via redox process.

The electroless deposition of metals is best explained using the mixed potential theory. According to this theory the overall metal deposition is a combination of two different partial reactions: oxidation of the reducing agent and reduction of the metal ion. A schematic representation of metal deposition based on mixed potential theory is given in Figure 1.11. The figure shows the generalized polarization characteristics of the redox reactions associated with electroless plating. Curve 1 and curve 2 represent the polarization characteristics of the metal ions and the reducing agent respectively. I_M and I_{RA} are the currents associated with curve 1 and curve 2 respectively. For the metal deposition, the equilibrium electrode potential of the metal ions must be higher than that of the reducing agent. According to the mixed potential theory the electroless plating occurs at the electrode potential where I_M is equal to I_{RA} (because the net external current for the electroless plating is zero).

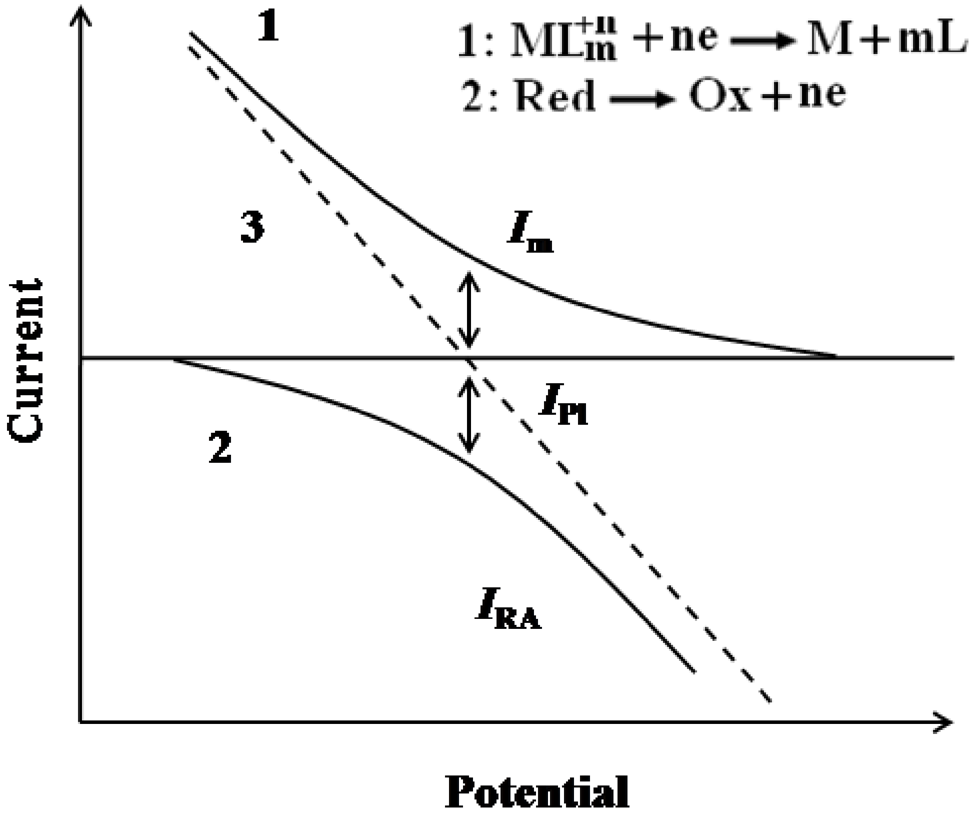

Figure 1.11. Schematic representations of polarization characteristics of metal deposition according to the mixed potential theory

Most of the membranes fabricated by this method for purification hydrogen isotopes are based on palladium and its alloys with silver and copper. This technique was first applied by Kikuchi et al. and Uemiya et al. [103,104] for deposition of Pd or Pd alloy composite membranes. The chemistry of these metal depositions using different plating baths is described below. In case of palladium and silver deposition using hydrazine based plating baths, Pd (II) and Ag(I) forms complex with EDTA and hydrazine reduces Pd(II) to Pd(0) and Ag(I) to Ag (0) in a basic medium. Nitrogen gas is evolved from the reaction which is an indication of reaction progress.

Anodic reaction: $N_2H_4 + 4OH^- \rightarrow N_2 + 4H_2O + 4e^-$ (1-34)

Cathodic reaction for Pd: $2[Pd(NH_3)_4]^{2+} + 4e^- \rightarrow 2Pd + 2NH_3$ (1-35)

Cathodic reaction for Ag: $4Ag(NH_3)_2^{2+} + 4e^- \rightarrow 4Ag + 8NH_3$ (1-36)

Overall reaction of Pd deposition:

$2[Pd(NH_3)_4]^{2+} + N_2H_4 + 4OH^- \rightarrow 2Pd + 8NH_3 + 4H_2O + N_2$ (1-37)

Overall reaction of Ag deposition:

$4Ag(NH_3)_2^{2+} + N_2H_4 + 4OH^- \rightarrow 4Ag + 8NH_3 + N_2 + 4H_2O$ (1-38)

The chemistry of copper deposition is similar to that of Pd and Ag. However HCHO is used as a reducing agent instead of N_2H_4. The deposition takes place according to the reaction given below.

$2HCHO + 4OH^- \rightarrow 2HCOO^- + 2H_2O + H_2 + 2e^-$ (1-39)

$Cu^{2+} + 2e^- \rightarrow Cu$ (1-40)

$Cu^{2+} + 2HCHO + 4OH^- \rightarrow Cu + 2HCOO^- + 2H_2O + H_2$ (1-41)

Though electroless plating is an easy and cost effective method for production of thin supported membranes but high time-consumption and difficulty in composition control in alloy plating are the major drawbacks of this method.

1.6. Historical background and current status of using Palladium based membrane in hydrogen purification

Classically, palladium membrane is used for purification of hydrogen isotopes due to high hydrogen permeability, good thermal and mechanical stability. However, pure palladium membrane suffers hydrogen embrittlement due to α-β phase transition below a critical temperature of 298°C and pressure of 20 atm [58]. The hydride β phase has an expanded lattice (4.02 Å) compared to α phase (3.89 Å) [105]. Thus, the phase transition is accompanied by the volume expansion (~10%) in the host lattice while retaining the f.c.c structure. Therefore, if a pure Pd membrane is exposed to hydrogen below the critical temperature (i.e. 298° C), the transition between α and β phase could cause cracking of the membrane [106]. This results in the loss of the hydrogen selectivity and membrane integrity. The high critical temperature for the phase transition in the Pd-H system is a drawback of the Pd membranes from the industrial application point of view. The hydrogen embrittlement can be suppressed by alloying Pd with other metals. Alloying metals with appropriate composition suppresses critical temperature, enhances the hydrogen permeability and the mechanical properties [106].

Alloying Pd with another metal changes the lattice sizes and the number of vacant d-band holes in Pd [107]. As a result, the hydrogen solubility in different phases (α and β) and the extent of α-β phase transition changes. Literature reported data suggests that the addition of metal such as Ag, Cu, Pt, Ni, Rh, Au lowers the critical temperature [105-107]. Among the alloying elements, Ag has drawn considerable early interest because it is the nearest neighbour of Pd in the periodic table and it forms a complete range of solid solution with Pd [108]. It is reported that addition of Ag to Pd results in lattice expansion and the alloy has lower 4*d* orbital density compared to that of Pd [106]. Brodowsky and Poeschel [109] studied the α-β phase transition in Pd-Ag-H systems. Their findings show that the addition of Ag into Pd increases the resistance to hydrogen embrittlement and for Ag concentration more than 25 at% in Pd results in the disappearance of α to β phase transition at 50^oC. The study by Knapton [49] for the binary alloys of metals, such as Ag (23 wt%), Cu (40 wt%), Ce (8 wt%) and Y (12 wt%) with Pd shows positive effect on the H_2 permeability. According to Knapton [49] and Kikuchi et.al [110], the permeability of H_2 increases with the addition of Ag into Pd up to 23 wt% Ag and then decreases on further addition. Another factor which affects the H_2 permeability in Pd membranes is the surface poisoning in presence of contaminating species like CO, CO_2, H_2S etc. These contaminants decrease the catalytic dissolution of hydrogen in the matrix also increases the activation energy of hydrogen adsorption ion metal surface. Several alloys of Pd-Cu, Pd-Pt and Pd-Au shows increased resistance to poisoning species [111-113].

Pd-based dense metallic membranes find application for both purification of industrially produced hydrogen and processing of fusion fuel gas. The same membrane material can be used for both the applications; however, the process requirements are different. For industrial applications the membrane should be operated at a trans-membrane pressure of ≥ 3 bar at moderate temperature (500-800K). Hence cost effective membranes having lower noble metal inventory with high hydrogen flux and moderate hydrogen perm-selectivity (500 to 1000) are being extensively explored for this application. In the processing of the fusion fuel gases the transmembrane pressure is kept low (approximately 100 kPa) and the Q_2 partial pressure in the feed gas varies from 1 Pa to 100 kPa. The temperature is also preferred to be within 500-700 K to minimize tritium losses due to permeation through reactor walls. Therefore for this application radiation resistant membranes with infinite hydrogen perm-selectivity are the prime requirement. Pd-based membrane reactor coupled to a Pd-based membrane diffuser, where low concentration of Q_2 needs to be recovered, is proposed for this application. Both purification of industrially produced hydrogen and processing of hydrogen isotopes for fusion fuel applications plays vital role in the future energy scheme. There are many literatures available for Pd-based metallic membranes for hydrogen purification applications [107-113]. However, a very limited work has been done on application of palladium based membranes for purification of hydrogen isotopes for fusion reactor application. Most of the available literature information relates to purification studies based on Pd and binary Pd-alloys. Therefore, it is imperative to explore other palladium based alloys with higher permeability for these applications.

1.7. Objective of the present investigation

The present thesis deals with development of palladium based metallic membranes for purification of hydrogen isotopes. Pd-Ag and Pd-Ag-Cu alloy membranes were prepared by conventional metallurgical route as well as by electroless plating method. In the metallurgical route, membranes were prepared by arc melting followed by cold rolling and annealing. In this method, membranes of 100 µm thickness were prepared. In the electroless plating method, Pd-Ag and Pd-Ag-Cu alloy membranes were prepared by electroless deposition of constituent elements on porous stainless steel support. In this method, membranes of approximately 30 µm thickness were prepared. The alloy membranes prepared by both the methods were characterized for composition by TXRF and EDS, phase by XRD, morphology by SEM. Hydrogen and deuterium permeation experiments on membranes prepared by metallurgical route were carried out at different temperatures. Thermodynamics and kinetics of hydrogen and deuterium sorption on Pd-Ag, Pd-Ag-Cu alloys were carried out by employing Sieverts' type volumetric apparatus.

In addition to the above objectives, the membrane was investigated for separation of helium from tritium. In a tritium storage bed ^{3}He is formed due to radioactive decay of tritium. Being an inert gas, ^{3}He gets released from the entrapped tritium bed and develops pressure in the storage vessel. This ^{3}He can be removed and used for neutron detectors. However, the ^{3}He recovered in this manner contains tritium at low concentration which should be purified for its use in neutron detectors. Hence, in the present investigation, the applicability of this membrane configuration was explored for purification of ^{3}He from traces of tritium.

CHAPTER 2

EXPERIMENTAL

Chapter 2. Experimental

2.1. Synthesis of membrane by metallurgical route

2.1.1. Preparation of alloys by arc melting method

Pd-alloys were prepared by arc melting method using high pure components. The arc furnace used in this study consists of a non-consumable tungsten electrode as cathode and a water cooled copper hearth as a part of the anode (*Edmund Bühler Gmbh*, Model-MAM-1). Electric arc is generated between the tungsten electrode and the copper hearth by applying low voltage and high ampere current. The copper hearth is designed to hold the raw material. The arc melting furnace is coupled with a chiller unit which cools the copper hearth and the tungsten electrode to protect them from overheating/melting. A rotary pump is connected to the furnace to attain a vacuum of 10^{-3} mbar. The furnace is flushed with high pure helium gas several times to ensure oxygen and moisture free environment. Evacuation and flushing with inert gas avoids oxidation of molten metal/ alloys. The temperature of melt and evaporation loses of the low melting metal was controlled by optimizing the current supply. Stoichiometric amounts of high pure palladium, silver and copper (Sigma Aldrich, 99.99% trace metals basis) were melted under high pure helium atmosphere. The ingots were repeatedly melted for six times by turning over inside the furnace to ensure homogeneity of the relative concentration of atoms. When the arc is broken, the bottom of the sample gets cooled faster than the top due to direct contact with the cooled copper hearth. This irregular cooling of the ingot in the arc furnace results in poor crystalinity and generates strain in the system. Hence, annealing of the samples is required to improve the homogeneity, crystalinity and remove the strain that appear during solidification due to segregation. In order to attain an equilibrium phase, the cast alloy ingots were wrapped in tantalum foil and annealed in sealed and evacuated quartz ampoule at 1073 K for about 150 hours. Then the annealed alloys were cooled slowly to room temperature inside the furnace. Negligible weight loss was observed after melting and annealing, which ensures the composition to be similar as taken on the starting.

2.1.2. Membrane synthesis by cold rolling technique

Cold rolling method was used for preparation of alloy foils of 100 μm thickness. Cold rolling is a practical metal working process to prepare thin metal sheets. Several kinds of rolling mills are used according to the hardness of the material, rolling speed, minimum thickness, etc. The minimum thickness which can be obtained for a given material depends on the diameter of the milling rolls. Smaller the diameter of the milling rolls, thinner the worked metal sheet. However, the use of small diameter rolls involves their bending under operation and produces curved foils [114, 115]. A four-high rolling mill (shown in Figure 2.1) has been used to produce very thin and straight foils. In such a device two larger support rolls constrains the working rolls of small diameter by avoiding their bending. The hardness of the material changes upon rolling hence, during the cold rolling intermediate thermal treatment is necessary [116]. These thermal treatments are carried out under reducing atmosphere of hydrogen and helium mixture at a temperature of 823 K to remove strain and avoid the oxidation at high temperatures. Each time before annealing, the foil was cleaned by alkali and acetone in ultrasonic bath. Finally the prepared foil was surface polished using sand paper of 1200 grit size followed by acetone cleaning in ultrasonic bath. The cleaning process was done to remove any oil and organic impurities during cold rolling.

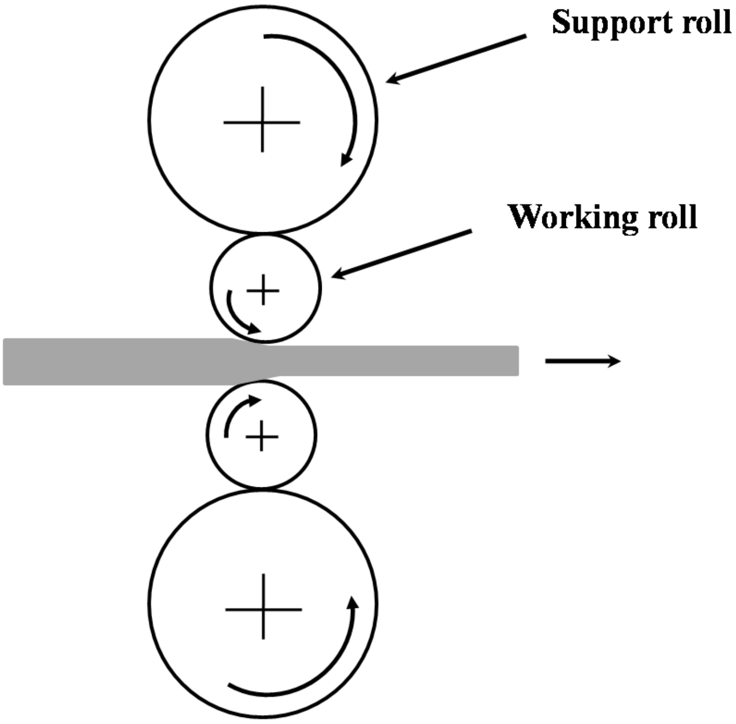

Figure 2.1. Schematics of a rolling meal

Powder of the ternary Pd-Ag-Cu alloy ingot was made by using a diamond file. The alloy powder was annealed under hydrogen and helium atmosphere to remove strain.

2.1.3. Characterization of membranes prepared by metallurgical route

2.1.3.1. Compositional analyses of the alloys by Total Reflection X-ray Fluorescence (TXRF)

Compositional analyses of the alloys were carried out using Total Reflection X-ray Fluorescence (TXRF) spectrometry. TXRF is an advanced variant of Energy Dispersive X-ray Fluorescence (EDXRF) for micro and trace elemental analysis. It is based on the principle of total reflection of X-rays from a flat smooth surface at a grazing angle less than the critical angle of the sample support [117]. It differs from the classical X-ray fluorescence in the way of incidence angle of X-rays. In XRF, the angle of incidence is ~ 45° whereas in case of TXRF the grazing incidence angle is in the range of 0.1–1^{o} [118]. For TXRF analysis, a small amount of sample in the form of a thin film is irradiated with X-rays in total reflection condition. Total reflection occurs if X-rays strike a medium with grazing incidence. The glancing angle must be smaller than a critical value 'Θ_c', which can be calculated according to Snell's law:

$$\Theta_c = \sqrt{(2\delta)} \tag{2.1}$$

where, δ represents the dispersion of the medium and is dependent on the density of the medium. The reflectivity and penetration depth are dependent on the angle of incidence. With increase in incident angle, the reflectivity decreases and the penetration depth increases. At the critical angle, the X-rays are totally reflected from a plane surface and a very little penetration into the medium takes place. As the X-rays do not penetrate inside the sample support, there is very little scattering of the X-rays from the sample support. Therefore, the background is considerably reduced. In addition, the specimen is excited by incoming as well as the totally reflected beam. This condition makes the excitation efficiency of the elements almost double compared to the conventional X-Ray Fluorescence (XRF). The detector can be placed very near to the sample at an angle of 90^{o} to the surface, which increases the detection efficiency. All these factors contribute towards a better detection limit. Due to the better detection limit, low matrix effect, minimum sample size, TXRF technique finds application in several fields for micro and trace elemental analysis and surface characteristics [117].

In this study, the alloy samples were dissolved in nitric acid and sonicated for an hour to prepare 10 µg/ L sample solution. The sample solution was deposited on a polished quartz support, dried and TXRF spectrum was recorded using an ITAL STRUCTURES TXRF spectrometer: TX-2000. The spectrometer is equipped with a Mo-W dual target tube and operates at voltage and current of 40 kV and 30 mA, respectively. Monochromatic Mo Kα radiation (17.443 keV), obtained from the W-Mo dual target X-ray tube and a W/C multilayer monochromator, was used for sample excitation. The characteristic X-rays emitted from the sample were detected with a Si (Li) detector having a resolution of 139 eV (FWHM) at 5.9 keV (Mn Kα). The elemental concentrations are determined by comparison of the normalized intensities of each element after consideration of its characteristic X-ray line sensitivity with that of a standard.

2.1.3.2. Phase analysis using X-ray diffraction method

The phase analysis of the alloys were carried out by X-ray diffraction (XRD) method. X-ray diffraction is a non-destructive characterization technique for identification of the crystallographic phases present in the sample. In X-ray diffraction, monochromatic X-rays beams are used to interact with the crystal and the scattered beams are detected with a detector. The most common source of X-rays used in the instruments is an X-ray tube, in which high energy electrons are bombarded with the anode to generate X-rays. The X-ray beams interact with the electronic cloud of the atoms present in the material and get scattered. Constructive and destructive interference takes place between the scattered X-rays. This happens because, the difference between the scattering centers (inter atomic spacing) are in the order of wavelength of X-rays. The constructive and destructive interferences cause increase and decrease in intensities of in the scattered X-rays. The condition for constructive interference of the X-ray beam at an angle θ is given by Bragg equation [119].

$$n\lambda = 2d\ \mathrm{Sin}\theta \qquad (2.2)$$

where, n is the integer, λ is the wavelength of X-ray, and d is the inter-planner spacing for a particular set of plane with Miller indices ($h\ k\ l$). The diffracted beams are detected using a detector, counted and processed to form a diffraction pattern, which gives information about the crystalline phase of the material. Each crystal has a unique diffraction pattern because of the difference in the arrangement of the atoms in the material.

In this study, the room temperature as well as the high temperature X-ray diffraction measurements were carried out using a diffractometer (theta–theta geometry) supplied by GNR Analytical Instruments Group, Italy (Model: EXPLORER). The source of X-rays in the instrument is a copper tube producing X-ray beams of Cu Kα with 1.5406 Å wavelength. The diffractometer operated at the power level of 1.6 kW (40 kV and 40 mA) and was equipped with the secondary graphite monochromator in the diffracted beam. The detector is a NaI scintillation counter. The room temperature XRD patterns were recorded in the 2θ range of 30-90° with a step of 0.02° and 3 seconds counting time. The high temperature XRD measurements were carried out using Anton Paar HTK16N high temperature chamber. Pd, Pd-Ag and Pd-Ag-Cu foils of 100 µm thickness were used for this study. The chamber is connected with a turbo molecular pump to reach and maintain a high vacuum condition during high temperature experiments. This is done to protect oxidation of the sample. Vacuum of approximately $3\text{x}10^{-7}$ bar was maintained in the chamber throughout the experiments. The sample was heated using a heating unit consisted of a platinum strip with a spot welded thermocouple which is controlled by a controller with an accuracy of ±1 K. The heating strip is pre-stressed to compensate its thermal elongation upon heating, which ensures a very stable sample position over the complete temperature range. The experiment was carried out in the temperature range of 298 to 1023 K at a span of 50 K. At each isothermal temperature, the sample was kept for 30 minutes to attain thermal equilibrium before recording the diffraction pattern. Si (2 2 0) diffraction line was chosen as a reference line for the calibration of the diffraction position. The difference in the arrangements of atoms in the crystal lattice gives rise to a unique X-ray diffraction pattern. The recorded X-ray diffraction patterns are used for phase identification by comparing with the reported pattern in the International Centre for Diffraction Data base (ICDD) [120]. In this study, phase identification from the diffraction patterns were carried out using MATCH-2, CRYSTAL IMPACT software. The High temperature XRD patterns were used for determination of thermal expansion and Debye temperature of the alloys.

2.2. Preparation of membrane by electroless plating method

Pd and Pd-alloys were deposited on porous stainless steel (PSS) substrate by electroless plating method. The metal deposition was carried out using conventional two step process; (a) activation of the substrate surface and (b) metal/alloy deposition on the activated substrate. In the present investigation, porous stainless steel is chosen as the substrate material because of similar thermal conductivity of stainless steel with palladium [121]. Both tubular and planar disc shaped substrates (shown in Figure 2.2) of porosity of 30% and 0.2 µm media grade (supplied by Mott metallurgical corporation) were used for electroless plating.

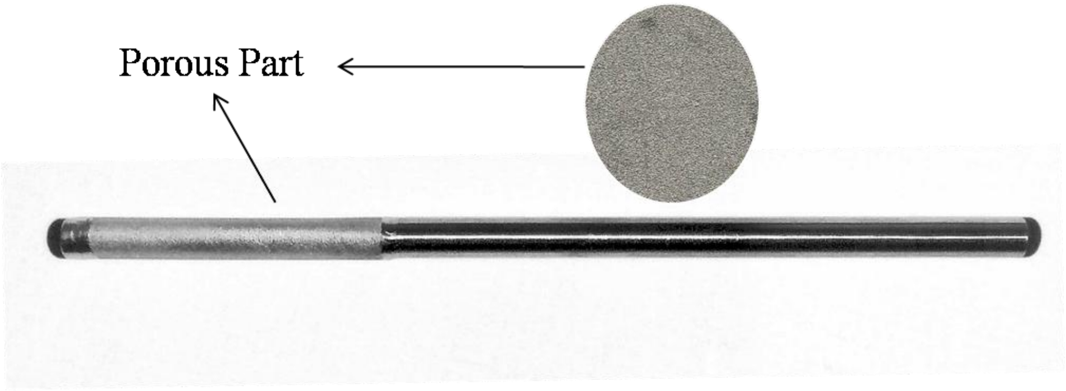

Figure 2.2. Different PSS substrates used for plating experiment

For effective utilization of the disc shaped membranes in hydrogen permeation experiments, the PSS discs were joined to non-porous SS pipe. The joining of porous to nonporous part is difficult, because of the cracks generated due to excess heating during conventional TIG welding process. To overcome this problem, other welding techniques such as low energy electron beam welding and pulsed laser welding were explored for this application. The assembly made after laser beam and electron beam welding are shown in Figure 2.3. The welding portions were scratched with sand paper before deposition to make a rough surface and to remove the oxides formed during welding because rough surfaces have good adhesion properties compared to the plain surface. The PSS substrate was then subjected to different surface cleaning and activation treatment before electroless plating experiment.

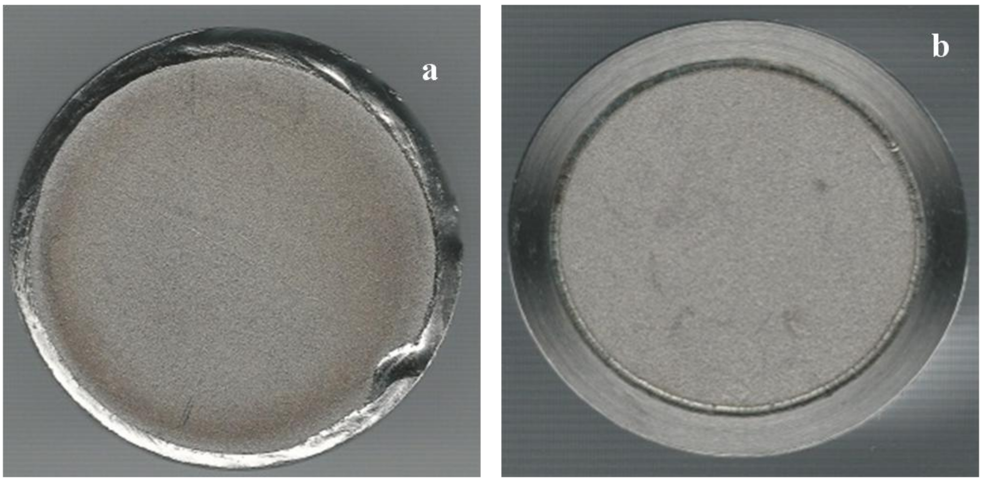

Figure 2.3. PSS-NPSS welded assembly for electroless plating, (a) EB welding, (b) Laser beam welding

2.2.1. Cleaning and activation of substrate surface

The presence of organic and non metallic impurities on the surface interfere in bonding and results in poor adhesion. Even these contaminants can prevent the deposition of metal on the surface. Hence, proper surface cleaning is a pre-requirement before metal deposition experiment [122]. Several surface cleaning processes are developed to remove the contaminants from the surface and increase the efficiency and durability of plating. In case of porous substrates, the residues penetrate the pores and interfere in plating. These residues in the pores decompose or vaporize during plating experiment and causes blistering effect. Therefore the contaminants are required to be removed from the pores for which, the cleaner must penetrate through the pores of the substrate. In this study, the substrate was thoroughly cleaned with an alkali solution in an ultrasonic bath. The composition of the solution is given in Table 2-1. For cleaning, the substrate was placed in a 250 ml alkali solution at 323 K in an ultrasonic bath for about 2 hours. After that, it was ultrasonicated several times with de-ionized water until the pH of the residue becomes neutral. Thereafter, the substrate was dried in an oven for about 6 hours.

Table 2-1. Alkali solution used for cleaning the surface

Chemicals	Concentration (M)
$Na_3PO_4 \cdot 12H_2O$	0.12
Na_2CO_3	0.6
NaOH	1.12
Detergent solution	5ml/L

To improve the homogeneity and adhesion of plating, the substrate was activated by seeding small grains of Pd nuclei on the surface. This was carried out by alternative immersion in the acidic solution of $PdCl_2$ and $SnCl_2$ with intermediate rinsing with de-ionized water. The concentration of activating solution is given in Table 2-2. The solutions were freshly prepared each time before activation. Total 100 ml of each $PdCl_2$ and $SnCl_2$ solutions were taken for this experiment. A teflon assembly was prepared for seeding and deposition of metals on the PSS disc. This was done in order to plate the PSS part only and to protect the rest of the tubular assembly. The PSS assembly was placed in such a manner that only the porous part was exposed to the seeding/plating solution. Schematic diagram of the teflon assembly used for seeding/plating of PSS substrate is shown in Figure 2.4.

The activation of the PSS was done by following steps.

a. The PSS substrate was dipped in stannous chloride solution (sensitizing solution) and kept for five minutes followed by rising with DI water.

b. After that the substrate was dipped in palladium chloride solution (activating solution) and kept for five minutes followed by rinsing with 0.01 N HCl and distilled water.

Table 2-2. Composition of seeding solution

Chemicals	Concentration
$SnCl_2.H_2O$	1 g/L
$PdCl_2$	0.1 g/L
HCl	0.01 N

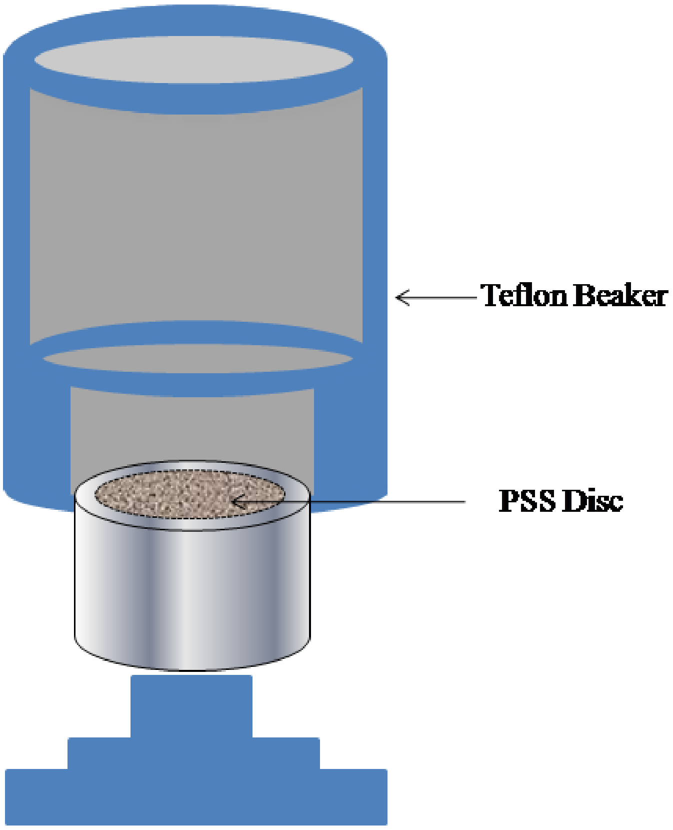

Figure 2.4. Schematics of Teflon assembly used for electroless plating

The purpose of immersing the supports in 0.01 M HCl after immersion in $PdCl_2$ solutions was to prevent the hydrolysis of the Pd^{2+} ion which would form hydroxyl-chlorides on the supports [102]. During rinsing with DI water after dipping in acidic $SnCl_2$ solution, hydrolysis of Sn^{+2} solution takes place to form a thin layer of tin hydroxy-chlorides on the surface. The thickness of the layer depends on the ratio of $HCl/SnCl_2$ solution, support surface roughness and the hydrodynamic regime of rinsing. An excess of the Sn^{+2} would cause an easy to peel layer, while deficiency of this causes a non-uniform Pd nuclei seeding [101]. Therefore the two step emersion process was repeated for ten times to get homogenous activation. The appearance of dark brown colour on the surface confirms homogenous seeding. The activation was done at room temperature. After proper activation, the disc was dried at 383 K for 8 hours and the weight gain was monitored.

2.2.2. Electroless plating of Pd and Pd-alloys on PSS substrate.

In this study, Pd, Pd-Ag, and Pd-Ag-Cu alloy membranes were prepared on PSS substrate by electroless plating method. Hydrazine based plating baths were used for the deposition of Pd and Ag whereas a formaldehyde based plating bath was used for the deposition of copper on the porous stainless steel substrate. The plating solutions were prepared in ultrasonic bath according to the composition given in Table-2.3. All the chemicals used were from Sigma Aldrich and had a chemical purity of more than 99.8%. A series of experiments were carried out to optimize the plating parameters for efficient and homogenous deposition. Copper deposition was always carried out after Pd and Ag deposition, because copper gets dissolved in NH_4^+ ion rich plating solution of Pd and Ag. Isothermal condition at 333 K and constant pH of 10 were maintained during the plating experiments of Pd and Ag. The solution was preheated to the experimental bath temperature for easy attainment of thermal equilibrium. The deposition of Cu was carried out at room temperature and at a constant pH of 11. During the deposition of Pd and Ag, the pH of the solution continuously decreases with the progress of reaction. Therefore, the pH was maintained constant by intermediate addition of NH_4OH. Each time, freshly prepared solution was used for deposition.

Table 2-3. Composition of different plating baths

Bath components	Pd bath	Ag bath	Cu bath
$PdCl_2$	1.6 g/L	-	-
$AgNO_3$	-	0.38g/L	-
$CuSO_4$	-	-	2g/L
Na_2EDTA	40 g/L	40 g/L	30g/l
EDA			100 ppm
NH_4OH	3M	3M	-
N_2H_4(1 M)	5.6ml	5.6ml	-
NaOH	-	-	20 gm/L
HCHO	-	-	15ml/L

The addition of reducing agents (N_2H_4 for Pd & Ag and HCHO for Cu) was carried out in a stepwise manner to avoid bulk precipitation. The complete procedure of electroless plating is shown in Figure 2.5. In addition to the above effects of bath components and operation conditions other parameters stirring also plays an important role in electroless plating of metals/alloys. Stirring of the solution often increases the rate of metal deposition by enhancing the mass transfer phenomena inside the bath. Metal deposition by electroless plating method is accompanied by release of different gas molecules. The accumulation of the gases on the surface causes blistering effect, thereby resulting in a poor film deposition. Mechanical stirring helps in release of the gas molecules from the surface of the substrate as soon as it is formed. It increases the homogeneity of metal deposition by restricting the localized buildup in ion concentration. Hence, in this study the solution was stirred continuously with the help of a mechanical stirrer. Higher stirring rate caused turbulence in the solution and very slow stirring rate was found to have minimum effect. Therefore, the speed of stirring was optimized according to the amount and shape of sample used.

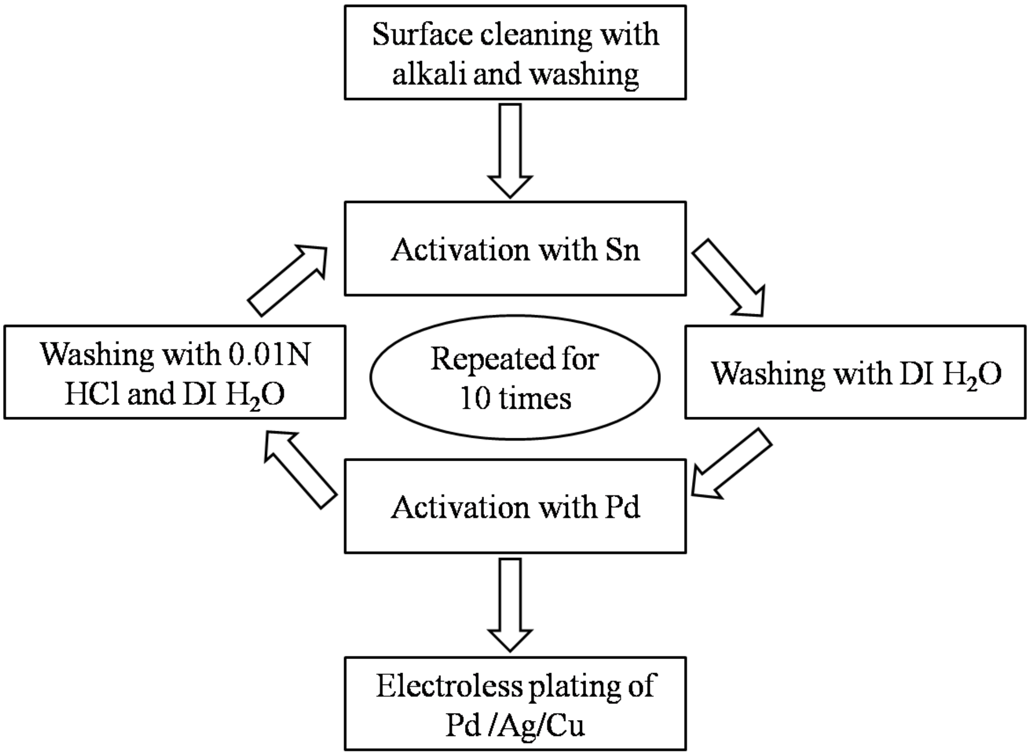

Figure 2.5. Process of metal deposition on PSS substrate by electroless plating technique

The deposition of metals was carried out for 4-6 hours depending upon the rate of deposition. For getting a dense metallic membrane, the plating experiments were repeated. The plated substrates were dried at 393 K for 8 hours and the weight gain was recorded after each plating experiment. The thickness of the metal deposited was calculated from the weight gain. For alloy formation, different metals were deposited over PSS substrate and annealed under helium and hydrogen atmosphere at 823 K for 20 hours each.

2.2.3. Characterization of membrane prepared by electroless plating method

The membranes were characterized by XRD, scanning electron microscope (SEM) and Energy-dispersive X-ray spectroscopy (EDS) for phase, morphology and composition analysis, respectively. In order to study the alloy formation, the membrane was characterized by XRD before and after annealing. The XRD patterns were recorded using the same instrument discussed previously (section-2.1.3.2). The patterns were taken in the range of 30-90 degree at a step of 0.03 degree per 2 second.

Scanning electron microscope (SEM) is a type of electron microscope that produces images of a sample by scanning it with a focused beam of electrons. In this technique, high energy electrons are generally scanned across the sample in a raster scan by the scan coil [123]. The electrons interact with atoms in the sample and produce a number of signals. These signals are detected and images are formed. The image contains information about the sample's surface topography and composition. When a high-energy primary electron beam is impinged on an atom of specimen, it undergoes different types of interactions. The interaction of electron beam with the atomic nucleus can be divided in to two categories: elastic scattering that affects the trajectories of the electrons without altering its energy and inelastic scattering that results in transfer of a part or full energy of the electron beam. Thus, the electron-matter interactions produces back scattered electrons, secondary electrons, X-ray fluorescence photons, augur electrons, and various other photons [123]. The elastic scattering of the impinged electrons by atomic nuclei of the sample generates back-scattered electrons (BSE). Inelastic scattering of electrons by sample atoms results in loss of energy of the electrons and low energy secondary electrons (SE) are produced. The back scattered electrons and the secondary electrons are used for the study of morphology of the surface. The probability for elastic scattering increases with Z^2 and hence BSEs are useful for generating images of sample containing multiple atoms based on Z-contrast [124]. The characteristic X-rays (characteristic and Bremsstrahlung background X-rays) generated as a result of inelastic scattering are useful for chemical analysis of the sample. Ultra-high vacuum (10^{-6} torr) is maintained in the instrument. The sample used must be dry and electrically conductive. The volatile components present in the sample are pretreated before analysis.

In the present study, the surface morphology of the deposited membranes was analyzed by Scanning Electron Microscope (SEM, SERON INC South Korea, Model ATS 2100). The deposited membranes were perfectly dried to remove the moisture and volatile components of the sample. The compositional analysis was carried out by energy-dispersive X-ray spectroscopy (EDS) using oxford Instruments UK, model number INCAE 350. This is an analytical technique used for the quantitative elemental analysis. As discussed above, the characteristic X-rays generated by the electron-matter interaction are measured by an energy-dispersive spectrometer. Chemical composition of the sample is determined by comparing the intensities of characteristic X-rays from the sample material with intensities from a standard sample of sample elements with known composition. The composition of the deposited alloys was measured by taking average of the compositions at different morphological positions.

2.3. Hydrogen and deuterium permeation experiments of alloys prepared by metallurgical route:

2.3.1. Fabrication and testing of membrane module

100 µm thick alloy foils, prepared by cold rolling method were used for hydrogen and deuterium permeation studies. The foils were cleaned with alkali solution (Table 2-1) followed by ultrasonication in acetone and de-ionized water to remove the oil and grease residues from the surface. The annealed and surface cleaned foils in the form of circular disc of 35 mm diameter were vacuum brazed with a solid stainless steel (316 L) tube of 5 mm thickness to prepare the permeator tube. The schematics diagram of vacuum brazing the membrane with the SS tube is shown in Figure 2.6.

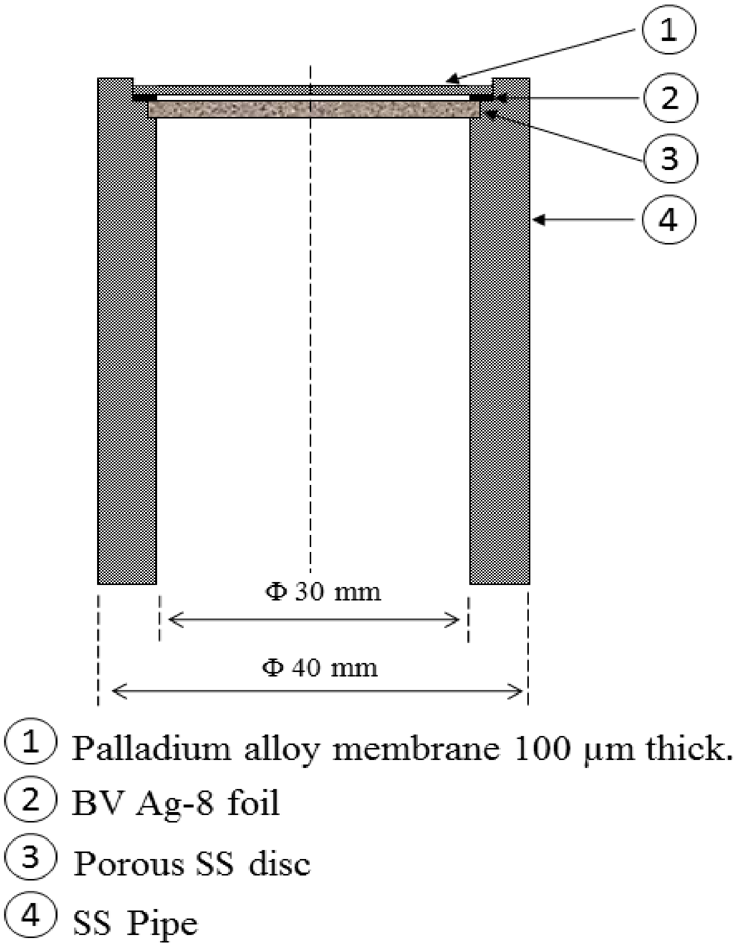

Figure 2.6. Schematic diagram of vacuum brazing of membrane with SS tube

A porous stainless steel (PSS) disc of 0.2 µm grade was used as a mechanical support to the membrane in the inner side of the tube. The faying surface cannot be wetted by brazing filler material due to chemically stable chromium oxide (Cr_2O_3) layer. Hence, prior to brazing, the stainless steel faying surface was electroplated with nickel strike of ~ 6 µm followed by copper plating of ~ 5 µm thickness. A silver-copper eutectic ($Ag_{0.72}Cu_{0.28}$, commercially known as BVAg-8) foil of 0.1mm thickness was used as brazing filler material. Brazing time and temperature were optimized to get leak tight and strong joint. Maximum care was taken to minimize the flow of brazing material by using very small filler material and minimum brazing time while ensuring a solid and homogenous joint. The liquidus temperature of the eutectic is 1053 K but brazing temperature was selected to be 1073 K for better fluidity and wetting action. The fabricated permeator tube is shown in Figure 2.7. The tube was leak tested using a helium leak detector (model-Agilent 959 Macro Torr) with a detection limit of 10^{-9} cc/sec helium leak rate.

Figure 2.7. Vacuum brazed tube

The prepared tube was joined with a CF flange to prepare a membrane module, shown in Figure 2.8. The performance of the permeator tube was tested using a re-circulatory and continuous closed loop permeation setup shown in Figure 2.9. The permeation setup was indigenously designed and fabricated using standard stainless steel (SS 316 L) ultra-high vacuum components.

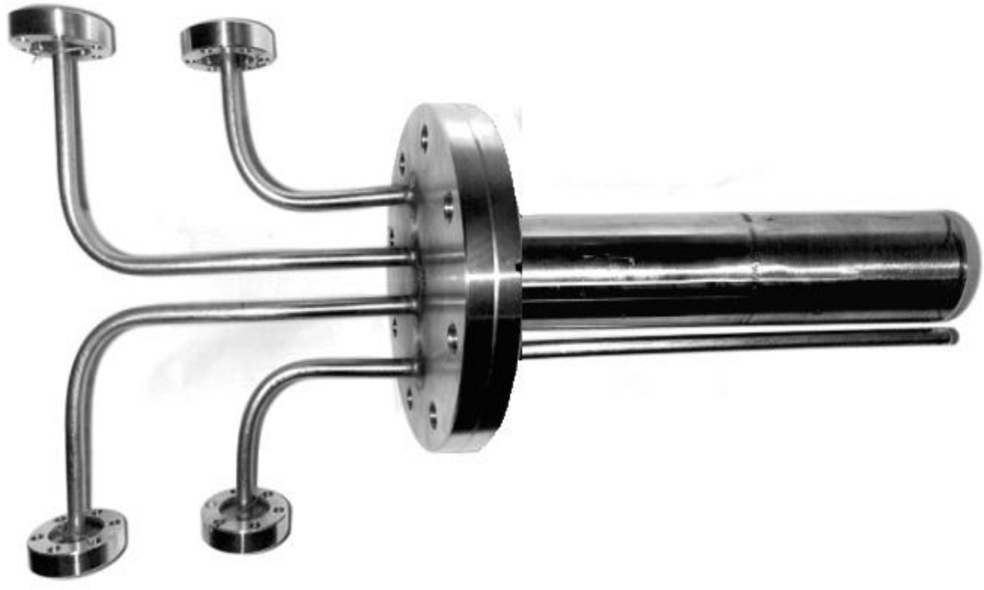

Figure 2.8. Fabricated membrane module

The gas permeation setup consists of a permeation cell, pressure and vacuum gauges, recirculation pump, mass flow controllers, pressure regulating valves and uranium getter bed. The permeation set-up is shown in Figure 2.10.The permeation setup was leak tested using the same helium leak detector and found to hold 10^{-6} torr vacuum. The membrane was heated with a resistance furnace with PID controller and the membrane temperature was measured by a K-type thermocouple with an accuracy of ± 1 K. The outer jacket of permeation cell is made up of 5 mm thick SS-316L to avoid hydrogen diffusion through the walls. Analysis of feed and permeate gases was carried out using a residual gas analyzer (Model SRS RGA 200). The membrane module was leak tested at different trans-membrane pressures (up to 400 kPa) and temperatures (up to 773 K) by filling helium in the feed side and analyzing the permeate side using the RGA.

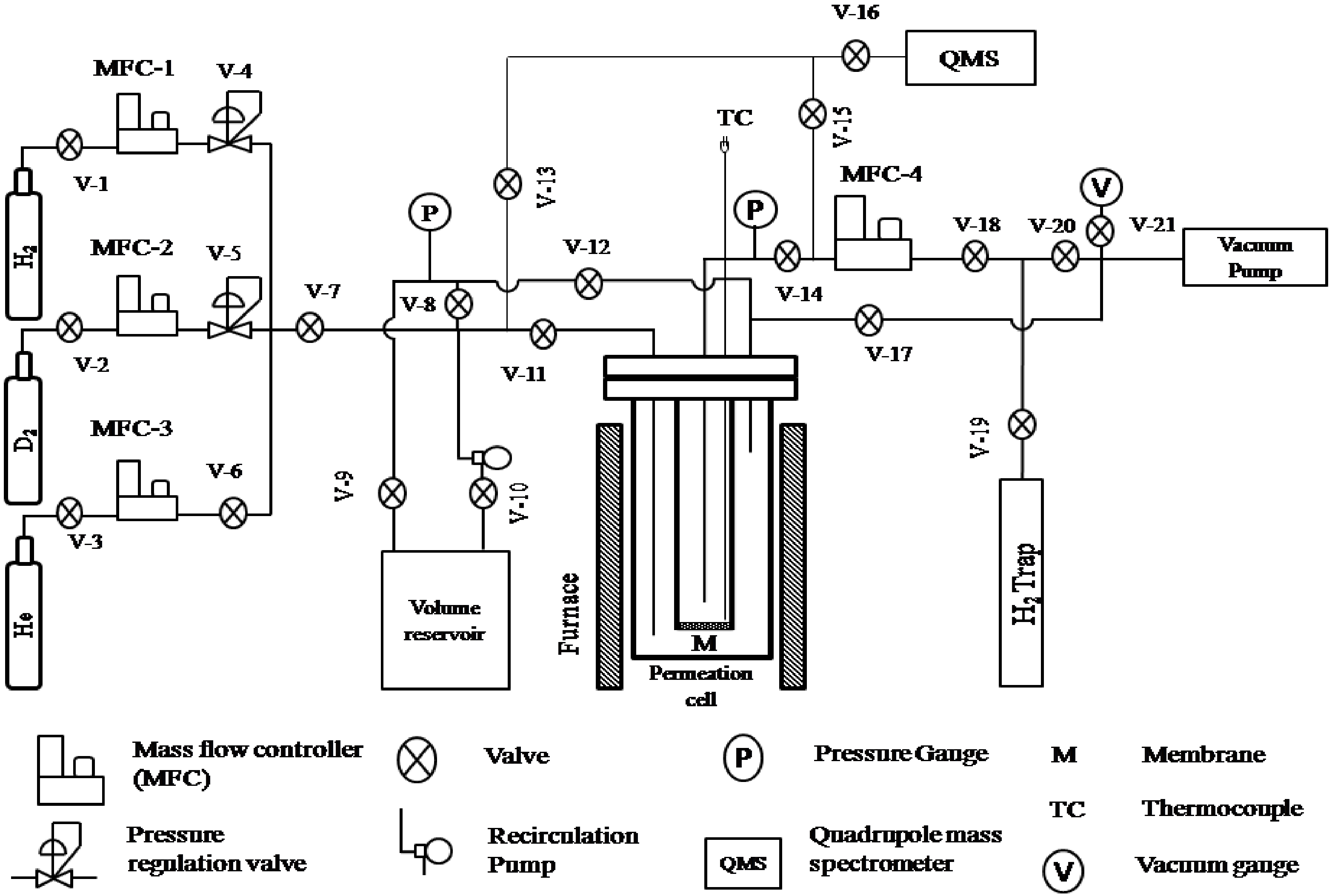

Figure 2.9. Schematic diagram of permeation setup

Figure 2.10. Hydrogen permeation setup

2.3.2. Hydrogen/deuterium permeation experiments

Activation of the surface is an important step during the permeation experiment. The presence of adsorbed gas molecules (other than hydrogen) on the surface of the membrane decreases the hydrogen permeability. In this study, prior to permeation experiments, the membrane was activated by heating at 673 K in helium for 4 hours and then in hydrogen atmosphere for 10 hours. The permeation experiments were carried out using high purity test gas mixture of helium (purity 99.999%) and hydrogen (purity 99.999%) and deuterium (purity 99.96%). The feed gas mixture of a definite composition (Q_2: He = 90 : 10) was initially prepared using mass flow controllers in a standard reservoir volume of 4 liters. The gas mixture was allowed to recirculate in the volume for 1 hour for homogeneous mixing. The permeation cell was slowly heated to the desired experimental temperature at a heating rate of 10 K per minute under pure helium gas cover and the thermal equilibrium is maintained. After desired temperature is attained within ± 1 K, the helium cover gas was evacuated using the vacuum pump and the feed gas mixture was allowed to pass through the feed side of permeation cell. During permeation experiments, the partial pressure of Q_2 in the feed side is expected to decrease due to permeation through the membrane. However, in order to derive the permeation parameters, it is required to maintain the constant partial pressure of Q_2 during an isothermal experiment**.** This was achieved by using a pressure regulatory valve in the Q_2 reservoir in the feed side. The permeate side was maintained under vacuum by continuously absorbing the permeate Q_2 gas in the uranium getter bed. This ensured that the trans-membrane Q_2 pressure was kept constant during an isothermal permeation experiment. Permeation experiments were carried out at four different isothermal temperatures of 523, 573, 623 and 673 K and three different trans-membrane Q_2 pressures of 50, 100 and 150 kPa maintaining the feed gas composition at Q_2 : He = 90 :10. At any instant during the experiments, the composition of the feed gas and permeate gas was analyzed by the residual gas analyzer. The flux of hydrogen through the membranes were calculated using the mass flow meter in the permeate side.

2.4. Pressure-Composition-Isotherm generation.

The PCIs for the desorption reaction of Pd-Ag-Cu-H_2/D_2 system were generated using a constant volume Sieverts' type apparatus. These instruments are mostly used for the gas sorption studies in a material. The instrument is designed to generate the pressure-volume data with high precision. The schematic of the Sieverts' apparatus is shown in Figure 2.11. In the present study, Sieverts' type volumetric apparatus supplied by SETARAM Instrumentation, France (model PCT Pro-2000) shown in Figure 2.12, was used to generate the PCIs of H_2/D_2 desorption reactions. This is a fully automated instrument for measuring gas sorption properties of materials. It is designed for precision measurements over a broad range of pressure, temperature and sample size. It has PID controlled temperature and pressure gas handling systems for sophisticated measurements and excellent process control. The instrument uses an internal PID controlled pressure regulator that can operate to up to 170 bar and all gas handling components are rated up to 200 bar. It has five different calibrated gas reservoir volumes, which enables the instrument for PCT measurement on very large amount of samples. The gas handling enclosure is temperature controlled to maintain a constant temperature during gas sorption studies. The instrument is attached with a thick stainless steel reaction vessel, which is heated using PID temperature controller.

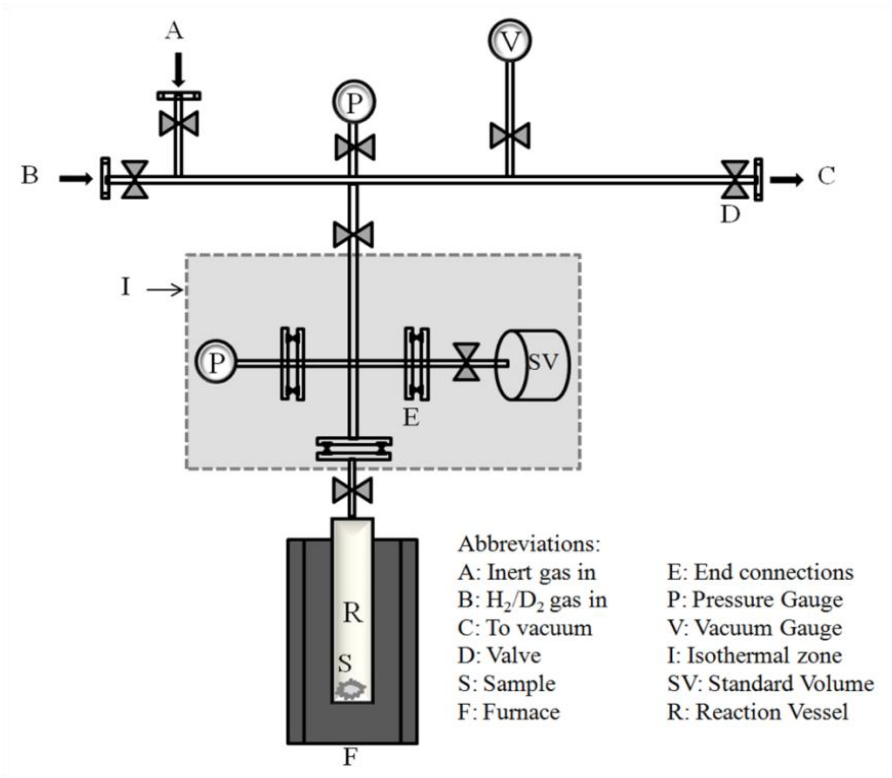

Figure 2.11. Schematic of Sieverts' apparatus

The reaction vessel is designed to be heated from room temperature to 673 K. The position of thermocouple is fixed in the reaction vessel in such a way that the measured temperature is same as the sample temperature. There are four capacitance based pressure transducers out of which two can operate on very high pressure up to 200 bar and other two operates up to 5 bar pressure. This ensures very accurate pressure measurement over a broad range. All the valves used in the instrument are pneumatically controlled valves, which allow fully automated measurement.

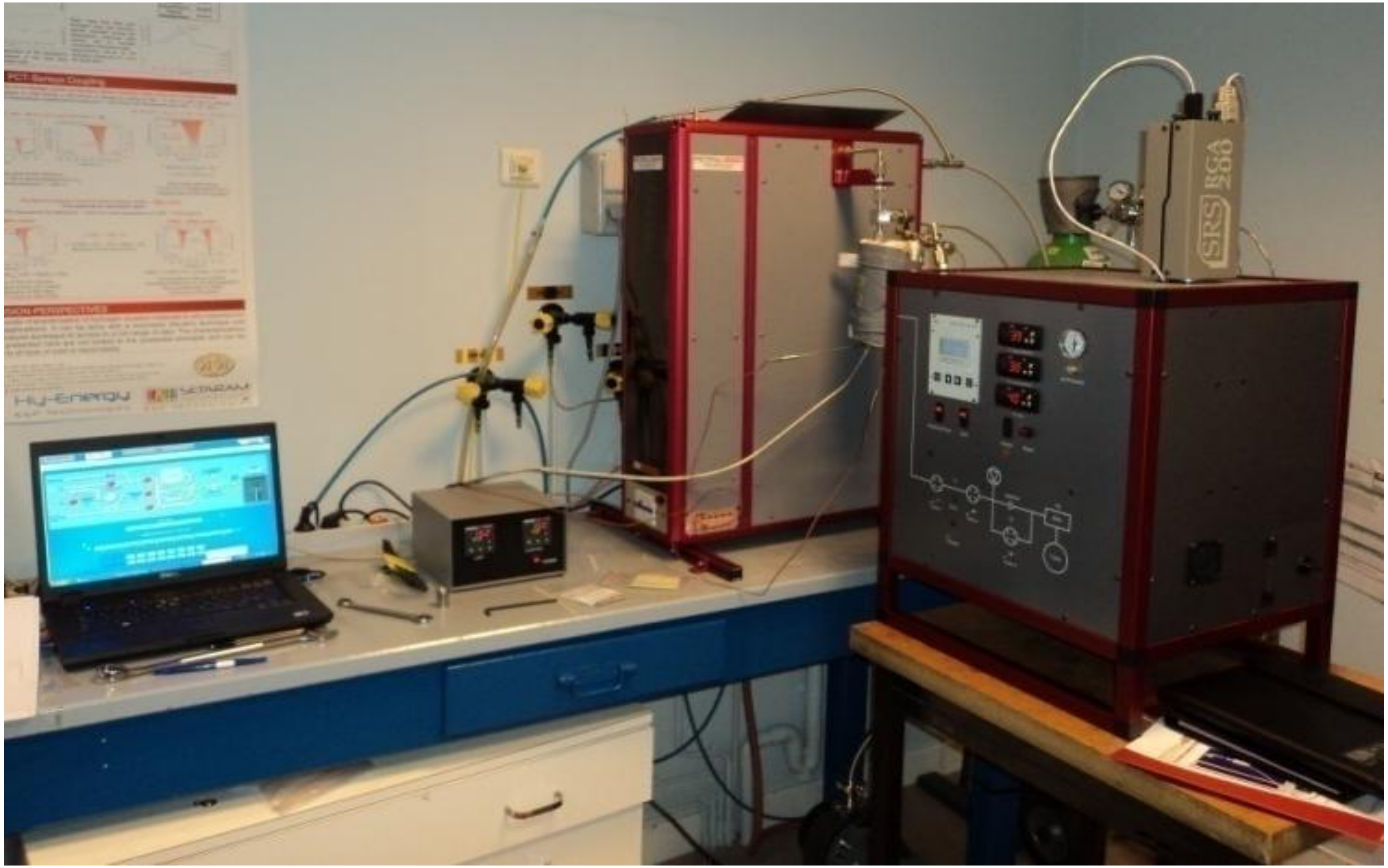

Figure 2.12. Sieverts type apparatus (PCT Pro-2000)

The instrument is process controlled using ‘Hy-Data-4.1’ software. The hydrogen/deuterium concentrations in materials are measured using pressure-volume-temperature correlations. Utmost care was taken to minimize the variation in the temperature and volumes of the gas reservoir and sample holder. Isothermal condition is maintained inside the instrument to prevent the fluctuations in volume/pressure due to variation in room temperature. Accurate volume of sample holder was measured by using helium gas at the required experimental temperatures after loading of sample. Temperatures of the gas reservoir and sample holder are controlled using the PID temperature controller with an accuracy of ±1 K. Thus, by fixing volume and temperature of the reservoir and sample holder, the pressures of the system can be measured using suitable pressure transducers [125]. The pressure-temperature and volume data were used to calculate the concentration of hydrogen in the sample. For accurate measurements of hydrogen/deuterium concentration for generation of PCIs, the NIST Standard Reference Database [126] containing the latest compressibility factors for different gases were used. These NIST database are inbuilt in the software Hy-Data-4.1. The data processing was carried out using IGOR-Pro software.

When hydrogen gas is allowed to react with the alloy, it is absorbed by the material and the pressure of hydrogen decreases. If ΔP is the pressure drop due to absorption of hydrogen by sample, the concentration of hydrogen in the sample is calculated as:

$$n = PV/RT \tag{2.3}$$

where, n is moles of hydrogen, V is the volume of system at T is temperature in kelvin and R is the gas constant.

In general, for the present PCIs, the hydrogen concentration is represented by hydrogen to formula unit of the sample (H/f.u.).

$$\mathrm{H/f.u.} = n/n_s \tag{2.4}$$

where, n_s is the moles of sample alloy.

Presence of contaminants on the surface of the alloy affects the hydride/deuteride formation by blocking the active sites. The contaminating species may be oil or organic residues or the intrinsic oxide layer formed on the surface of the metal/alloy. These contaminants decrease the kinetics of hydrogen sorption reaction and the hydrogen absorption capacity. Hence, there is a need to breach this passive surface layer before carrying out actual measurements. This preliminary step is termed as activation. In this step, repeated hydriding/dehydriding cycles were carried out by applying different thermal treatment to the alloy. The alloy is said to be activated when the absorption capacity of the alloy becomes constant for a repeated number of cycles. Prior to PCT measurements on actual systems, the accuracy of Sieverts' type volumetric apparatus was checked by performing the PCT measurements on palladium metal.

The alloy samples used in the present investigation were first loaded into Sieverts' type volumetric apparatus. The samples were degassed under high vacuum with a base pressure of 10^{-4} mbar for 2 h followed by a preheat treatment in a flow of helium with 4% hydrogen at 773 K for 2 h. Thereafter, the alloy was allowed to react with high pure hydrogen gas (99.999% purity) at a known pressure at room temperature. Pressure drop was noticed as the hydride formation takes place, after the sample complete hydriding the sample was degassed at 573 K. In a similar manner, repeated hydriding-dehydriding cycles were carried out. The total pressure drop was monitored and the concentration of hydrogen absorbed was calculated using pressure volume relationship. After ~ 15 cycles, reproducible measurements were obtained.

The activated samples were used for PCI measurements without removing from the reaction vessel. A similar procedure was followed for measurements with high purity deuterium gas (99.999% purity) and with a different set of samples. A known amount of activated alloy was loaded in to the reaction vessel of known volume of the Sieverts' apparatus and allowed to react with hydrogen/deuterium at ambient temperature and a known initial pressure. Absorption of hydrogen/deuterium by the alloy resulted in a pressure drop which was measured using a capacitance manometer. From the pressure and volume data, the composition (X/f.u., where f.u. is formula unit, X = H or D) of the hydride/deuteride phase was calculated. In order to generate the pressure-composition isotherm (PCI), this hydride/deuteride phase was heated to the desired experimental temperature under a known over-pressure of hydrogen/deuterium in the system. The attainment of equilibrium was ascertained when the change in pressure was observed to be less than 10 Pa for a period of 30 min. Thereafter, a known amount of hydrogen/deuterium was removed from the reservoir and the system was allowed to attain a new equilibrium corresponding to different X/f.u. The complete desorption isotherm was generated by sequential liquating of known amount of hydrogen/deuterium from the reservoir. The generation of PCI by sequential liquating is show in Figure 2.13. The upper part of the figure represents number of desorption cycles by removing small over pressure from the sample.

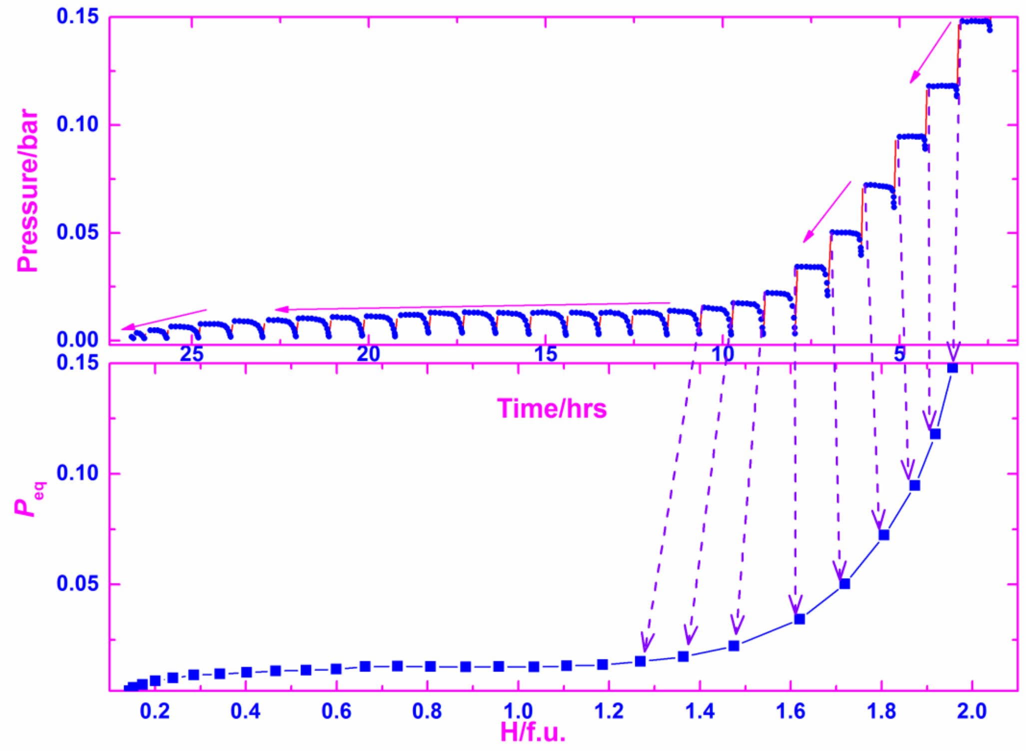

Figure 2.13. Generation of PCI for Pd-alloy

The last point of each hydrogen desorption curve provides the concentration of hydrogen in the material at that temperature and equilibrium hydrogen pressure. Thus, by joining the last point of each desorption curve and calculating the corresponding hydrogen concentration, a PCI can be generated as shown in the figure. Following this procedure, PCIs for Pd-Ag-Cu -H_2/D_2 systems were generated in the temperature range of 374 - 419 K with a step of 15 K. The equilibrium pressure data at different temperatures were used to derive the thermodynamic parameters.

2.5. Kinetic measurements

The kinetic measurements were performed using the above mentioned Sieverts' apparatus. The activated alloy was loaded in the reaction vessel of the apparatus and degassed at 673 K for 2 hours under high vacuum (10^{-4} mbar) conditions. Thereafter, the sample was cooled to the desired experimental temperature and allowed to reach the thermodynamic equilibrium. The samples were allowed to react with high pure (99.99%) hydrogen/deuterium under isothermal condition. The initial hydrogen/deuterium pressure was selected considering the hydrogen/deuterium desorption pressure of the alloys at that temperature. The initial gas pressure was feed with an accuracy of 2 %. The pressure drop due to absorption with time was recorded using the manometer gauge. The reaction was continued for sufficient time until complete hydride formation takes place. This was noticed by no further decrease in the pressure. Following this procedure, the hydrogen/deuterium absorption kinetic measurements were carried out in the temperature range of 335 - 394 K with a step of 20 K for Pd-Ag-H_2/D_2 and 303-333 K with a step of 10 K for Pd-Ag-Cu -H_2/D_2 system. The temperature-dependent rate constants were calculated by fitting these kinetic data into a suitable kinetic model. The activation energies of hydrogen/deuterium absorption reactions were derived by employing the Arrhenius equation.

CHAPTER 3

RESULTS AND DISCUSSION

Chapter 3. Results and discussion

3.1. Characterization of alloys prepared by metallurgical route

3.1.1. Compositional analysis by TXRF method

The compositional analysis of the synthesized alloys was carried out using TXRF technique. The relative mass fraction (C_x) of an element 'x' is determined by using the formula [127]:

$$C_x = \{(I_x/S_x) / \sum (I_i/S_i)\} \times 100 \qquad (3\text{-}1)$$

where, I_x and S_x are the net intensity and relative sensitivity of the element ‘x’ present in the sample, I_i and S_i are the net intensity and the relative sensitivity of all the elements ‘i’ present in the sample. The net intensities of all elemental X-ray lines are calculated by taking the area under the curve for each element. The relative sensitivity with respect to standard was calculated by dividing the absolute sensitivity of each element with the standard. The mass fractions obtained from the TXRF measurement of alloys confirm the composition of alloys as $Pd_{0.77}Ag_{0.23}$ and $Pd_{0.77}Ag_{0.10}Cu_{0.13}$.

3.1.2. X-ray diffraction analysis

3.1.2.1. Room temperature XRD patterns

The room temperature X-ray diffraction patterns of Pd, $Pd_{0.77}Ag_{0.23}$ and $Pd_{0.77}Ag_{0.10}Cu_{0.13}$ are shown in Figure 3.1. The XRD patterns confirm the formation of the alloys. The XRD patterns of the alloys are compared with the patterns reported in the JCPDS (Joint committee on powder diffraction standards) files. This reveals that both the alloys form face centered cubic crystallographic structure similar to Pd. It is also evident from the figure that the Bragg reflection lines of alloys closely match with those of palladium with a systematic shift in reflection angles thereby, confirming the f.c.c phase formation in both the alloys.

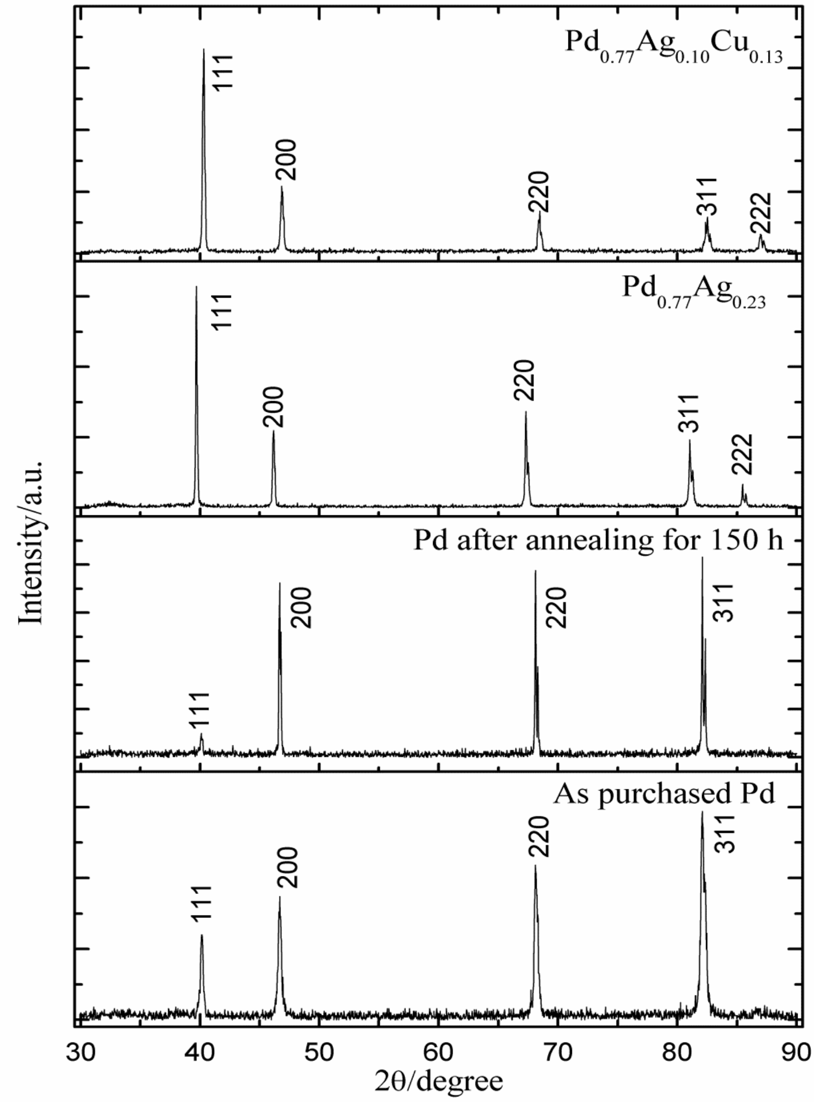

Figure 3.1. Room temperature XRD pattern of Pd, Pd$_{0.77}$Ag$_{0.23}$ and Pd$_{0.77}$Ag$_{0.10}$Cu$_{0.13}$ alloys

Further, XRD patterns of both the alloys show the absence of impurity phases. In case of the binary Pd$_{0.77}$Ag$_{0.23}$ alloy, the reflection lines are shifted to lower 2θ angles compared to Pd indicating lattice expansion. However, for Pd$_{0.77}$Ag$_{0.10}$Cu$_{0.13}$ alloy, the reflection lines are shifted to higher angles indicating lattice contraction compared to pure palladium. In case of pure palladium, the reflection from plane (3 1 1) had maximum intensity compared to all other indicating preferred orientation in the sample. The sample was further annealed at 1073 K for about 150 h and cooled slowly to room temperature and the XRD pattern was again recorded. However, the pattern remained same as that of the original sample. For both the alloys the intensity patterns do not indicate preferred orientation.

The lattice parameters of Pd, $Pd_{0.77}Ag_{0.23}$ and $Pd_{0.77}Ag_{0.10}Cu_{0.13}$ were calculated by indexing the reflection lines using SAX analysis and Unit Cell WIN software [128]. The room temperature lattice parameters of Pd, $Pd_{0.77}Ag_{0.23}$ and $Pd_{0.77}Ag_{0.10}Cu_{0.13}$ obtained in this study along with data reported in the literature [129-131] are listed in Table 3-1. In addition, the calculated values of lattice parameters of Pd-Ag solid solutions using Vegard's law are listed in Table 3-1 for comparison. All these values show excellent agreement.

Table 3-1. Lattice parameters of Pd alloys

System	Lattice parameter(nm)	Reference
Pd	0.3890±0.0001	This study
	0.389	[129]
$Pd_{0.77}Ag_{0.23}$	0.3931±0.0001	This study
	0.3931	Vegard’s Law
	0.3929	[130]
$Pd_{0.77}Ag_{0.10}Cu_{0.13}$	0.3874±0.0001	This study
	0.3874	Vegard’s Law
	0.3878	[131]

It is evident from the table that addition of Ag to Pd increases the lattice constant of the alloy, whereas the addition of Cu to Pd-Ag decreases its unit cell size. The observation in shrinkage in the unit cell volume of the ternary alloy compared to the binary is in consistence with the smaller lattice constant of Cu compared to Pd and Ag.

3.1.2.2. High temperature XRD patterns

In the present investigation, the high temperature XRD patterns of Pd, $Pd_{0.77}Ag_{0.23}$ and $Pd_{0.77}Ag_{0.10}Cu_{0.13}$ alloys recorded in the temperature range of 298-1023 K, are shown in Figure 3.2, Figure 3.3 and Figure 3.4, respectively. It is observed from the figures that the two alloys $Pd_{0.77}Ag_{0.23}$ and $Pd_{0.77}Ag_{0.10}Cu_{0.13}$ retain the single f.c.c phase even up to a temperature of 1023 K. A systematic shifting of the reflection lines towards higher 2θ angle is observed. This shifting of the reflection lines indicates the expansion in the unit cell size of the alloys. The high temperature lattice parameters were calculated indexing the reflection lines of the XRD patterns at each temperature and the variation of lattice parameters as a function of temperature for Pd, $Pd_{0.77}Ag_{0.23}$ and $Pd_{0.77}Ag_{0.10}Cu_{0.13}$ are shown in Figure 3.5. For pure Pd, the high temperature lattice parameters are compared with those reported in literature [129, 133]. For $Pd_{0.77}Ag_{0.23}$ and $Pd_{0.77}Ag_{0.10}Cu_{0.13}$, there is no experimental high temperature lattice parameter data in the literature for comparison.

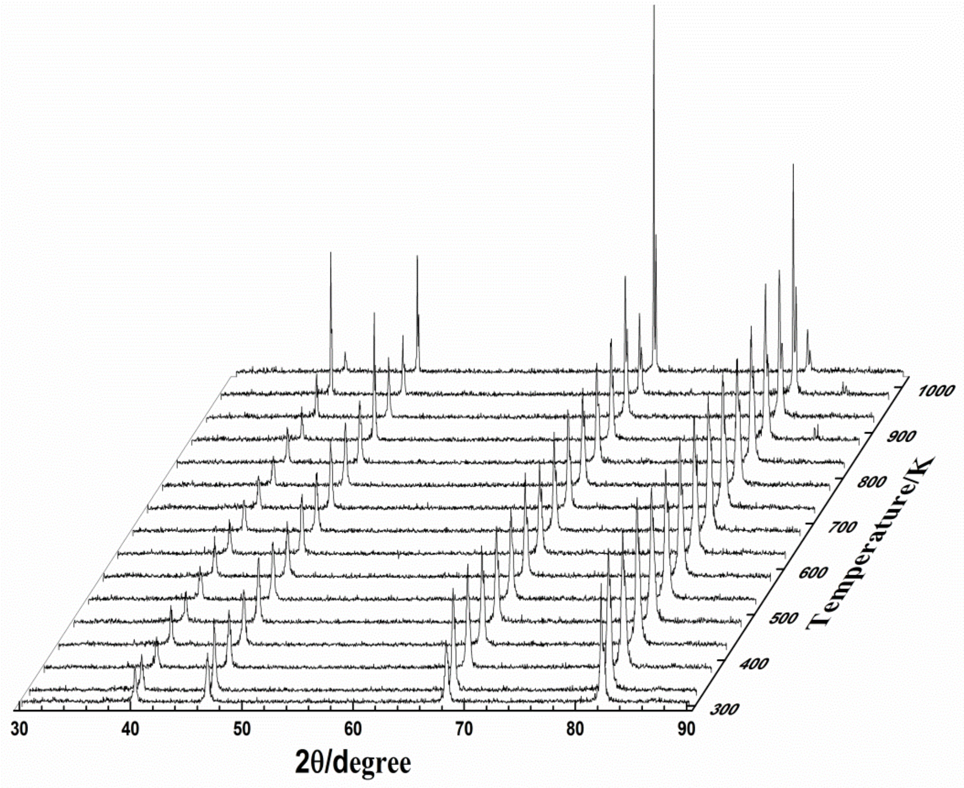

Figure 3.2. High temperature XRD pattern of Pd

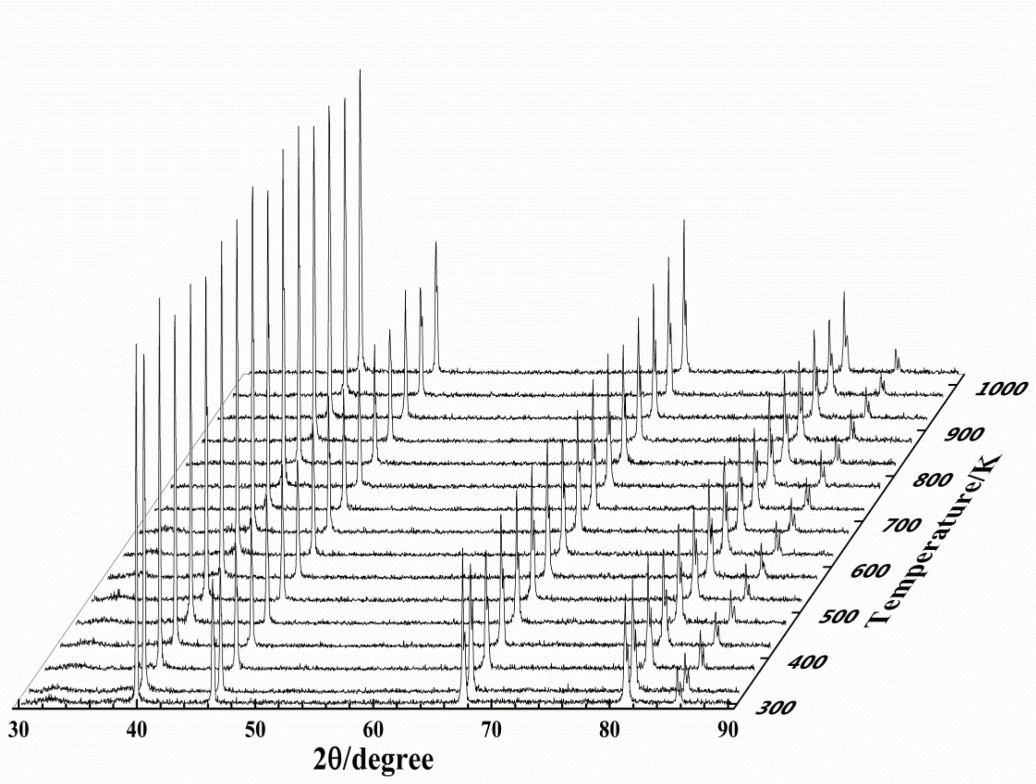

Figure 3.3. High temperature XRD patterns for $Pd_{0.77}Ag_{0.23}$ alloy

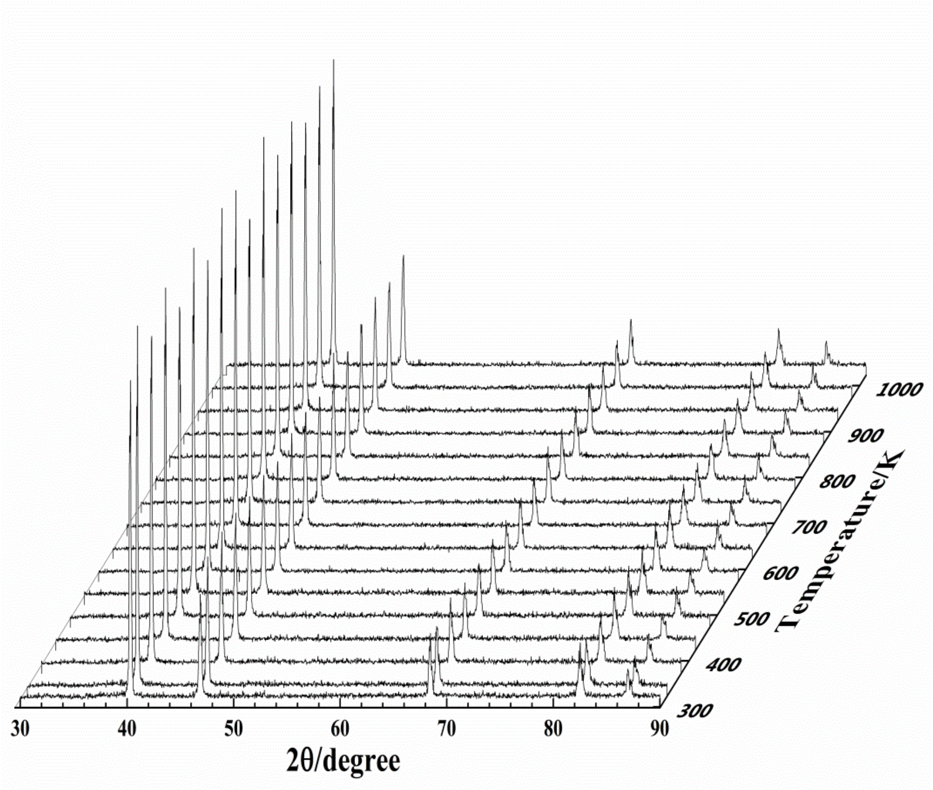

Figure 3.4. High temperature XRD patterns of $Pd_{0.77}Ag_{0.10}Cu_{0.13}$ alloy

The lattice constants of both the alloys as a function of temperature was also calculated using Vegards law. For $Pd_{0.77}Ag_{0.23}$ and $Pd_{0.77}Ag_{0.10}Cu_{0.13}$ alloys, the Vegard's law relation can be written as:

$$a(Pd_{0.77}Ag_{0.23}) = 0.77 \cdot a_{Pd} + 0.23 \cdot a_{Ag} \quad (3\text{-}2)$$

$$a(Pd_{0.77}Ag_{0.10}Cu_{0.13}) = 0.77 \cdot a_{Pd} + 0.10 \cdot a_{Ag} + 0.13 \cdot a_{Cu} \quad (3\text{-}3)$$

where, a_{Pd}, a_{Ag}, a_{Cu} are the lattice constants of Pd, Ag and Cu, respectively.

The values of a_{Pd} are taken from the present experimental data where as those for a_{Ag}, a_{Cu} are taken from Suh et al. [132]. The calculated values of lattice constants as a function of temperature and those derived using Vegard's law are compared in Figure 3.5. From the figure it can be observed that both the alloys show negative deviation from Vegard's law.

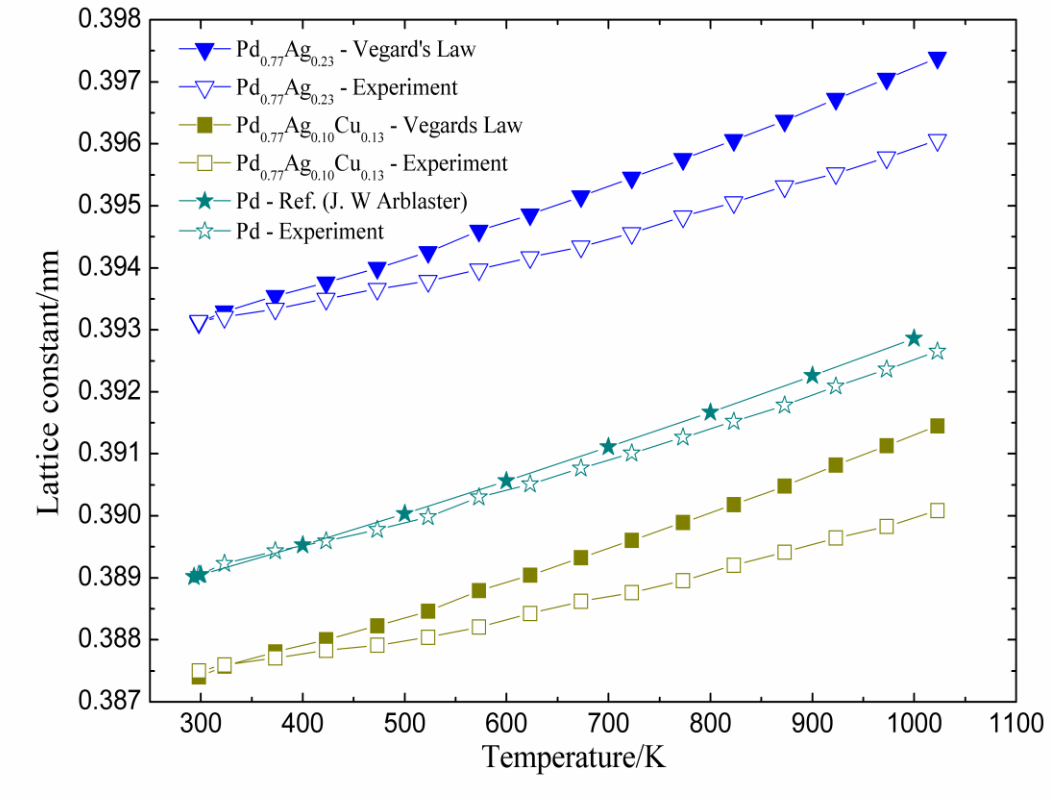

Figure 3.5. Variation of lattice parameter as a function of temperature

Our experimental data on lattice constant of Pd is systematically lower than that of reported in literature [129] and the maximum deviation is 0.05%. It has been seen that using either of our experimental data or data from literature for palladium, in both the cases, similar deviation from Vegard’s law is observed. The experimental observation of lattice contraction for $Pd_{0.77}Ag_{0.10}Cu_{0.13}$ and lattice expansion for $Pd_{0.77}Ag_{0.23}$ compared to pure Pd is consistent with predictions from Vegard’s law.

3.1.2.3. Liner thermal expansion coefficient

The variation of lattice constant (a_T) with temperature for Pd, $Pd_{0.77}Ag_{0.23}$ and $Pd_{0.77}Ag_{0.10}Cu_{0.13}$ best fits to a second order polynomial of the form [134]:

$$a_T = A + BT + CT^2 \qquad (3\text{-}4)$$

The values of fitting parameters A, B and C are listed in Table 3-2. The coefficient of linear thermal expansion (α_T) can be expressed as [134]:

$$\alpha_T = (1/a_{298})\cdot d(a_T)/dT \qquad (3\text{-}5)$$

where, a_{298} is the lattice constant at a reference temperature of 298 K. The variation of α with temperature calculated using equation (3.5) is shown in Figure 3.6. The temperature dependency of coefficient of linear thermal expansion in the temperature range of 298-1023 K can be represented by a general equation of the type [134]:

$$\alpha_\mathrm{T} = \mathrm{C}_1+\mathrm{C}_2T \qquad (3\text{-}6)$$

where, C_1, C_2 are related to the parameters B and C as: $\mathrm{C}_1 = \mathrm{B}/a_{298}$ and $\mathrm{C}_2 = 2\mathrm{C}/a_{298}$. The values of C_1, C_2 and average value of coefficient of thermal expansion are given in Table 3-2. It can be observed from the figure that coefficient of thermal expansion (α) varies linearly with temperature which is due to the increase in lattice anharmonicity with rise in temperature.

Table 3-2. Fitting parameters of equations (3-4) and (3-6) and average value of coefficient of linear thermal expansion (α_{av})

System	Parameters for Eq. (3-4)			Parameters for Eq. (3-6)		$\alpha_{av}/10^{-6}$ K^{-1}
	A	$\mathrm{B}/10^{-6}$	$\mathrm{C}/10^{-9}$	$\mathrm{C}_1/10^{-6}$	$\mathrm{C}_2/10^{-9}$	
Pd	0.39259	3.0722	1.3994	7.897	7.193	12.65
$\mathrm{Pd}_{0.77}\mathrm{Ag}_{0.23}$	0.38804	1.1756	2.1652	2.918	11.114	10.24
$\mathrm{Pd}_{0.77}\mathrm{Ag}_{0.10}\mathrm{Cu}_{0.13}$	0.38707	0.8849	2.0329	2.187	10.624	9.32

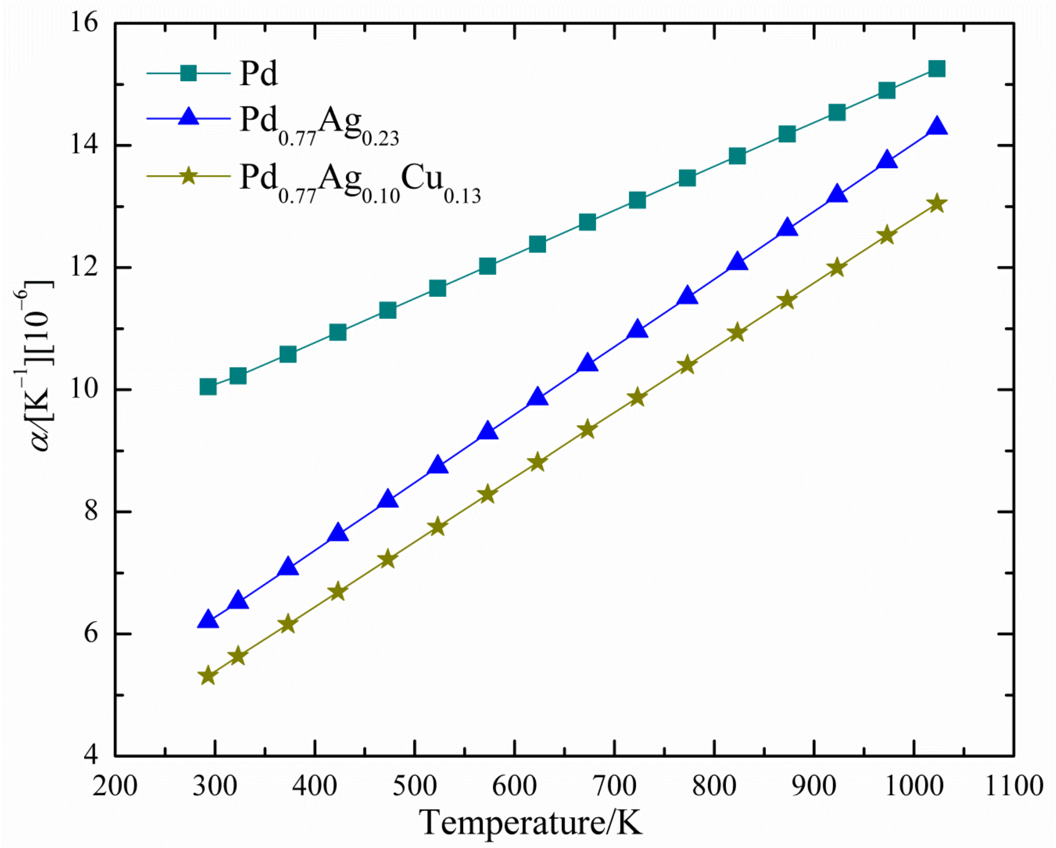

Figure 3.6. Variation of coefficient of linear thermal expansion with temperature

In case of pure palladium, value of α_T varies from 10.04×10^{-6} K^{-1} to 15.25×10^{-6} K^{-1} within the temperature range of 298 to 1023 K with an average value of 12.65×10^{-6} K^{-1}. Thermal expansion of pure palladium has been determined by Dutta and Dayal [133] by using high temperature X-ray camera in a temperature range of 298 to 1151 K and the value α_T was found to vary from 11.74×10^{-6} K^{-1} to 17.76×10^{-6} K^{-1}.The average linear thermal expansion coefficient between 298 K and 618 K obtained by them [133] is 12.58×10^{-6} K^{-1}. Owen and Jones [135] have investigated thermal expansion of pure palladium, and found the mean coefficient of linear thermal expansion in a temperature range of 273 to 573 K to be 12.7×10^{-6} K^{-1}. The mean coefficient of thermal expansion of pure palladium obtained in the present study is in excellent agreement with all these reported values.

The value of α_T for the binary alloys $Pd_{0.77}Ag_{0.23}$ obtained in this study varies from 6.21×10^{-6} K^{-1} to 14.28×10^{-6} K^{-1} and the average value is 10.24×10^{-6} K^{-1}. Ziya et al. [136] have reported the value of α_T for $Pd_{0.50}Ag_{0.50}$ alloy which varies from 9.3×10^{-6} K^{-1} to 14.6×10^{-6} K^{-1} in the temperature range of 308 to 1178 K by using X-ray diffraction technique. The value of α_T for the ternary alloy $Pd_{0.77}Ag_{0.10}Cu_{0.13}$ obtained in this study is found to vary from 5.31×10^{-6} K^{-1} to $13.05 \times 10^{-6} K^{-1}$ and the average value is 9.32×10^{-6} K^{-1}. Coefficient of linear thermal expansion for pure palladium, binary $Pd_{0.77}Ag_{0.23}$ alloy and ternary $Pd_{0.77}Ag_{0.10}Cu_{0.13}$ alloy obtained in this study follows the trend: α_T (Pd) > α_T ($Pd_{0.77}Ag_{0.23}$) > α_T ($Pd_{0.77}Ag_{0.10}Cu_{0.13}$).

The results show that the coefficient of linear thermal expansion of palladium decreases upon alloying. The ternary alloy has least value of α compared to pure metal and binary alloy at all experimental temperatures. The average values of α_T for SS 304 and SS 316 are 17.3×10^{-6} K^{-1} and 16.0×10^{-6} K^{-1}, respectively [137]. The variation in α_T between these Pd alloys and SS materials is between 25 to 45 %. Hence, coating of palladium and its alloys on SS substrates may delaminate after successive thermal cycling during hydrogen purification using coated palladium based membranes.

3.1.2.4. X-ray Debye temperatures of $Pd_{0.77}Ag_{0.23}$ and $Pd_{0.77}Ag_{0.10}Cu_{0.13}$ alloys

Debye temperatures are frequently used to characterize the thermal vibrations (phonon modes) of solids and are found to be useful in a number of physical properties of solids. There are different methods of finding the Debye temperatures like measurement of sound velocities, specific heats, phonon dispersion relation from neutron scattering method and X-ray diffraction method; all the methods have their own merits and limitations depending on the temperature range of measurement and type of crystal lattice. In the present study, the Debye temperatures of $Pd_{0.77}Ag_{0.23}$ and $Pd_{0.77}Ag_{0.10}Cu_{0.13}$ alloys have been calculated from high temperature X-ray diffraction data. Debye temperature for palladium could not be calculated due to the preferential orientation of (3 1 1) plane. The integrated intensities of Bragg reflection lines have been measured over a wide temperature range. The method of calculation of Debye temperature is similar to that reported by James [138]. The integrated intensity of a Bragg reflection depends on the specimen temperature. The intensity is reduced relative to the absolute zero value by the Debye-Waller factor, $\exp(-2M)$ where, the expression for $2M$ is given below [138].

$$2M = (12h^2/mk_B\Theta_M)\cdot\{(F(x)/X) + 1/4\}\,(\sin\theta/\lambda)^2 \tag{3-7}$$

$$F(X) = (1/X)\cdot\int(\xi\cdot d\xi)/(\exp(\xi)-1);\ X = \Theta_M/T$$

$$\text{(within the limit from 0 to } X\text{)} \tag{3-8}$$

where, m is the mass of the atom (or reduced mass in case of molecule), h is Planck's constant, k_B is the Boltzmann's constant, θ is the Bragg angle, λ is the wavelength of X-ray, $F(X)$ is the Debye function, Θ_M is the X-ray Debye temperature and T is the absolute temperature. Writing equation (3.7) for two different temperatures T_1 and T_2 and rearranging one can get the following expression:

$$2M\,(T_2) - 2M\,(T_1) = \ln\{I(T_1)_{\text{observed}}/\,I(T_2)_{\text{observed}}\} \tag{3-9}$$

Initially, the value of $2M\,(T_1)$ at the reference temperature of 298 K is calculated using a 'guessed' value of Θ_M and the corresponding value of $F(X)$ from the international tables for X-ray crystallography [139]. The obtained values of $2M\,(T_1)$ along with the integrated intensities from experiments are then used to calculate $2M\,(T_2)$ using equation (3-9), from which the X-ray Debye temperature at T_2 is calculated. This procedure is repeated in an iterative manner with different initial values of Θ_M to yield self-consistent value of the X-ray Debye temperature. A family of curves is obtained depending upon the choice of $\Theta_M(T_1)$, the most acceptable one is that which gives consistent value of Θ_M over the experimental temperature range [140]. In this case the integrated intensity data of higher diffraction angle ((2 2 2) plane) was used for calculation of Debye temperature, because of better temperature dependency of higher angles compared to lower diffraction angles. The calculated values of the X-ray Debye temperatures for $Pd_{0.77}Ag_{0.23}$ and $Pd_{0.77}Ag_{0.10}Cu_{0.13}$ alloys along with available literature reported data for Pd [140], Ag [141], Cu [141] and Pd-Ag alloys [136,140,142] are summarized in Table 3.3. The variation of Debye temperature as a function of absolute temperature for $Pd_{0.77}Ag_{0.23}$ and $Pd_{0.77}Ag_{0.10}Cu_{0.13}$ alloys is shown in Figure 3.7 and Figure 3.8, respectively. It is evident from the figures that the X-ray Debye temperatures of both $Pd_{0.77}Ag_{0.23}$ and $Pd_{0.77}Ag_{0.10}Cu_{0.13}$ alloys show initial decrease followed by a rise with increase in absolute temperature. The increase in the value of Θ_M for both alloys with increase in temperature may be due to the anharmonic lattice vibration with rise in temperature. For the alloy $Pd_{0.77}Ag_{0.23}$, the curve corresponding to 225 K gives consistent value of Θ_M over all temperature ranges and all other curves diverge to this value of Θ_M. Similarly for the alloy $Pd_{0.77}Ag_{0.10}Cu_{0.13}$, the curve around temperature 165 K gives consistent values of Θ_M. Hence, the X-ray Debye temperature of $Pd_{0.77}Ag_{0.23}$ alloy is estimated to be 225±10 K and for $Pd_{0.77}Ag_{0.10}Cu_{0.13}$ alloy is165 ±10 K. The value of X-ray Debye temperature of $Pd_{0.77}Ag_{0.23}$ alloy is found to be higher than that for $Pd_{0.77}Ag_{0.10}Cu_{0.13}$ alloy.

Table 3-3. Comparison of X-ray Debye temperatures of $Pd_{0.77}Ag_{0.23}$ and $Pd_{0.77}Ag_{0.10}Cu_{0.13}$ alloys with the corresponding elements

System	X-ray Debye temperature/ K	Reference
Pd	290	[140]
Ag	226	[141]
Cu	345.6	[141]
$Pd_{0.80}Ag_{0.20}$	308.6	[142]
$Pd_{0.77}Ag_{0.23}$	225±10	This study
$Pd_{0.75}Ag_{0.25}$	280	[140]
$Pd_{0.70}Ag_{0.30}$	302	[142]
$Pd_{0.50}Ag_{0.50}$	275	[142]
$Pd_{0.50}Ag_{0.50}$	219, 239	[136]
$Pd_{0.77}Ag_{0.10}Cu_{0.13}$	165±10	This study

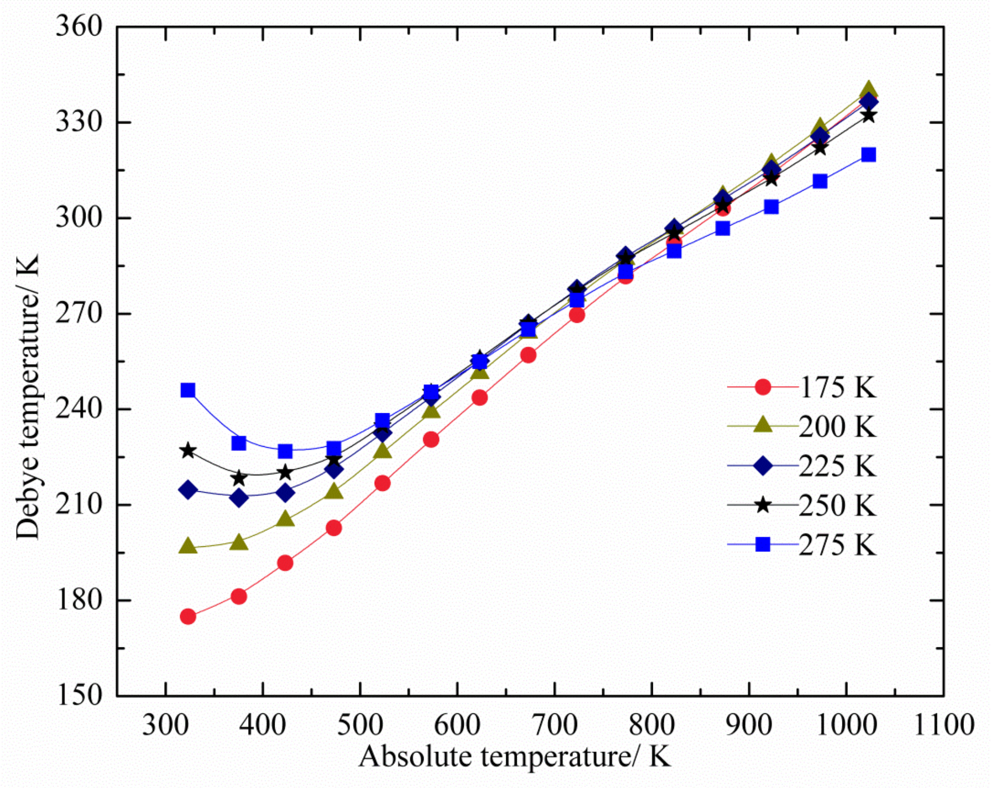

Figure 3.7. Variation of Θ_M as a function of T for $Pd_{0.77}Ag_{0.23}$ alloy

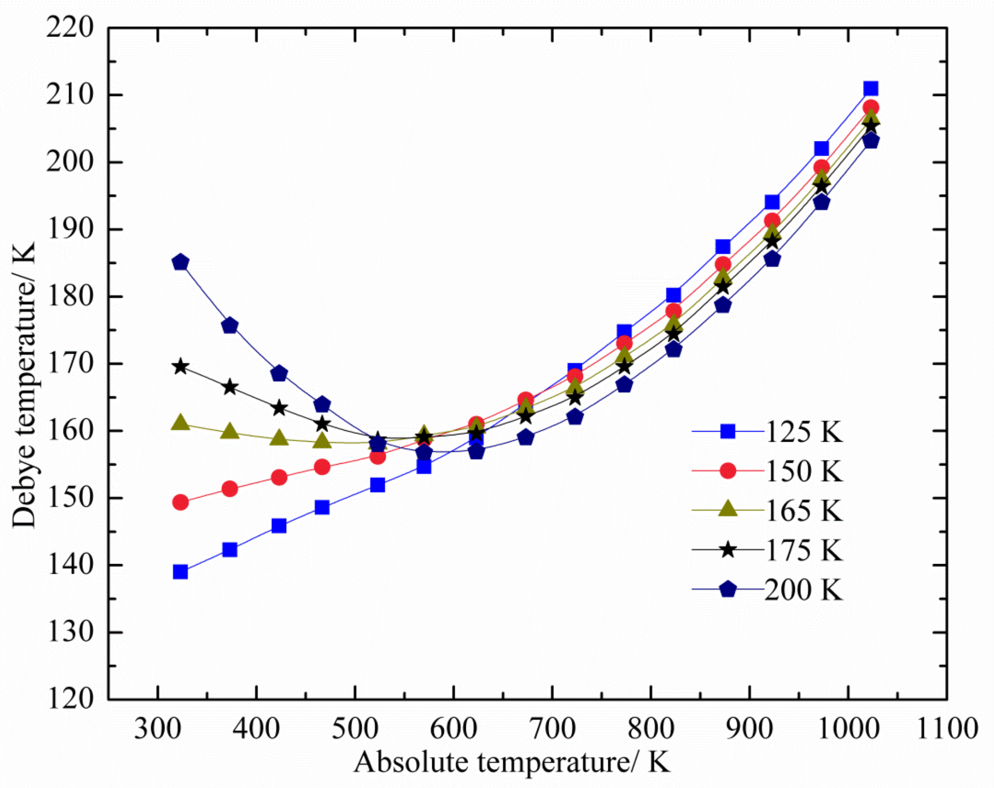

Figure 3.8. Variation of Θ_M as a function of T for $Pd_{0.77}Ag_{0.10}Cu_{0.13}$ alloy

3.2. Preparation and characterization of membrane by electroless plating method

The joints of PSS disc with NPSS tube using laser welding and electron beam welding techniques were characterized by SEM. The SEM images of joints are shown in Figure 3.9. It can be clearly visualized that the laser welding and EB welding results in crack free joints.

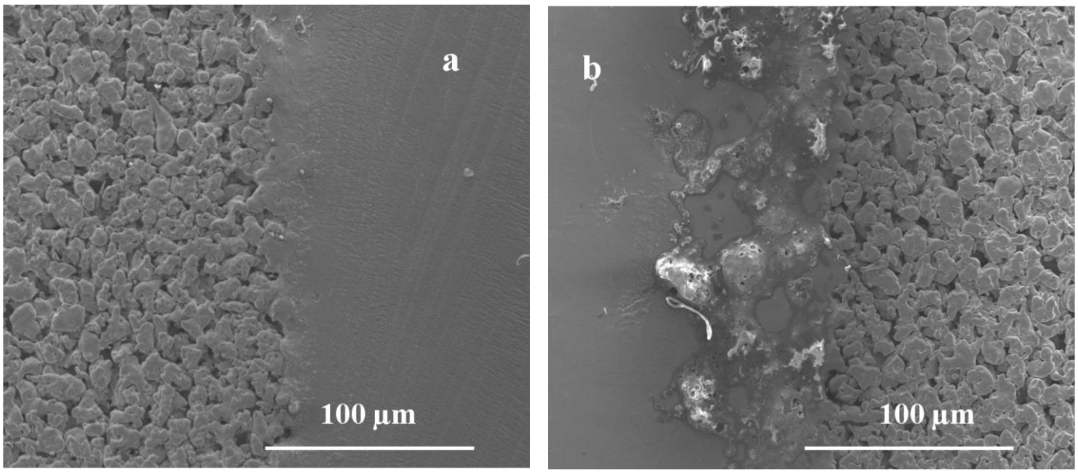

Figure 3.9. (a) SEM image of laser weld joint (b) SEM image of electron beam weld joint

3.2.1. Electroless plating of Pd based membranes

In the present study, Pd, Pd-Ag and Pd-Ag-Cu membranes were deposited over porous stainless steel substrate by electroless plating method using different plating baths. During the plating experiments, it was observed that the plating efficiency strongly depends upon bath stability, which eventually depends upon several parameters like temperature, pH, addition of reducing agent and nature of plating solution. Both temperature and pH of the solution play important role in the stability of the plating bath. It was observed that a small variation in these two parameters significantly affects the bath stability and results in bulk precipitation. The consumption of OH^- ion during the experiment and evaporation losses of NH_4OH results in decrease in pH of the plating bath. Therefore, to maintain the pH constant, NH_4OH was continuously added to the plating solution of Pd and Ag baths. In case of Cu deposition, it was observed that with increase in the pH of solution the rate of metal deposition increases but above a certain value (pH ≥ 11.5) the rate of deposition decreases. This is ascribed to the hydrolysis of formaldehyde at higher pH to form methylene glycol ions, which further oxidizes to formate ion according to the following reactions:

$$HCHO + OH^{(-)} \rightarrow CH_2(OH)O^{(-)} \qquad (3\text{-}10)$$

$$CH_2(OH)O^{(-)} + OH^{(-)} \rightarrow CHOO^{(-)} + H_2O + e^{(-)} \qquad (3\text{-}11)$$

Similar type of results has been observed by F. Hanna et al. [143] during electroless copper deposition. Further, it was observed that freshly prepared solution yields efficient and homogenous plating and controls the bath chemistry whereas use of stock solution destabilizes the bath and reduces the plating efficiency. As described previously, activation of the substrate surface is important for better adherence and homogenous plating. Hence, the substrate was properly activated each time before plating experiment. Several additives such as reducing, complexing and stabilizing agents also affect the rate of metal deposition. Bulk addition of the reducing agent results in bath destabilization and precipitation of the metal particles in the solution. Hence, stepwise addition of the reducing agent was carried out to maintain the bath stability. Stirring was found to have positive effect on the plating conditions. The effect of these experimental parameters on plating efficiency are summarized below in Table 3-4.

Table 3-4. Parameters of plating experiments

Nature of solution	T (K)		pH of bath		Addition of reducing agent	Effect on plating
	Pd/Ag	Cu	Pd/Ag	Cu		
Fresh solution	333	298	8	9	Bulk addition	Bath destabilization no plating
-do-	333	298	9	10	Bulk addition	Bath destabilization no plating
-do-	333	298	10	11	Bulk addition	Bath destabilizes after few minutes of plating
-do-	333	298	11	12	Bulk addition	Bath destabilization no plating
Fresh solution	333	298	8	9	Stepwise addition	Bath destabilization no plating
-do-	333	298	9	10	Stepwise addition	Bath destabilizes after few minutes of plating
-do-	333	298	10	11	Stepwise addition	Bath stability is good and better plating
-do-	333	298	11	12	Stepwise addition	Bath destabilizes after few minutes of plating
Stock solution	Under all conditions					Bath destabilizes and no plating is observed

From all these experiments it was found, destabilization of the drastically affects the kinetics and rate of plating. Hence, optimization of all these bath parameters is necessary for an efficient metal deposition.

3.2.2. Characterization of the membrane by XRD method

Pd, Pd-Ag, Pd-Ag-Cu alloy membranes prepared by electroless plating method on PSS substrates were characterized by XRD technique. The XRD patterns of the PSS disc after Pd deposition is shown in Figure 3.10.

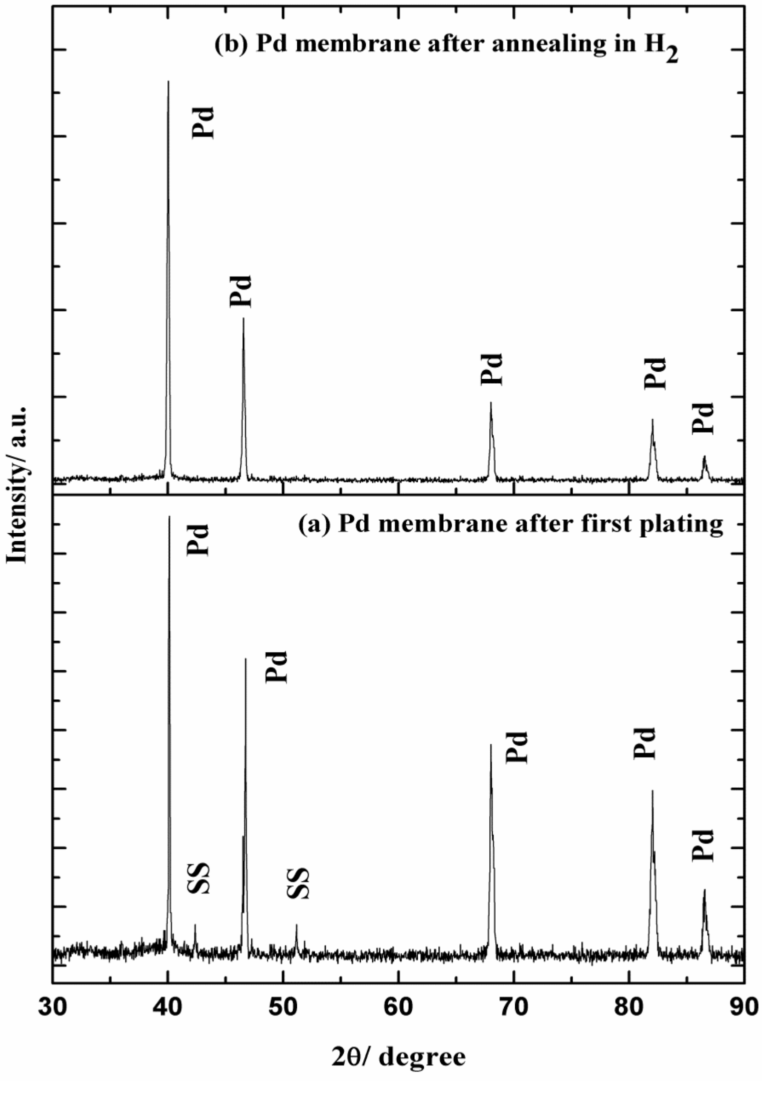

Figure 3.10. XRD patterns of Pd plated PSS disc

The figure represents two different patterns of Pd deposition: (a) XRD taken after a single plating experiment and (b) XRD after subsequent plating and annealing. It is evident from Figure 3.10(a) that along with the higher intensity reflection lines of Pd some of the less intense peaks corresponding to SS are also visible in the pattern. This may be due to the penetration of X-rays through the thin Pd layer formed after single plating. The XRD pattern of the membrane after subsequent plating and annealing is shown in Figure 3.10(b). This confirms the deposited membrane purely Pd and no impurity peaks due to SS was found after annealing experiment. Pd-Ag alloy membrane was deposited by sequential and co-deposition of metals and annealed under hydrogen and helium atmosphere for the formation of Pd-Ag solid solution. However, it was observed that during the co-deposition process, Ag deposits preferentially over Pd. This slows down the kinetics of Pd plating thereby, causing a silver rich layer deposition over PSS. Hence, sequential metal deposition was adopted for the alloy deposition. The XRD patterns at each step of sequential metal deposition and annealing under He and H_2 were recorded in order to study the alloy formation. Figure 3.11 shows the XRD patterns of Pd-Ag membrane at different steps of deposition and annealing process. The XRD pattern of membrane after sequential deposition of Pd and Ag shows that the reflection lines are due to individual Pd and Ag metal atoms. But the pattern recorded after annealing in helium atmosphere for 20 hours reveals a prominent shift in the peak positions. It is observed from the figure that the higher angle peaks have been merged to form a single peak indicating formation of solid solution by diffusion of metal atoms in lattice. On the other hand, some of the high intense peaks due to individual metals are still present in the pattern, which indicates that there is a diffusion of metals, but the two metals have not completely mixed to form an alloy. However, the XRD pattern of the membrane recorded after annealing in hydrogen atmosphere for 10 hours indicates that the peaks corresponding to individual metal atoms has been completely merged to form single phase. The Bragg’s reflection lines due to the single phase correspond to a Pd-Ag alloy having f.c.c crystal structure.

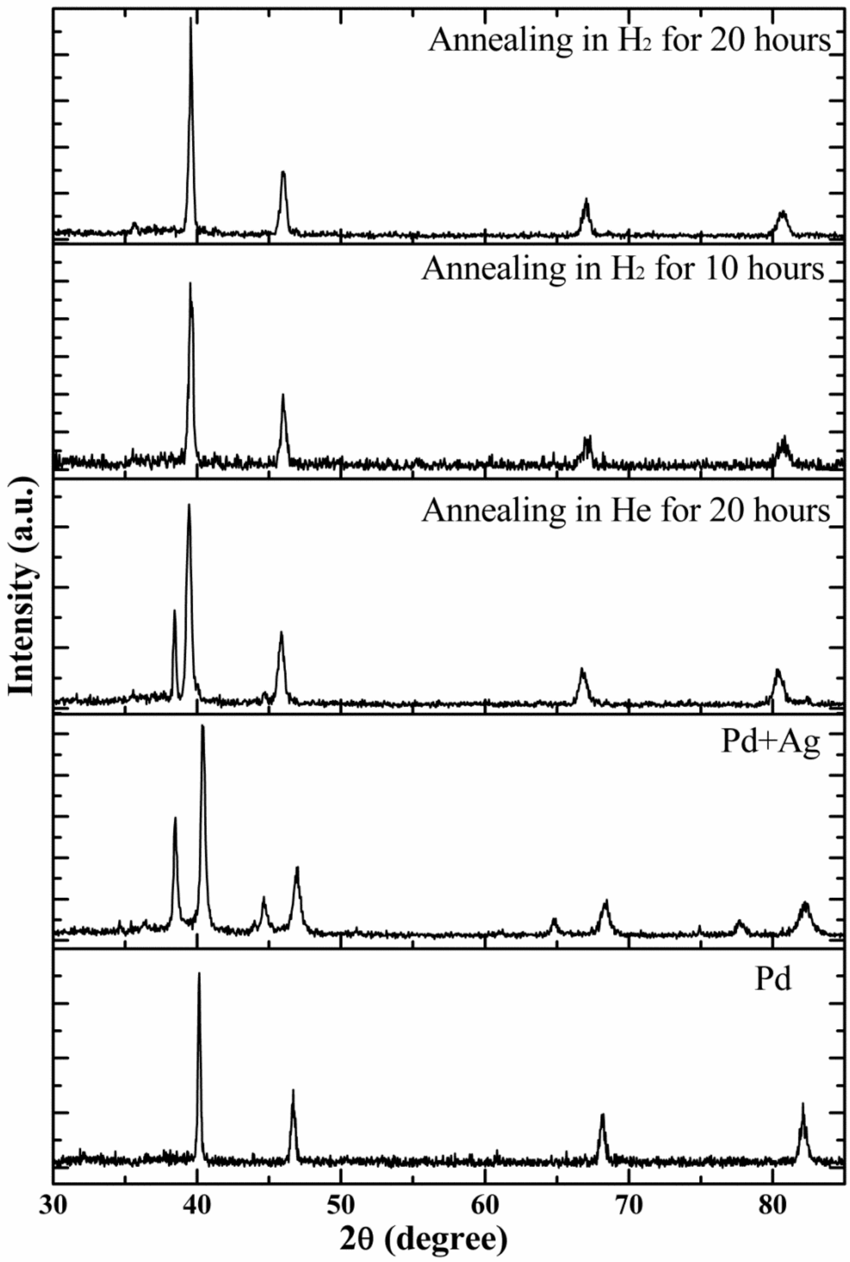

Figure 3.11. XRD patterns at different steps of Pd-Ag alloy deposition

Annealing in hydrogen atmosphere was found to be prominent because, it facilitates the thermal diffusion of metal atoms through the lattice to form a complete Pd-Ag solid solution. This process removes the thin oxide layer or any adsorbed gas molecules/volatile impurities present on the surface/grain boundaries of the deposited metal thereby, forming the alloy. Further, annealing in hydrogen for 20 hours improves the crystalinity of the lattice as is evident from the reduction of background in the XRD pattern shown in Figure 3.11.

Two ternary alloy (Pd-Ag-Cu) membranes (M_1 and M_2) were formed by two different ways:

(I) Initial plating of Pd-Ag alloy and then deposition of Cu over the alloy membrane and annealing in hydrogen atmosphere (M_1)

(II) Deposition of three individual metals sequentially (Pd, Ag then Cu) and annealing in hydrogen atmosphere (M_2)

XRD pattern of the plated membrane-M_1 under different plating and annealing conditions is shown in Figure 3.12. The XRD pattern of as prepared membrane reveals individual peaks due to Pd, Ag and Pd-Ag alloy after annealing in hydrogen atmosphere. The XRD pattern of the disc after copper deposition on the Pd-Ag alloy shows distinct peaks due to Cu and Pd-Ag alloy. After 30 hours of annealing in hydrogen atmosphere at 873 K it is observed that the peak corresponding to Pd-Ag alloy has been shifted to higher angle indicating formation of a ternary Pd-Ag-Cu alloy. However, another set of lines are also observed for a binary silver rich Pd alloy phase. This may be due the solubility limit of silver in the ternary alloy phase. The XRD pattern of the deposited membrane-M_2 is shown in Figure 3.13.

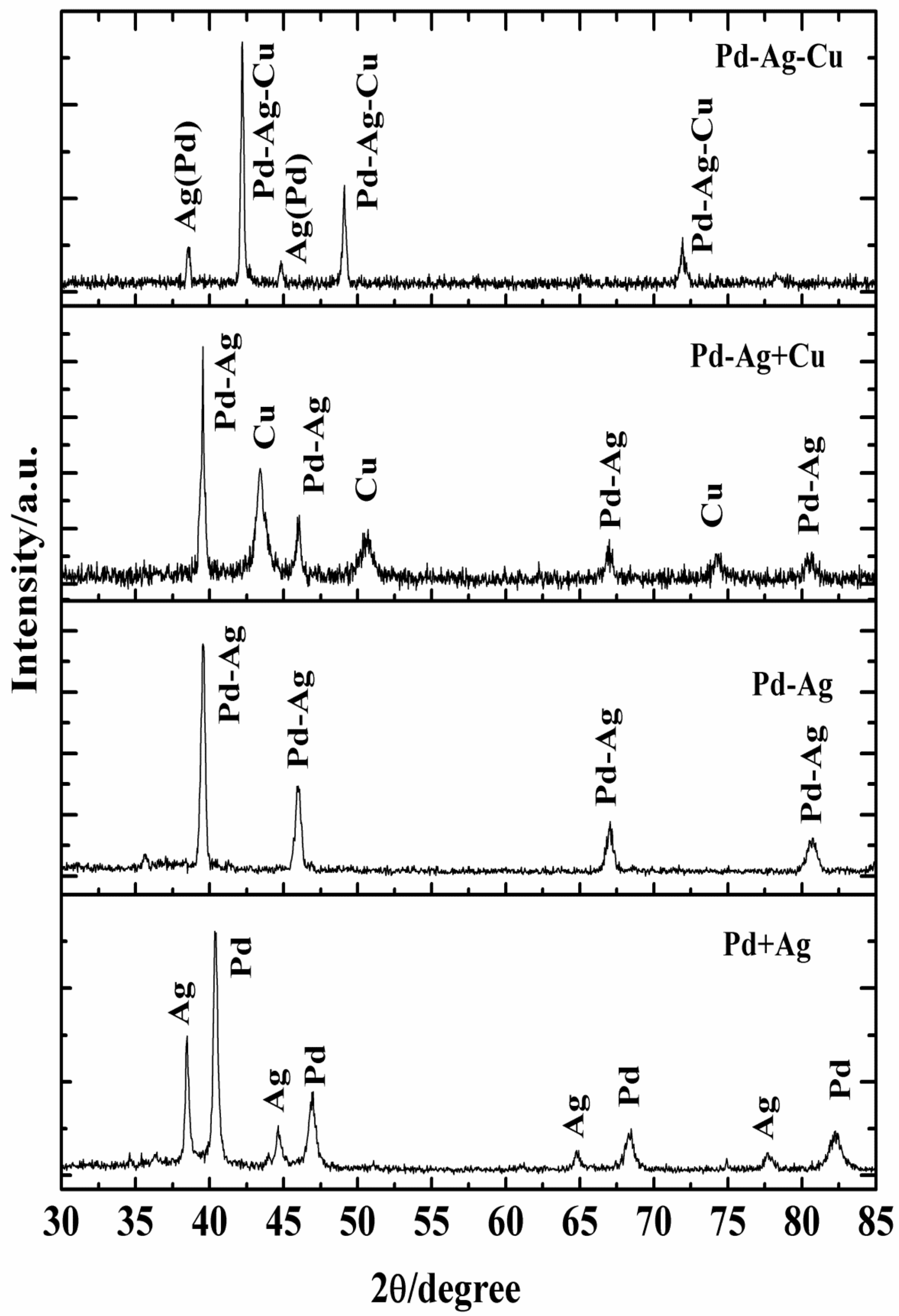

Figure 3.12. XRD patterns of Pd-Ag-Cu membrane M_1

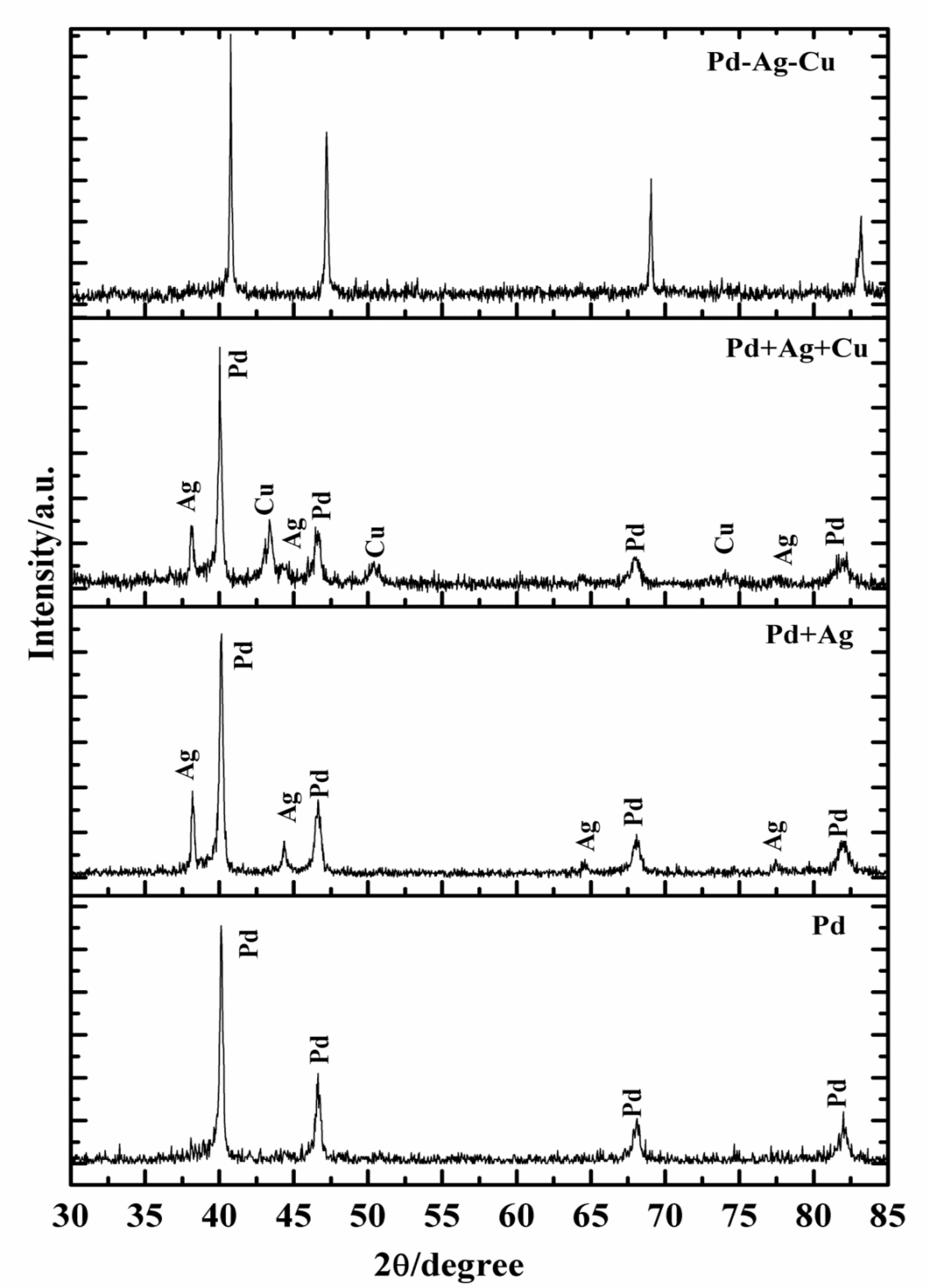

Figure 3.13. XRD patterns of Pd-Ag-Cu membrane M_2

The XRD pattern of the as prepared membrane clearly indicates peaks due to all three metals Pd, Ag and Cu. After annealing in hydrogen atmosphere for 30 hours, the peaks corresponding to the individual metals Pd, Ag and Cu have vanished and merged to form a single phase. The reflection lines of the formed alloy matches with that of Pd with a systematic shift towards higher angle. This indicates the formation of a ternary alloy having f.c.c crystal structure with a lower lattice constant compared to Pd. Study by Tarditi et al. [144] also indicates the effectiveness of alloying in hydrogen atmosphere for the formation of ternary alloy membrane. They have found formation of binary phase of Pd-Ag and Pd-Cu phase at initial stages of annealing. However, prolonged heating under hydrogen atmosphere at 773 K the fraction of the Pd-Ag phase increases to form a ternary alloy. Therefore, heating under hydrogen atmosphere enhances the thermal diffusion of atoms in the crystal lattice resulting in alloy formation. The annealing under hydrogen atmosphere was found to be effective and less time consuming process, whereas the annealing in inert atmosphere is an energy consuming process. It has been also reported that annealing for longer duration at higher temperature (> 873 K) may cause diffusion of SS through the metallic membrane, causing a permeation loss [145].

The lattice constant of the deposited Pd-Ag and Pd-Ag-Cu alloy membranes is calculated by indexing the reflection lines. The value of lattice constant of Pd-Ag was found to be 0.3957±0.0001 nm and that of Pd-Ag-Cu was found to be 0.38817±0.0001 nm.

3.2.3. Characterization of the surface topography by SEM

SEM images were taken after plating experiments to study the morphology of the membranes. The SEM images of bare PSS and after single Pd deposition on the PSS substrate is shown in Figure 3.14(a) & (b).

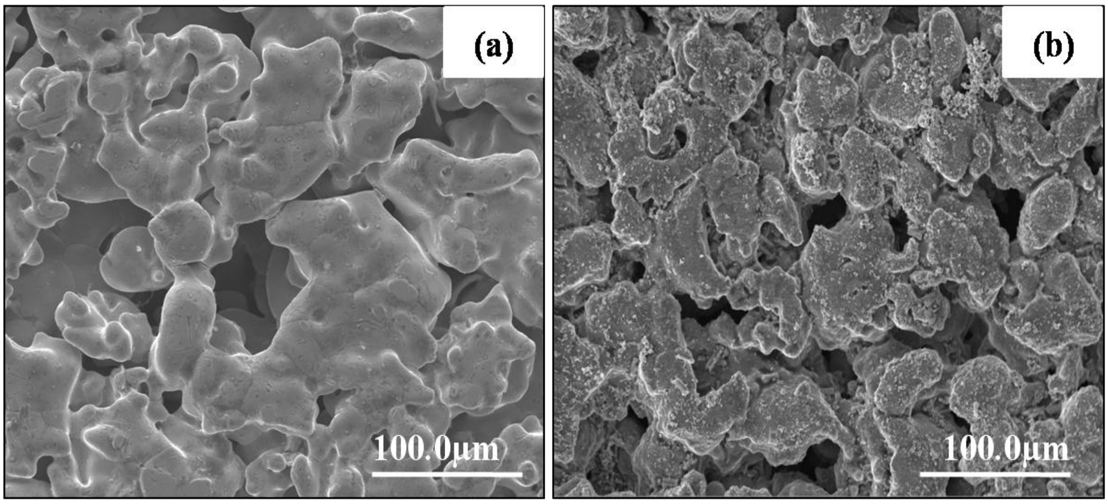

Figure 3.14. SEM image of (a) bare PSS, (b) after Pd deposition

The SEM image of bare SS surface (Figure 3.14(a)) depicts large number of open pores on the substrate. But the image of the membrane after Pd deposition (Figure 3.14(b)) clearly shows that the pores in PSS substrate have been covered by Pd however the membrane is not defect free. Repeated plating experiment and annealing reduces the number of pores substantially as is evident from the SEM image shown in Figure 3.15. It is observed from the figure that most of the pores have been blocked by Pd particles, which will improve the membrane selectivity.

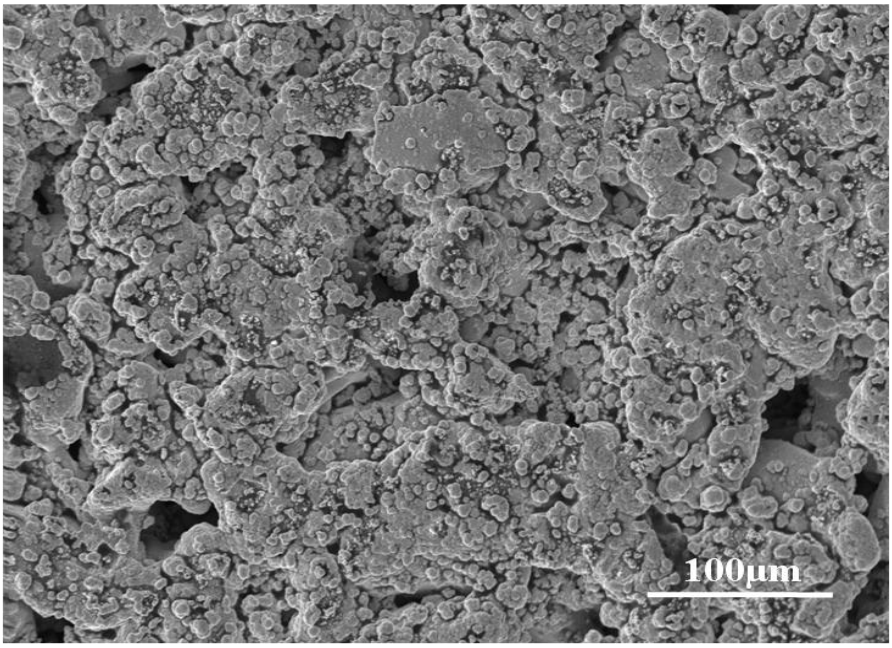

Figure 3.15. SEM image of Pd membrane after subsequent plating and annealing experiments

SEM image of sequentially deposited and co-deposited Pd-Ag alloy membrane is shown in Figure 3.16. It is evident from the figure that co-deposition results in dendrite growth of the membrane causing a poor filling of the pores. The growth of the grains in axial direction results in dendrite formation. This happens due to the large difference in the electrode potential of Pd and Ag deposition. The difference in reduction potential results in preferential deposition of Ag compared to Pd. The faster kinetics of Ag deposition over Pd results in a dendrite growth. However, the SEM image of the Pd-Ag membrane after sequential deposition and annealing under hydrogen cover shows that the pores are covered and a relatively defect free membrane is formed. Similarly the SEM image of the Pd-Ag-Cu plated membrane (M_2) is shown in Figure 3.17. It can be observed that the membrane produced after eletroless deposition of metals on PSS substrate is dense with minimum defects.

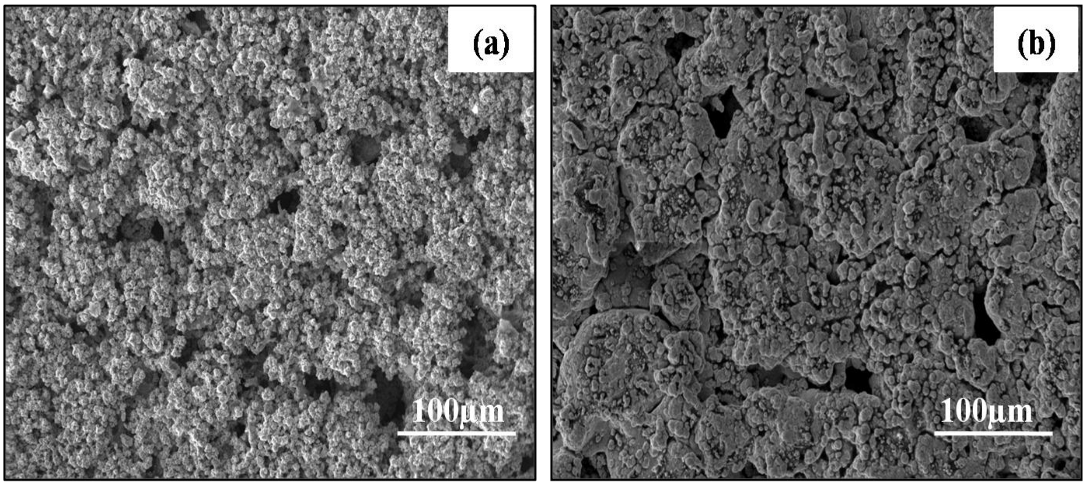

Figure 3.16. SEM image of (a) co-deposited Pd-Ag alloy, (b) Sequentially deposited Pd-Ag alloy

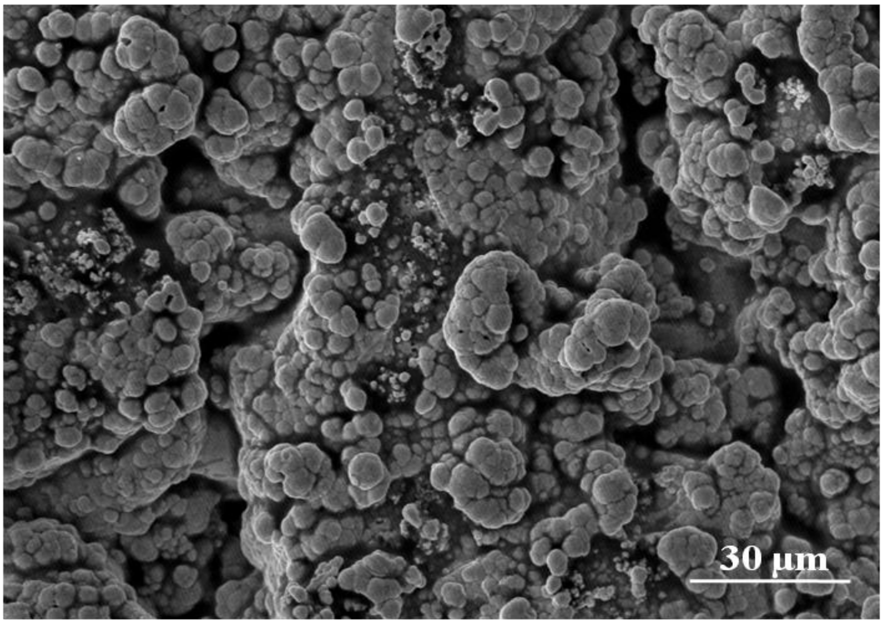

Figure 3.17. SEM image of Pd-Ag-Cu alloy membrane (M_2) after annealing

It is evident from the SEM image of the deposited metal/alloy that the formed membrane has high surface roughness. The high surface roughness of the films is one advantage of this method of preparation, as it provides increased surface area on which the hydrogen dissociation reaction may take place. Since the kinetics of the metal deposition decides the morphology of membrane, it is strongly dependent on the temperature and bath composition. Therefore a constant pH and temperature was maintained throughout the experiment.

3.2.4. Compositional analysis of the deposited membrane by EDS analysis

The EDS spectra of the deposited membranes after plating and annealing were taken at different morphological positions to verify their chemical compositions. The EDS spectrum of the deposited and annealed Pd membrane is shown in Figure 3.18, which clearly shows the characteristic peaks of Pd atom only, indicating a pure Pd membrane deposition.

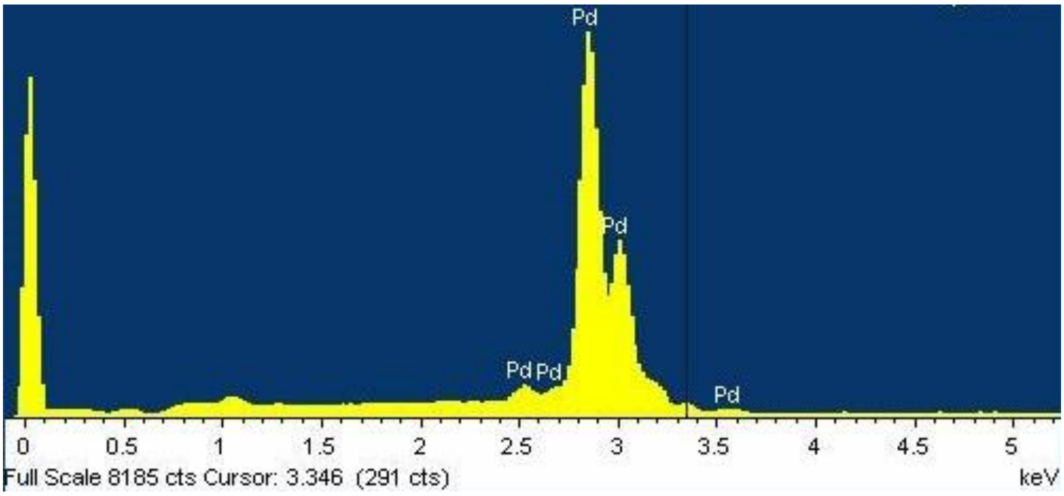

Figure 3.18. EDS image of Pd membrane after subsequent plating and annealing

The EDS spectra of the Pd-Ag alloy membrane annealed under hydrogen atmosphere is shown in the Figure 3.19. The spectrum indicates the characteristic peaks due to Pd and Ag. The EDS analysis carried out at different morphological positions reveal an average chemical composition of the alloy to be $Pd_{0.65}Ag_{0.35}$.

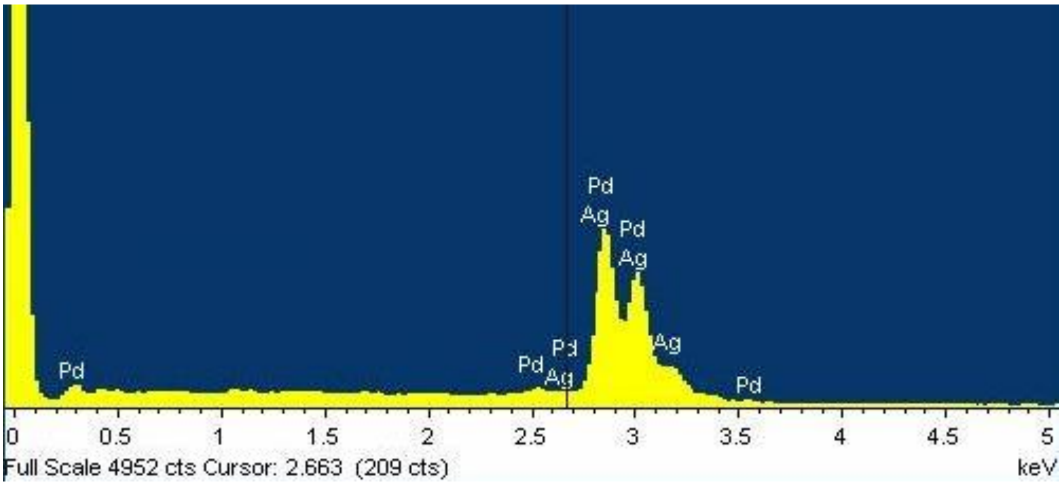

Figure 3.19. EDS image of the deposited Pd-Ag alloy membrane

The EDS spectrum of the deposited and annealed ternary alloy membrane (M2) is shown in Figure 3.20.

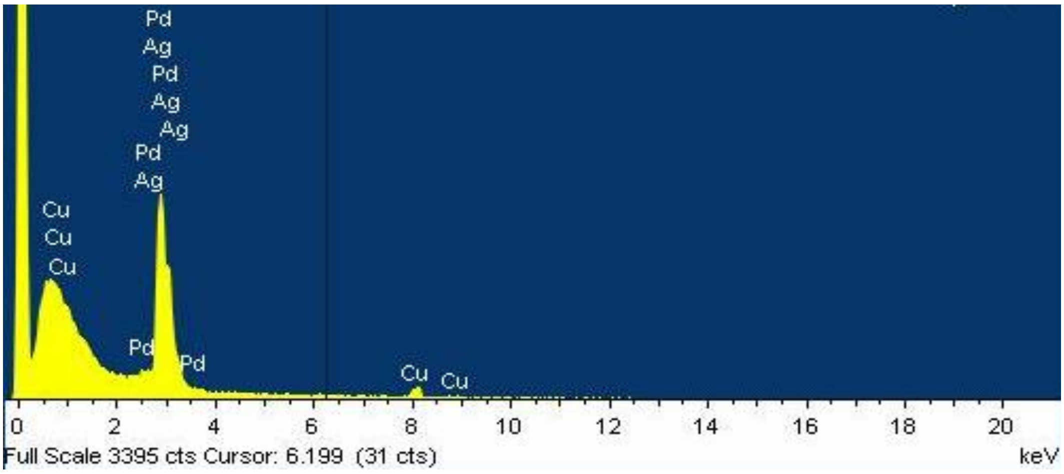

Figure 3.20. EDS image of Pd-Ag-Cu plated membrane (M_2)

The EDS analysis reveals the average composition of the alloy to be $Pd_{0.74}Ag_{0.14}Cu_{0.12}$. The thickness of the deposited membrane was determined from the weight gain calculations. If ΔW is the net weight gain after metal/alloy deposition on a substrate surface having area = 'A', and 'd' be the density of the metal/alloy deposited then the thickness of the membrane 'l' can be expressed as:

$$L = \Delta W/(A \text{ x } d) \qquad (3\text{-}12)$$

Using the above expression, the thickness of Pd, $Pd_{0.65}Ag_{0.35}$ and $Pd_{0.74}Ag_{0.14}Cu_{0.12}$ were found to be 30, 36, and 32 µm, respectively.

Electroless plating method is an efficient and cost effective way for production of very thin metal/alloy membranes. However, the present investigation and the literature information data [86, 95, 111, 144, 145] suggest that the membranes prepared by this method have finite defects due to presence of very small pinholes. Hence, in the hydrogen permeation experiments, the electroless plated membranes show finite hydrogen selectivity in the range of 500 to 1000 with respect to nitrogen. Membranes having infinite selectivity are difficult to prepare by electroless plating method. The outcome of the present investigation suggest that cost effective membranes can be prepared by electoless plating method with minimum pinhole defects which can be used for purification of industrially produced hydrogen, where infinite hydrogen selectivity is not an important criteria. However, these membranes cannot be used for fusion fuel cycle applications, where hydrogen isotopes such as tritium need to be purified from helium. For this particular application, infinite hydrogen selectivity is a prime requirement. It has been reported that membranes prepared by metallurgical route have infinite hydrogen selectivity [95, 111]. Hence, in the present investigation, hydrogen/deuterium permeation experiments were carried out using the membranes prepared by metallurgical route.

3.3. Hydrogen/deuterium permeation through membranes prepared by metallurgical route

In the present study, Q_2 (Q = H, D) permeation experiments were carried out using 100µm thin $Pd_{0.77}Ag_{0.23}$ and $Pd_{0.77}Ag_{0.10}Cu_{0.13}$ alloy foils prepared by arc melting and cold rolling technique. In the initial experiments, two different feed gas compositions (H_2 : He = 90 : 10 and 5 : 95) were chosen to examine the effectiveness of the membrane for separating hydrogen from helium in the entire range of compositions. The composition of the feed and permeate gases were analyzed by the residual gas analyzer (RGA) from time to time during the permeation experiments throughout the entire temperature range of investigation. The result of feed and permeate gas analysis at a particular instant of time using $Pd_{0.77}Ag_{0.10}Cu_{0.13}$ membrane and two different gas mixtures at 573 K are shown in Figure 3.21 and 3.22. It is evident from the figures that the peak due to helium at m/z = 4 is absent in the permeate gas. Similar behavior is observed for the $Pd_{0.77}Ag_{0.23}$ membrane. Hence, it is inferred that both the Pd-alloy membranes have infinite selectivity for hydrogen isotopes. From the gas analysis results it clear that the membrane can be applied to purify hydrogen from wide range of helium containing mixture.

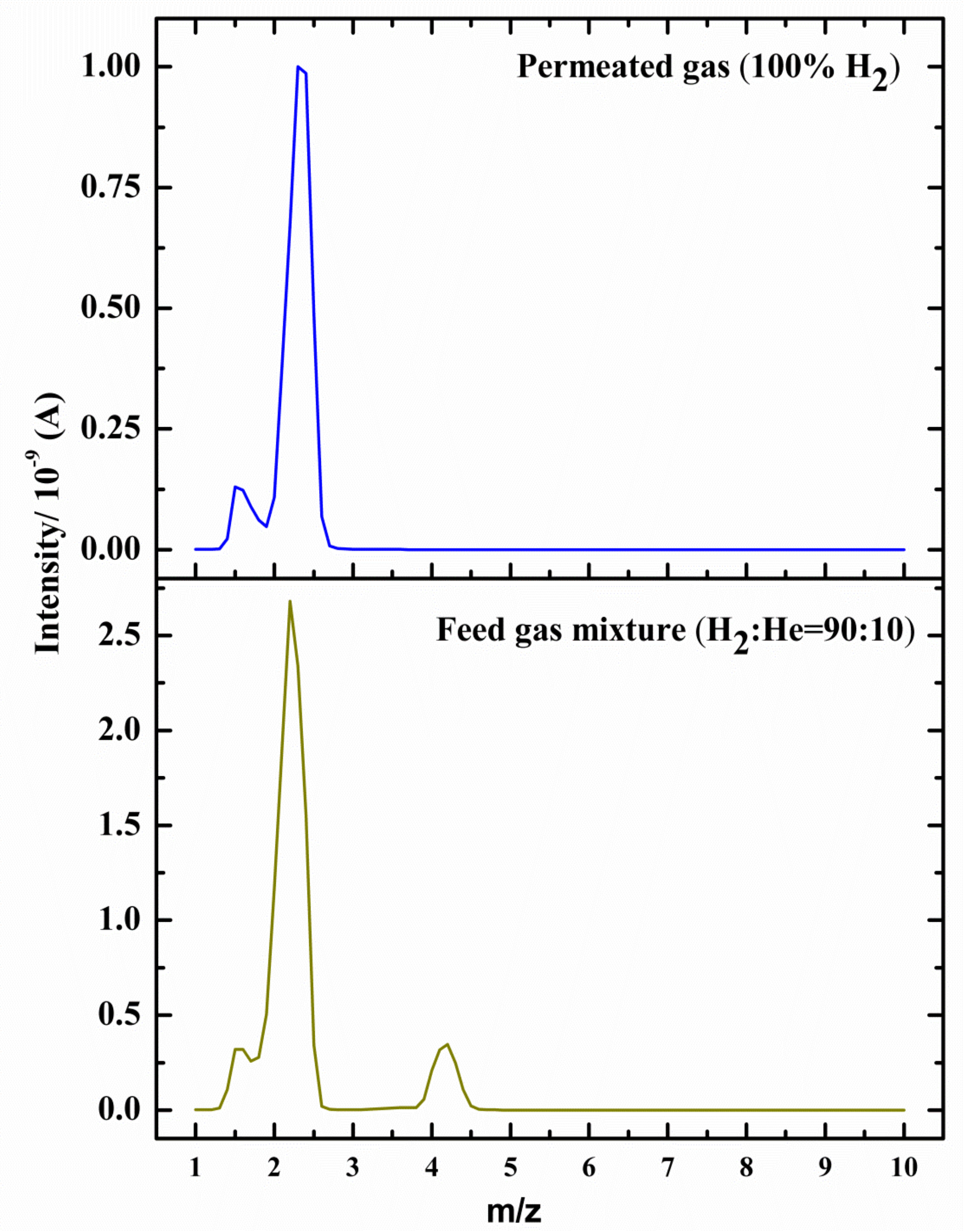

Figure 3.21. Analysis results of feed (H_2: He = 90 : 10) and permeated gas using RGA

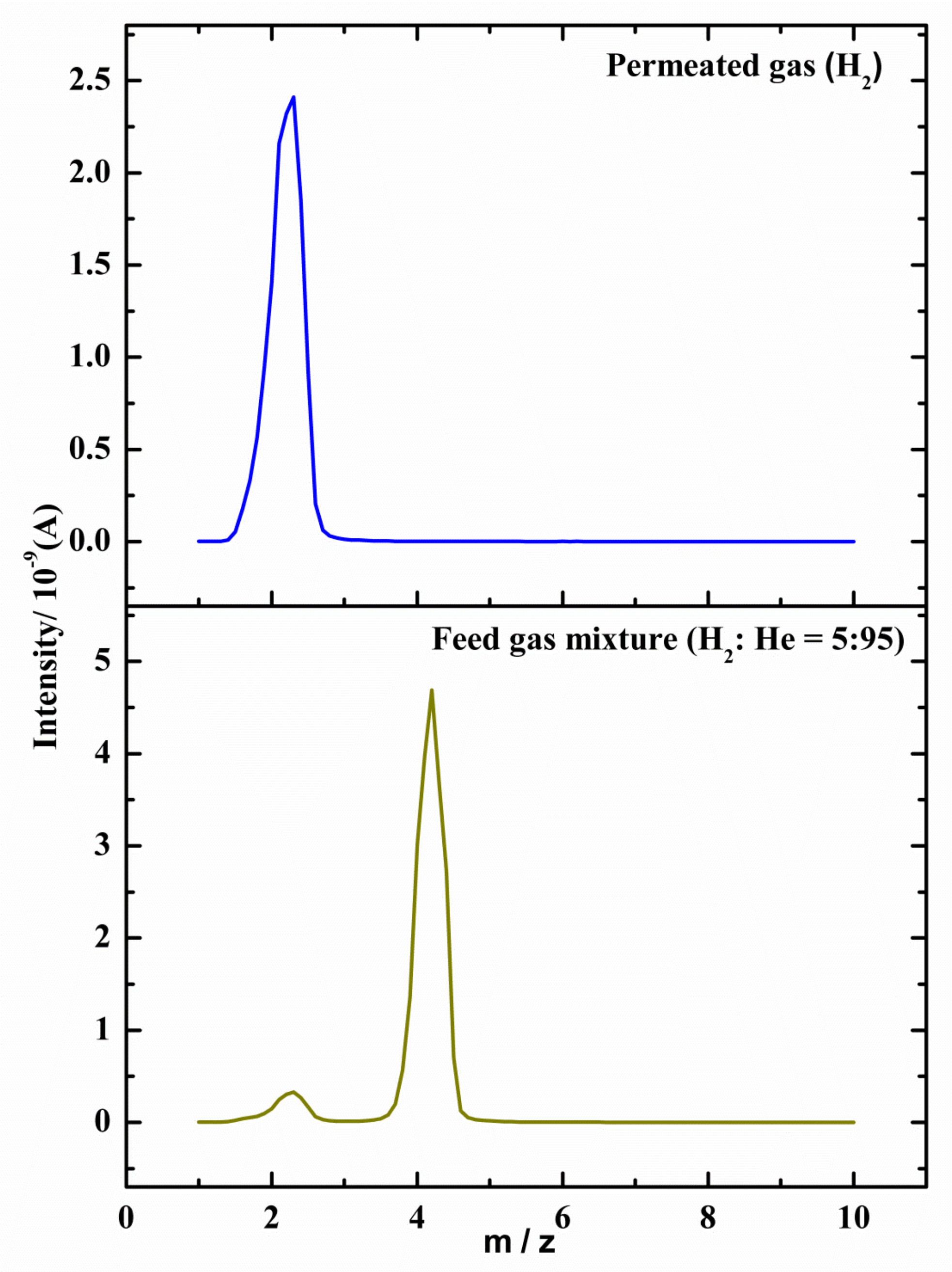

Figure 3.22. Analysis results of feed gas (He : H_2 = 5 : 95) and permeated gas using RGA

As discussed in the previous section-1.5.3, the mechanism of permeation of Q_2 through Pd/Pd-alloy membranes is a multi-step process referred to as "solution-diffusion" mechanism, as it proceeds through formation of a Pd-H_x solution [66]. The expression for Q_2 flux through the metallic membranes is given by:

$$J = P_e(p_f^n - p_d^n) / L \qquad (3\text{-}13)$$

where, J is the flux (mol $m^{-2}s^{-1}$), P_e is the permeability (mol $m^{-1}s^{-1}Pa^{-0.5}$), L is the thickness of membrane (m), 'n' is the pressure exponent and p_f and p_d are the Q_2 partial pressures (Pa) at the feed and permeate sides of membrane, respectively.

The value of n depends on the rate-limiting steps in the permeation process. When the rate limiting step is the bulk diffusion through the membrane, the value of n becomes close to 0.5 because the diffusion rate is proportional to the concentration of hydrogen atoms on opposite sides of the metal surface which in turn proportional to the square root of hydrogen pressure [90]. Several factors may contribute towards deviation of the pressure exponent (n) from the ideal behavior (n = 0.5). Guazzone et al [146] described the contribution of different flow mechanism through the defects in the membrane on the pressure exponent value and concluded that the value of n is greater than 0.5 when the membrane is not free of defects. In case of thickness of membrane > 5 µm, the exponent value greater than 0.5 is attributed to defects and pin holes in the membrane which contributes substantially to permeation. This happens through the Knudsen flow and viscous flow and results in increase of flux which gives rise to a higher value of pressure exponent. In addition to the above external mass transfer effect, Caravella et al. [91] have explained that the non-ideal behavior of hydrogen in metal-hydrogen system at low temperature and high pressure contributes significantly towards the deviation of pressure exponent (n) from the ideal value of 0.5. However, as seen in the analyses of Caravella et al. [91], the value of n is very close to the ideal value in the temperature and pressure ranges covered in the present study. Hence, for membranes of thickness ~100 μm and free of any mechanical defect, at moderate temperature and pressure Eq.3.13 can be written as:

$$J = P_e(p_\mathrm{f}^{0.5} - p_\mathrm{d}^{0.5}) / L \qquad (3\text{-}14)$$

In this study, we have kept the permeate side under vacuum i.e. p_d is zero and hence the permeability can be expressed as:

$$J = P_e(p_\mathrm{f}^{0.5}) / L \qquad (3\text{-}15)$$

The Q_2 permeation experiments through $Pd_{0.77}Ag_{0.23}$ and $Pd_{0.77}Ag_{0.10}Cu_{0.13}$ alloy membranes were carried out in the temperature range of 523-673 K with a gap of 50 K and at different trans-membrane Q_2 pressures of 50, 100 and 150 kPa. The Q_2 flux was calculated by metering the amount of Q_2 permeated through the membrane using a mass flow controller, in fully open mass flow meter (MFM) mode, in the permeate side. The measured flux of Q_2 at different temperatures as a function of square root of Q_2 partial pressure for $Pd_{0.77}Ag_{0.23}$ and $Pd_{0.77}Ag_{0.10}Cu_{0.13}$ alloy membranes are shown in Figure 3.23 and Figure 3.24, respectively. It is evident from these figures that both the alloy membranes show a linear relation between the flux with square root of partial pressure ($p^{0.5}$) of Q_2. The results are well in agreement with Sieverts' law suggesting the diffusion of hydrogen through the bulk Pd-alloy membrane as the rate limiting step. The general trend which emerges from the result is that the Q_2 flux increases with increase in Q_2 partial pressure in the feed side and the increase in experimental temperature.

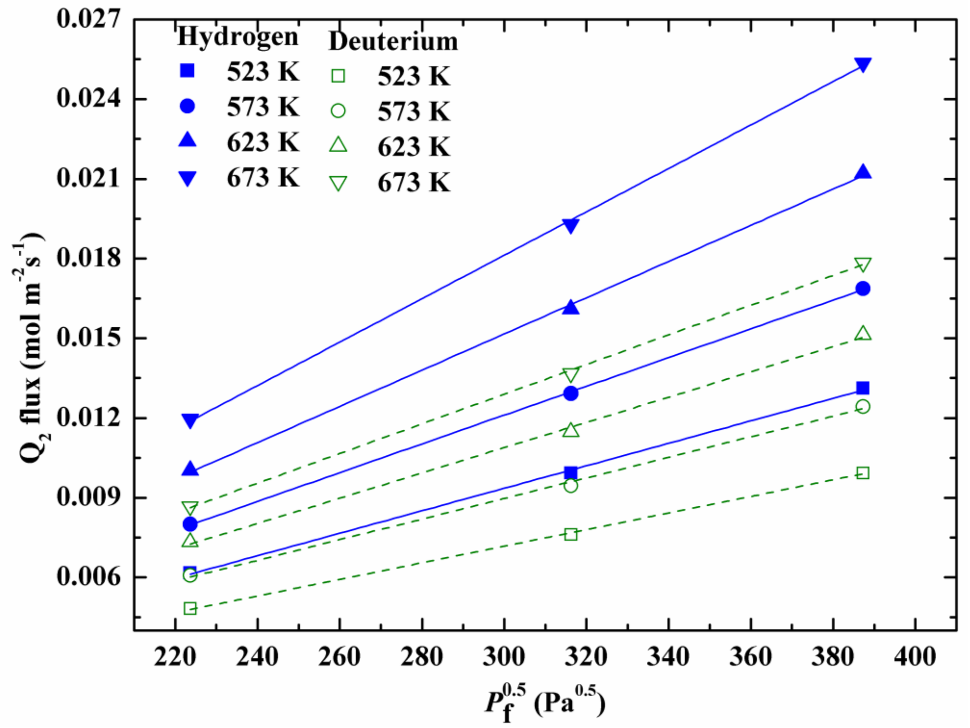

Figure 3.23. Variation of flux with trans-membrane pressure for $Pd_{0.77}Ag_{0.23}$ alloy

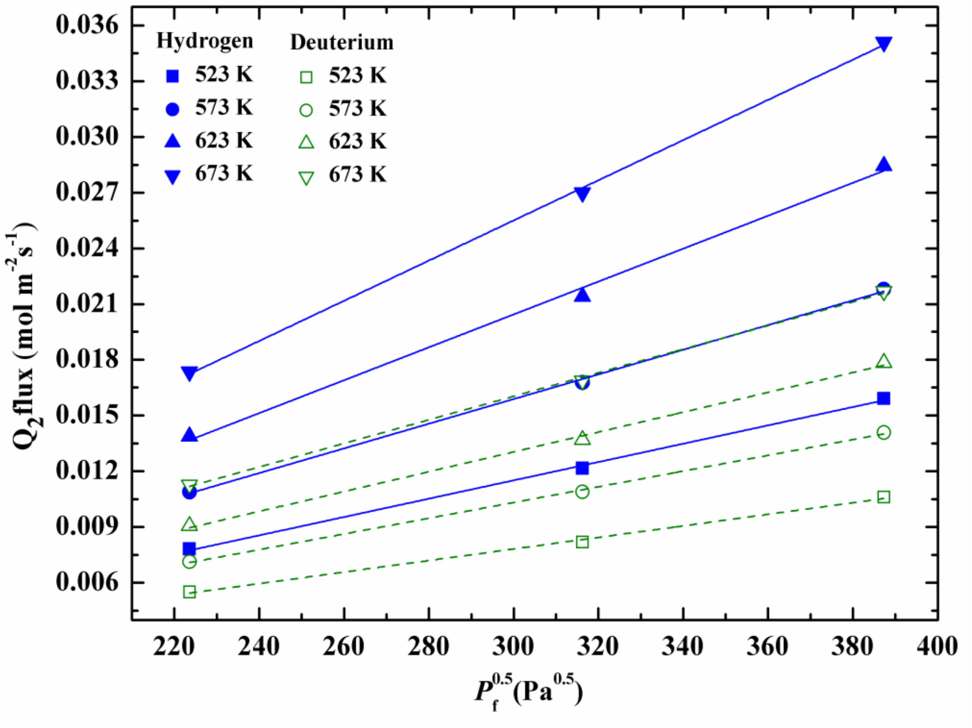

Figure 3.24. Variation of flux with trans-membrane pressure for

$Pd_{0.77}Ag_{0.10}Cu_{0.13}$ alloy

It can be seen from both the figures that the rate of D_2 permeation is lower than that of H_2 for both $Pd_{0.77}Ag_{0.23}$ and $Pd_{0.77}Ag_{0.10}Cu_{0.13}$ alloy membranes showing significant hydrogen isotope effect on permeation behavior. On this basis, it is expected that the rate of tritium permeation will still be lower than that of deuterium.

Since, the membrane has infinite hydrogen selectivity, it is expected that the flux should only depend upon the trans-membrane H_2 pressure and not on the total feed gas pressure. In order to validate this assumption, permeation experiments were carried out with $Pd_{0.77}Ag_{0.23}$ alloy membrane maintaining same trans-membrane H_2 pressure but varying total feed gas (H_2 + He) pressure. The results of these experiments are shown in Figure 3.25.

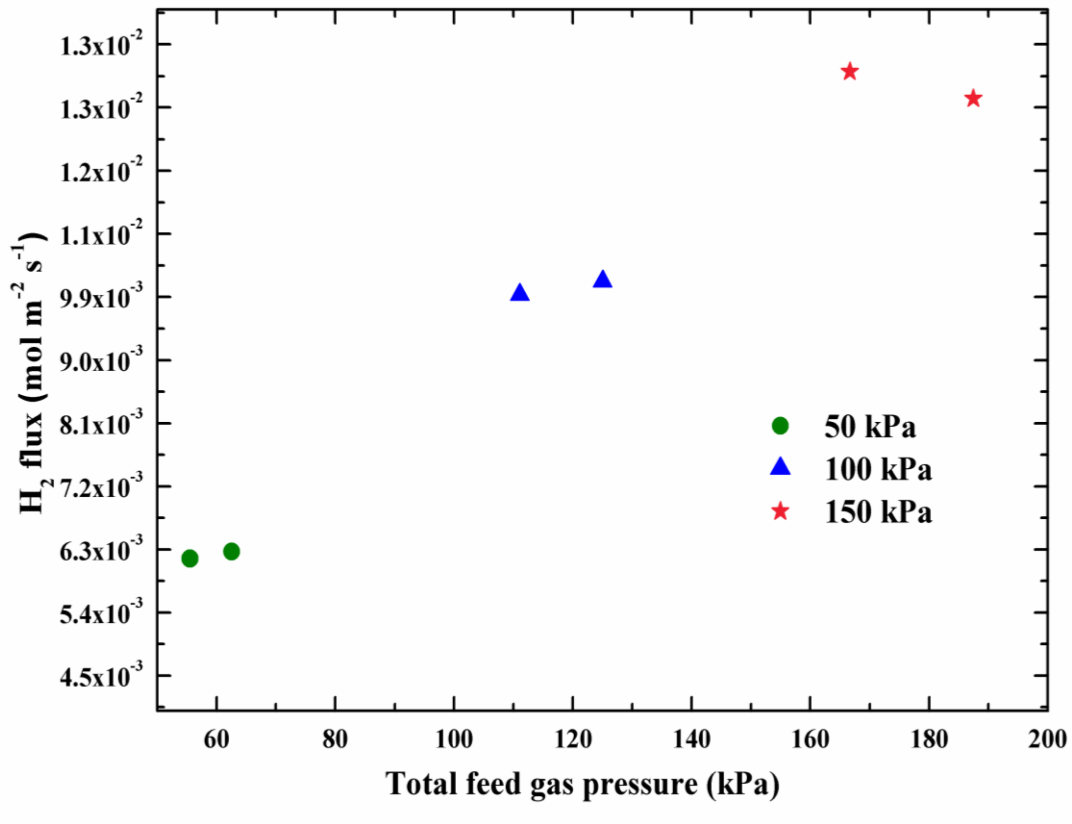

Figure 3.25. Variation of H_2 flux as a function total feed gas pressures at different trans-membrane H_2 pressures for $Pd_{0.77}Ag_{0.23}$ alloy membrane

It is evident from the figure the H_2 flux is only dependent on the trans-membrane H_2 pressure and not on the total feed gas pressure.

The permeability of Q_2 was calculated using equation 3.15. The plot of logarithm of permeability (ln P_e) versus reciprocal temperature ($1/T$) is shown in Figure 3.26 and Figure 3.27 for $Pd_{0.77}Ag_{0.23}$ and $Pd_{0.77}Ag_{0.10}Cu_{0.13}$ alloys, respectively.

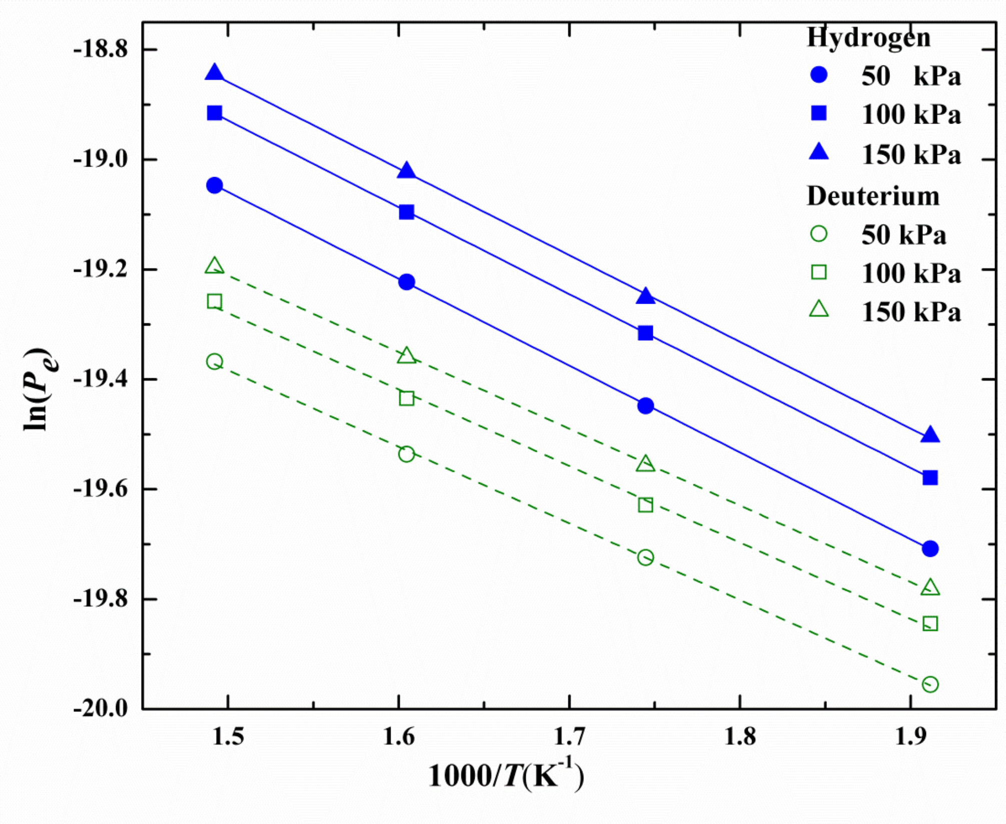

Figure 3.26. Variation of permeability with temperature for $Pd_{0.77}Ag_{0.23}$ alloy

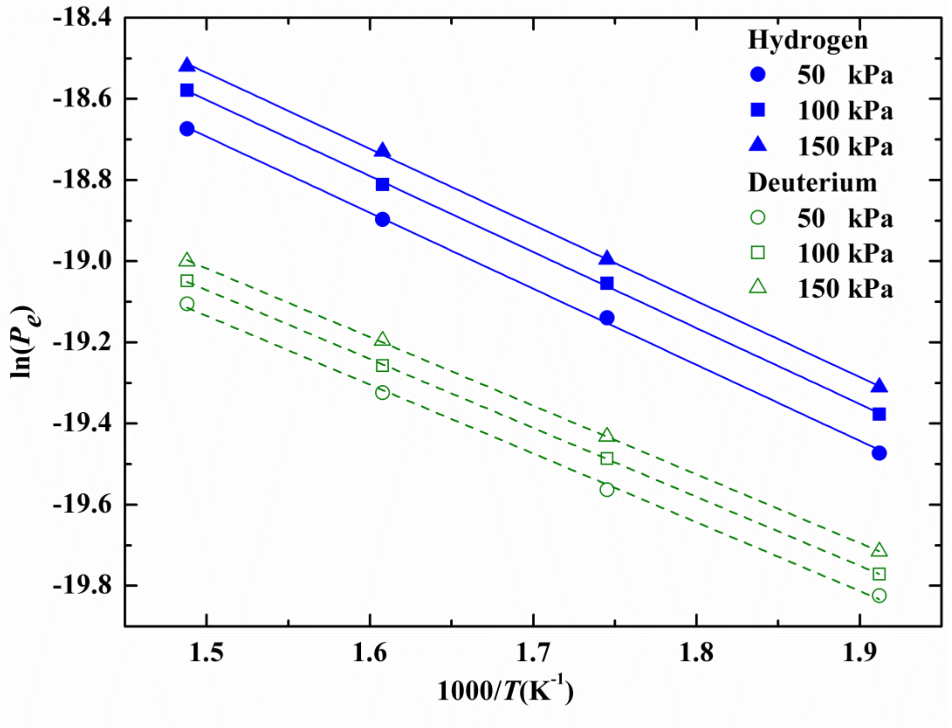

Figure 3.27. Variation of permeability with temperature for $Pd_{0.77}Ag_{0.10}Cu_{0.13}$ alloy

The linear dependence observed in both the figures shows Arrhenius behaviour as per the equation:

$P_e = P_o \exp(-E_a/RT)$ (3-16)

where, P_e is permeability (mol $m^{-1}s^{-1}Pa^{-0.5}$), P_o is the pre-exponential factor (mol m^{-1} $s^{-1}Pa^{-0.5}$), E_a is the activation energy (kJ mol^{-1}), R is the gas constant (8.314 J mol^{-1} K^{-1}) and T is the absolute temperature (K). The values of P_o and E_a obtained in this study are listed in Table 3-5. It is observed from the table that the value of P_o for a given alloy-Q_2 system shows a systematic but marginal variation with pressure. Similar type of dependence of P_o on the pressure is also reported in the literature [147]. This variation of P_o is expected because permeation of Q_2 in alloy is a gas-solid interaction phenomenon and hence will depend on the nature of the gas as well as pressure of the gas besides several intrinsic factors. Table 3-5 also indicates that the $P_o(H_2) > P_o(D_2)$ for both the alloys which is consistent with collision theory where the collision frequency is inversely proportional to the square root of reduced mass. A comparison of permeability of Q_2 in $Pd_{0.77}Ag_{0.23}$ and $Pd_{0.77}Ag_{0.10}Cu_{0.13}$ alloy membranes at 100 kPa trans-membrane pressure is shown in Figure 3.28. It is observed that permeability of H_2 is higher than that of D_2 for both the alloys at all experimental temperatures. However, the permeability of Q_2 is found to be higher for the ternary alloy $Pd_{0.77}Ag_{0.10}Cu_{0.13}$ than that of binary alloy $Pd_{0.77}Ag_{0.23}$ at all experimental temperatures and trans-membrane Q_2 pressures. These results show the favourable effect of replacement of silver with copper on permeability of hydrogen isotopes. It is apparent from Figure 3.28 that the slopes are nearly same at all trans-membrane Q_2 pressures indicating same activation energies. The average values of apparent activation energies for hydrogen and deuterium permeation in $Pd_{0.77}Ag_{0.23}$ alloy was found to be 13.1 ± 0.1 and 11.5 ± 0.1 kJ mol^{-1}, respectively, whereas for $Pd_{0.77}Ag_{0.10}Cu_{0.13}$ alloy was found to be 15.6 ± 0.1 and 14.1 ± 0.1 kJ mol^{-1}, respectively. The higher activation energies for hydrogen compared to deuterium can be qualitatively explained on the basis of transition state theory of diffusion as reported by Sicking [92].

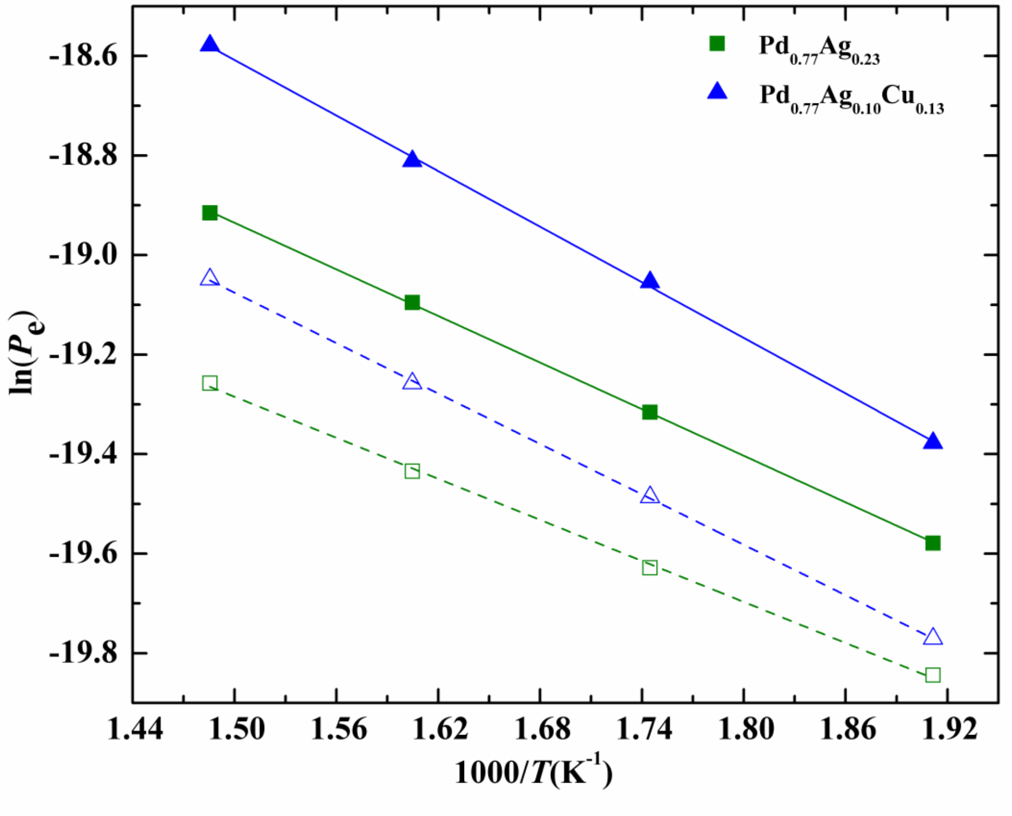

Figure 3.28. Comparison of permeability of Q_2 at 100 kPa for two alloys $Pd_{0.77}Ag_{0.23}$ and $Pd_{0.77}Ag_{0.10}Cu_{0.13}$ (Solid symbols: H_2; hollow symbol: D_2)

Since both $Pd_{0.77}Ag_{0.23}$ and $Pd_{0.77}Ag_{0.10}Cu_{0.13}$ alloys have f.c.c crystal structure, the hydrogen isotopes preferably resides in the octahedral interstitial positions. Hence, the bulk diffusion of Q in these alloys is mainly due to octahedral to octahedral jump. As reported by Sicking [92], the energies of the ground state and the transition state for octahedral to octahedral jump are dependent on the isotopic mass. The energy difference of these two states decreases with increase in isotopic mass which results in higher activation energy of diffusion of H as compared to D as shown in Figure 1.9.

The H_2/D_2 flux ratio, $J_{(H2)}/J_{(D2)}$, varies from 1.30 to 1.41 and 1.48 to 1.60 for $Pd_{0.77}Ag_{0.23}$ and $Pd_{0.77}Ag_{0.10}Cu_{0.13}$ alloys respectively, as the temperature increases from 523 to 673 K. This value is very close to the classical theoretical value of diffusion constant ratio $(m_D/m_H)^{1/2}$ [148] and is consistent with the theoretical expectation for kinetic isotope effect as reported by Sicking [92].

A comparison with literature reported data [148-158] is made for various Pd/Pd-alloy-Q_2 systems in Table 3-5. It is evident from Table 3-5 that the hydrogen permeation results for $Pd_{0.77}Ag_{0.23}$ are in good agreement with values reported in literature. However, the higher permeability of Q_2 in $Pd_{0.77}Ag_{0.10}Cu_{0.13}$ alloy compared to $Pd_{0.77}Ag_{0.23}$ alloy is surprisingly deviating from the earlier experimental and computational studies [156, 158, 159]. Since most of these studies use composite thin membranes having finite hydrogen selectivity, it is not possible to have a direct correlation with the results of present study where thick alloy membranes having infinity hydrogen selectivity are used. The reasonably higher permeability of $Pd_{0.77}Ag_{0.10}Cu_{0.13}$ alloy suggests its potential application in membrane diffuser for purification of hydrogen isotopes in fusion fuel clean-up system.

Table 3-5. Hydrogen permeation characteristic of Pd-alloy membranes

Membrane permeation system	L (μm)	ΔP (kPa)	T (K)	P_o (mol $m^{-1}s^{-1}Pa^{-0.5}$)	E_a (kJ mol^{-1})	P_e at 673 K (mol $m^{-1}s^{-1}Pa^{-0.5}$)	Ref.
Pd-H_2	100	2600	623-1173	1.01×10^{-7}	13.0	9.9×10^{-9}	[149]
Pd-H_2	1000	100-2700	623-1173	1.75×10^{-7}	13.8	1.5×10^{-8}	[150]
$Pd_{0.77}Ag_{0.23}$-H_2	61	100-200	423-673	6.64×10^{-8}	11.24	8.9×10^{-9}	[151]
$Pd_{0.77}Ag_{0.23}$-H_2	100	100	373-523	4.87×10^{-7}	15.23	3.2×10^{-8}	[152]
$Pd_{0.75}Ag_{0.25}$-H_2	198	1-100	323-773	5.58×10^{-8}	6.304	1.8×10^{-8}	[153]
$Pd_{0.75}Ag_{0.25}$-D_2	198	1-100	323-773	3.43×10^{-8}	6.156	1.14×10^{-8}	[148]
$Pd_{0.75}Ag_{0.25}$-H_2	50	100-250	473-573	5.4×10^{-8}	10.7	8×10^{-9}	[153]
$Pd_{0.77}Ag_{0.23}$-H_2	50	220	573-673	5.38×10^{-7}	33.3	1.4×10^{-9}	[154]
Pd-Ag(Ag-23-25at%)-H_2	42	141-243	-	-	-	${}^{a}1.8 \times 10^{-9}$	[155]
$Pd_{0.77}Ag_{0.23}$-H_2	**100**	**50**	**523-673**	**5.65×10^{-8}**	**13.1±0.1**	**5.4×10^{-9}**	**This Study**
		100		**6.44×10^{-8}**	**13.1±0.1**	**6.2×10^{-9}**	
		150		**6.87×10^{-8}**	**13.1±0.1**	**6.6×10^{-9}**	

$Pd_{0.77}Ag_{0.23}$-D_2	**100**	**50**		**3.09 x 10^{-8}**	**11.5±0.1**	**4.0x10^{-9}**	**This**
		100	**523-673**	**3.42 x 10^{-8}**	**11.5±0.1**	**4.4x10^{-9}**	**Study**
		150		**3.67 x 10^{-8}**	**11.6±0.1**	**4.7x10^{-9}**	
*$Pd_{0.79}Cu_{0.11}Ag_{0.10}$-$H_2$	4.6	100	673	1.15x 10^{-7}	12.5	1.23x10^{-8}	[156]
*$Pd_{0.68}Ag_{0.7}Cu_{0.25}$-$H_2$	24	10-100	623-723	-	-	^{b}5.4x10^{-9}	[157]
$Pd_{0.77}Ag_{0.10}Cu_{0.13}$-$H_2$	-	-	600	-	-	^{c}3.0x10^{-9}	[158]
$Pd_{0.77}Ag_{0.10}Cu_{0.13}$-$H_2$	**100**	**50**		**1.26 x 10^{-7}**	**15.6±0.1**	**7.8x10^{-9}**	**This**
		100	**523-673**	**1.38 x 10^{-7}**	**15.6±0.1**	**8.5x10^{-9}**	**Study**
		150		**1.48 x 10^{-7}**	**15.6±0.1**	**9.1x10^{-9}**	
$Pd_{0.77}Ag_{0.10}Cu_{0.13}$-$D_2$	**100**	**50**	**523-673**	**6.23 x 10^{-8}**	**14.0±0.1**	**5x10^{-9}**	**This**
		100		**6.67 x10^{-8}**	**14.1±0.1**	**5.3x10^{-9}**	**Study**
		150		**6.96 x 10^{-8}**	**14.0±0.1**	**5.6x10^{-9}**	

* Composite membranes; ^{a}at 648 K; ^{b}at 723 K; ^{c}calculated from contour map of permeability

3.2.2. Separation of helium from traces of hydrogen impurity using the ternary $Pd_{0.77}Ag_{0.10}Cu_{0.13}$ alloy membrane

Since $Pd_{0.77}Ag_{0.10}Cu_{0.13}$ alloy membrane has given infinite selectivity for hydrogen isotopes with appreciable flux at moderate temperature and low trans-membrane pressure, its applicability for separation and purification of ^3He from tritium streams is explored in this study. In a tritium storage bed, ^3He is formed due to radioactive decay of tritium. Being an inert gas, ^3He gets released from the entrapped tritium bed and develops pressure in the storage vessel. This ^3He can be removed and used for neutron detectors. However, the ^3He recovered in this manner contains tritium at low concentration which can be purified by passing through the Pd-based alloy diffuser. In this context, we have investigated the feasibility of removing about 1% tritium from ^3He using a synthetic mixture of ^4He + 1% H_2. The synthetic gas mixture was taken in a 1 litre volume and allowed to permeate through $Pd_{0.77}Ag_{0.10}Cu_{0.13}$ alloy membrane at 673 K at an initial feed pressure of 100 kPa. The feed gas was allowed to recirculate in the feed side of the membrane without any H_2 replenishment. Thus, the hydrogen concentration in the feed side continuously decreases due to its permeation through the membrane. The change in hydrogen concentration in the feed side was measured using the residual gas analyser at an interval of 30 minutes. The results are shown in Figure 3.29 and Figure 3.30.

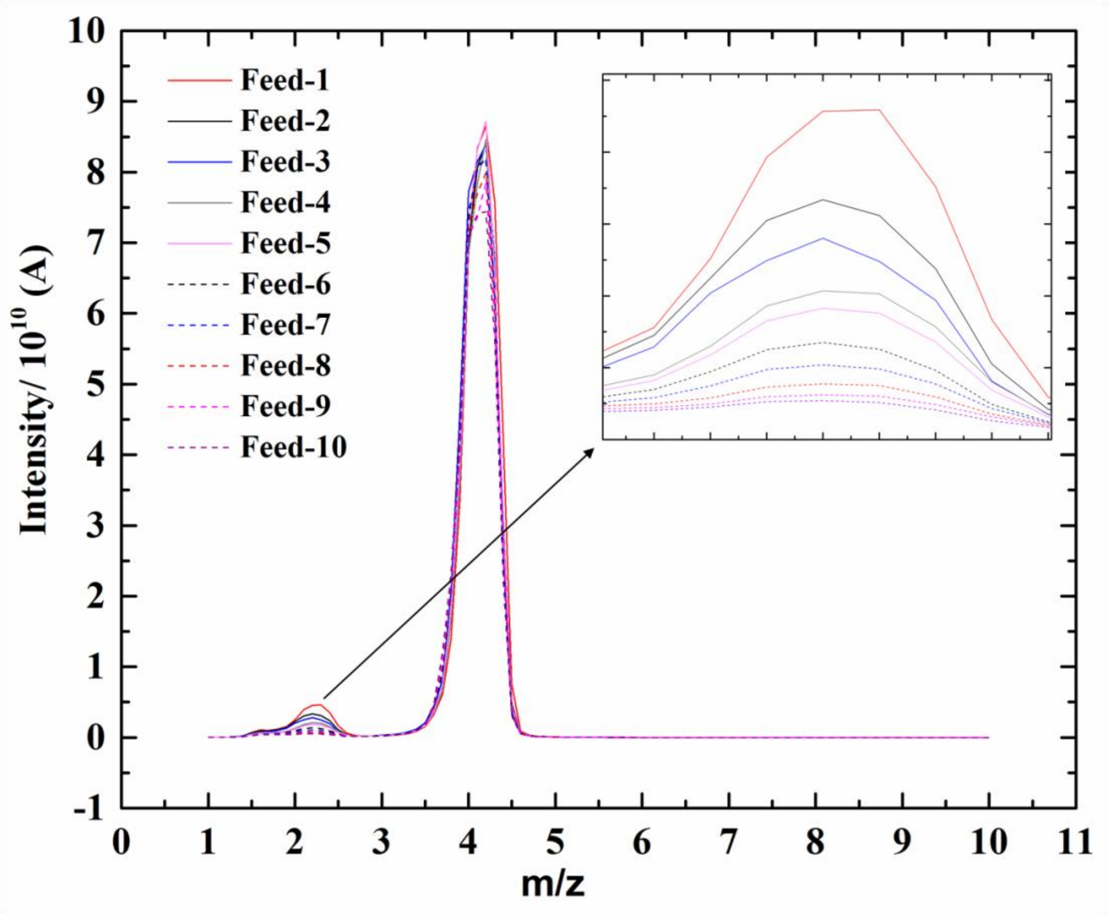

Figure 3.29. Mass Spectra of feed gas concentration with time

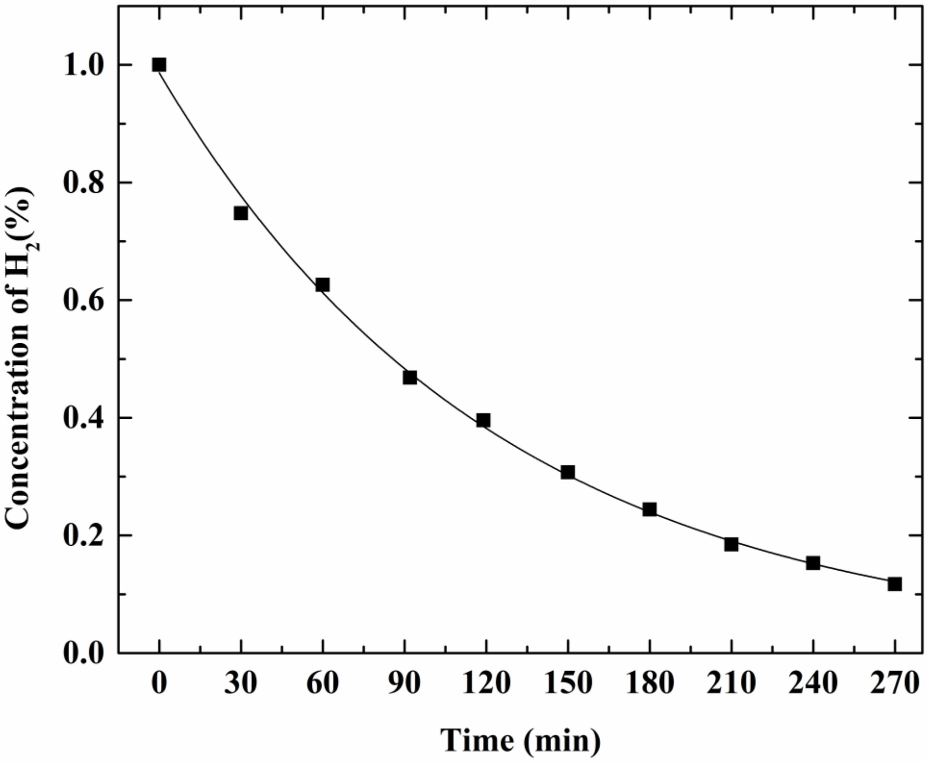

Figure 3.30. Variation of H_2 concentration in the feed gas mixture (He + H_2) with time

It is evident from these figures that, the hydrogen concentration in the feed stream decreases with time and it follows the exponential behaviour. During an experiment of 270 minutes, the hydrogen concentration in the synthetic feed gas mixture was found to decrease from 1.0 to 0.1 %. The rate of decrease in hydrogen concentration versus time was expressed as analytical expression by fitting the data using least squares method and the expression is given as:

$$\ln [H_2 \text{ in } \%] (\pm 0.005) = -0.0167 - 1.305 \cdot 10^{-4} \cdot (t/s) \qquad (3\text{-}17)$$

The considerable decrease in hydrogen concentration makes $Pd_{0.77}Ag_{0.10}Cu_{0.13}$ alloy membrane suitable for its application in purification of ^3He from tritium contamination.

3.4. Pressure-Composition-Temperature Measurements of $Pd_{0.77}Ag_{0.10}Cu_{0.13}$ alloy

3.4.1. Derivation of thermodynamic parameters

The pressure-composition isotherms for hydrogen/deuterium desorption reactions from the corresponding hydride/deuteride of $Pd_{0.77}Ag_{0.10}Cu_{0.13}$ alloy were generated in a temperature range of 313─393 K. The generated pressure-composition-temperature (PCT) profiles of $Pd_{0.77}Ag_{0.10}Cu_{0.13}$-$H_2$/$D_2$ system are shown in Figure 3.31 and Figure 3.32, respectively.

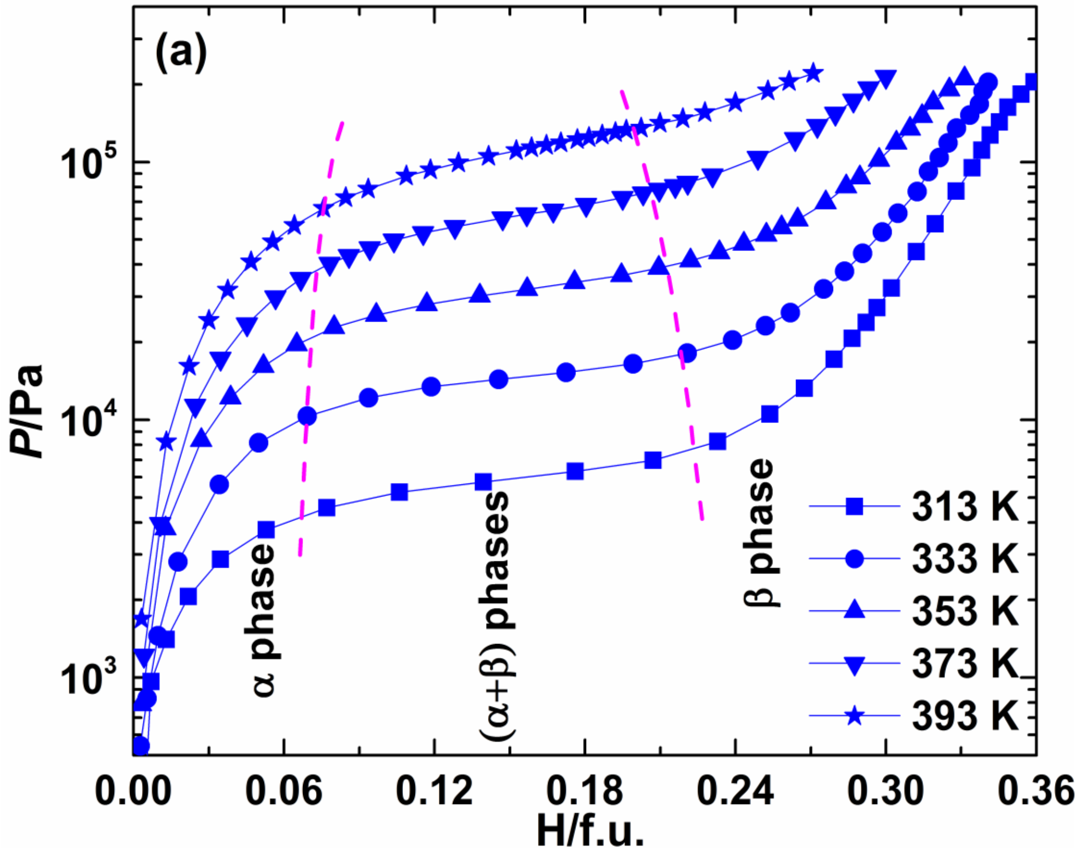

Figure 3.31. Desorption PCIs for $Pd_{0.77}Ag_{0.10}Cu_{0.13}$-$H_2$ reaction

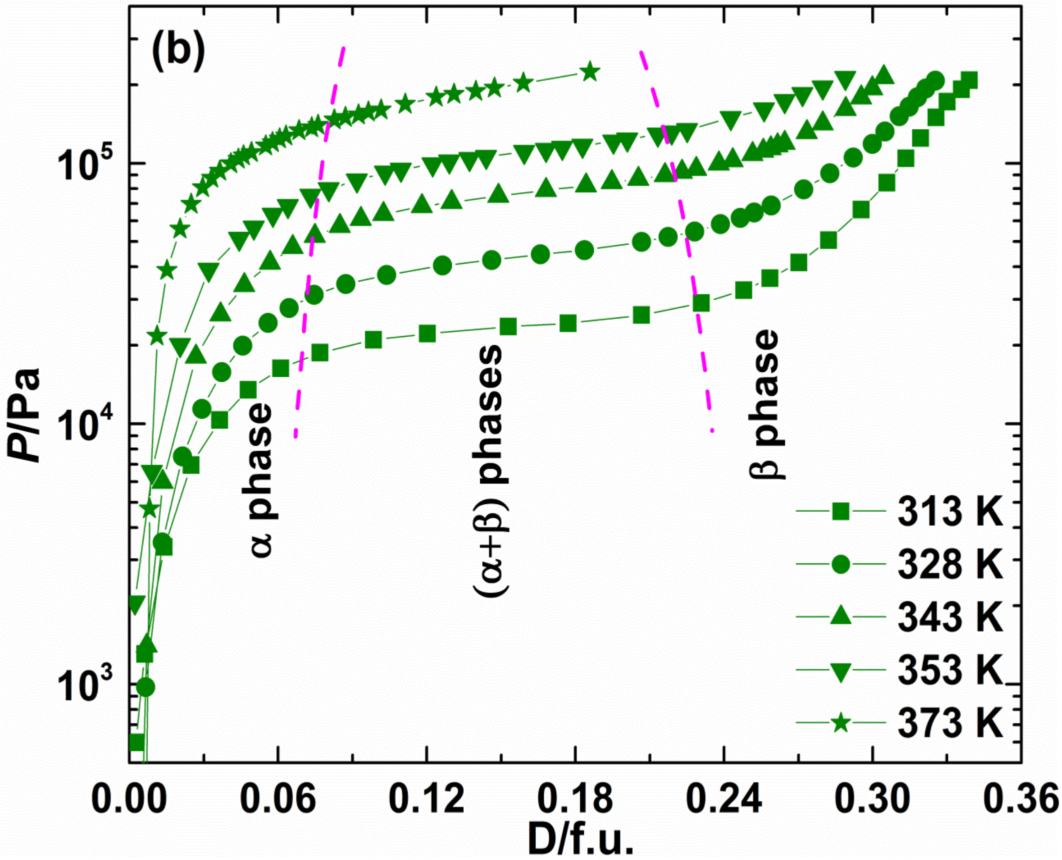

Figure 3.32. Desorption PCIs for $Pd_{0.77}Ag_{0.10}Cu_{0.13}$-$D_2$ reaction

Each PCI shows three different regions with distinct plateau pressure, where both the α and β phase coexist. Out of the three regions, the plateau region is most important, where the plateau width and the equilibrium plateau pressure are two important parameters which decide practical application of the alloys in hydrogen isotope separation applications. It is evident from the figures that the desorption equilibrium plateau pressure (P_{eq}) increases with temperature, whereas the plateau region of each PCI shrinks with rise in temperature. These figures show that at all experimental temperatures, the equilibrium plateau pressure of deuterium is higher than that of hydrogen showing normal hydrogen isotope effect. The equilibrium plateau pressure region is governed by the reaction:

$1/(y - x)\ MQ_y\ (s) = 1/(y - x)\ MQ_x\ (s) + ½\ Q_2\ (g)$ (3-18)

where, M = $Pd_{0.77}Ag_{0.10}Cu_{0.13}$ alloy, Q = H or D, x and y are the dilute (α) and the hydride (β) coexisting phase boundary compositions.

At a particular temperature, the magnitude of the desorption equilibrium pressure of Q_2 is fixed by the Gibbs free energy change $\Delta_r G^o$ which in turn is dependent on the enthalpy change $\Delta_r H^o$ and entropy change $\Delta_r S^o$ of the reaction. Hence, for comparison of equilibrium pressures of H_2 and D_2, Eq. (1.25) can be written as:

$ln\{P_{eq}(D_2)/P_{eq}(H_2)\} = -\{\Delta_r H^o_D - \Delta_r H^o_H\}/RT + \{\Delta_r S^o_D - \Delta_r S^o_H\}/R$ (3-19)

where, subscripts D and H represent the corresponding thermodynamic parameters for reactions with D_2 and H_2, respectively.

Further, the enthalpic contribution in equation (3-19) can be written as:

$(\Delta_r H^o_D - \Delta_r H^o_H) = \{\Delta_f H^o(MD_x, s) - \Delta_f H^o(MD_y, s)\} – \{\Delta_f H^o(MH_x, s) - \Delta_f H^o(MH_y, s)\}$

$= \{\Delta_f H^o(MD_x, s) - \Delta_f H^o(MH_x, s)\} –\{\Delta_f H^o(MD_y, s) –\Delta_f H^o(MH_y, s)\}$ (3-20)

The magnitudes of $\Delta_f H^o(MQ_x, s)$ and $\Delta_f H^o(MQ_y, s)$ are governed by the difference in zero-point vibrational energies (ZPE) of Q in the gas phase and Q in the interstitial site of crystal lattice of M. Since $Pd_{0.77}Ag_{0.10}Cu_{0.13}$ alloy have f.c.c. crystal structure, unlike Pd, Q atom preferentially occupies the octahedral interstitial sites. Further, occupancy of Q in MQ_y (β-phase) is much larger than that in MQ_x (α-phase). Hence, the magnitude and sign of $(\Delta_r H^o_D - \Delta_r H^o_H)$ largely depends upon $\{\Delta_f H^o(MD_y, s) – \Delta_f H^o(MH_y, s)\}$. According to the diagrammatic representation given by Sicking [92] shown in Figure.1.9, for the ZPE contributions in the metal-hydride system, $|\Delta_f H^o(MH_y, s)| > |\Delta_f H^o(MD_y, s)|$.

Similarly, the entropy contribution in Eq. (3.19) can be written as:

$(\Delta_r S^o_D - \Delta_r S^o_H) = 2/(y-x) \{S^o(MD_x, s) - S^o(MH_x, s)\} + \{S^o(Q_2, g) - S^o(H_2, g)\} – 2/(y-x) \{S^o(MD_y, s) - S^o(MH_y, s)\}$ (3-21)

The absolute entropy of the deuteride phase is always higher than that of corresponding hydride phase [160]. However, the difference in absolute entropies of MD_X and MH_X as well as MD_y and MH_y are very small compared to the difference in absolute entropies of gaseous D_2 and H_2 [160]. Hence, the entropy difference $(\Delta_r S^o_D- \Delta_r S^o_H)$ will be always positive. The difference in magnitude of thermodynamic parameters of desorption reaction for the corresponding pair of hydrogen isotopes, $|\Delta_r H^o|_{(Q = D)} - |\Delta_r H^o|_{(X = H)} < 0$ and $|\Delta_r S^o|_{(Q=H)} - |\Delta_r S^o|_{(Q=D)} > 0$, suggest that hydrogen has more affinity to remain associated with the alloy in the condensed phase than deuterium, showing normal hydrogen-isotope effect. Considering normal isotopic effect the trend in equilibrium pressure for $Pd_{0.77}Ag_{0.10}Cu_{0.13}$ alloy can be predicted to be: $P_{eq}(H_2) < P_{eq}(D_2) < P_{eq}(T_2)$. Thermodynamic data for the above reaction (3-18) were derived from the hydrogen/deuterium equilibrium plateau pressure (P_{eq}) for each isotherm corresponding to mid-point region of the plateau at X/f.u. = 0.15. These equilibrium plateau pressure data were used to construct the van't Hoff plot (plot of ln P vs. $1/T$) for both the hydrogen/deuterium desorption reaction which are shown in Figure 3.33.

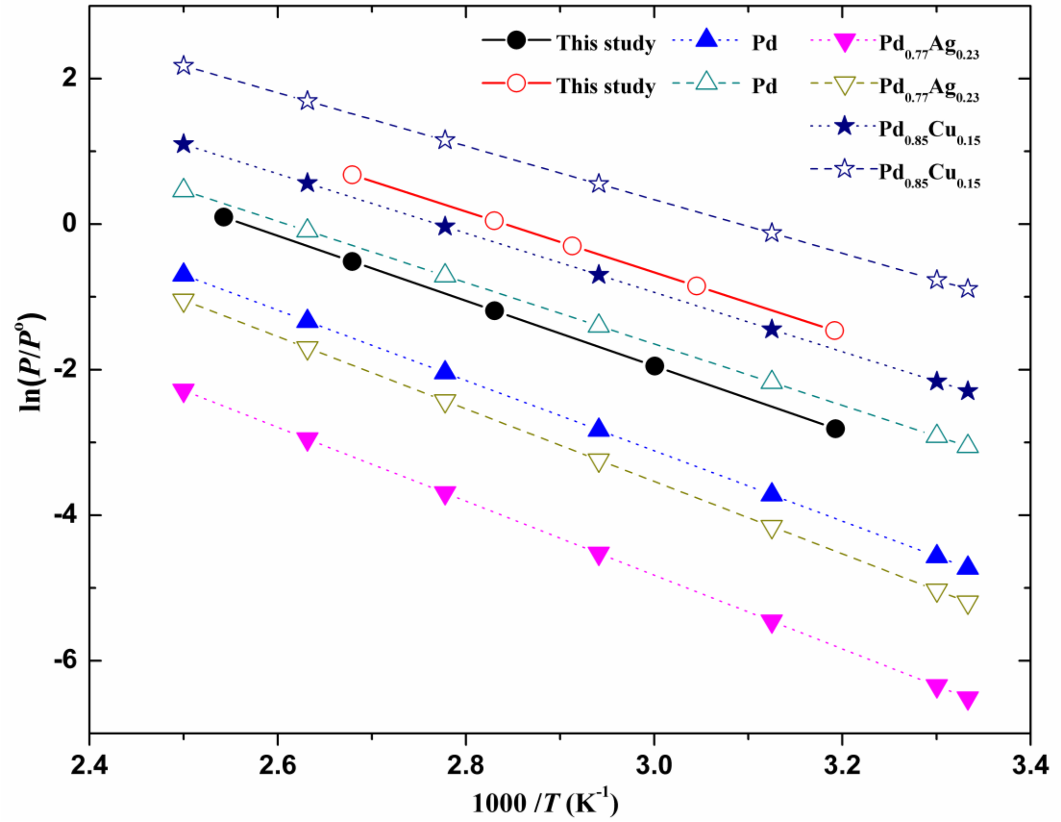

Figure 3.33. A comparison of van't Hoff plots (solid symbols: hydrides; hollow symbols: deuterides)

A linear relation was obtained for temperature dependent plateau pressure which is represented by van't Hoff relations. The relations obtained for $Pd_{0.77}Ag_{0.10}Cu_{0.13}$-$H_2/D_2$ can be represented by the following equations:

For $Pd_{0.77}Ag_{0.10}Cu_{0.13}$-$H_2$ system;

$$\log(P/P^o) = -\,4474.4\ /\ T(\mathrm{K}) + 11.5 \tag{3-22}$$

And for $Pd_{0.77}Ag_{0.10}Cu_{0.13}$-$D_2$ system;

$$\log(P/P^o) = -\,4173.7\ /\ T(\mathrm{K}) + 11.9 \tag{3-23}$$

The enthalpy ($\Delta_r H^o$) and entropy ($\Delta_r S^o$) of desorption reaction of $Pd_{0.77}Ag_{0.10}Cu_{0.13}$-$H_2/D_2$ derived from the van’t Hoff relation is listed in Table 3-6. Several authors have reported thermodynamic parameters for absorption/desorption reactions of Pd metal and different compositions of Pd-Ag and Pd-Cu alloys [161-165] employing different techniques. Thermodynamic data obtained in the present study are compared with those reported for Pd, Pd-Ag and Pd-Cu alloys in Table 3-6. A comparison of van't Hoff plots is also made in Figure 3.33 for same systems. However, there is no literature data available for thermodynamic parameters of Pd-Ag-Cu-H_2/D_2 desorption reactions for direct comparisons. Table 3-6 depicts that the enthalpy of reaction ($\Delta_r H^o$) shows a systematic variation with alloy composition. It is evident from the table that the $\Delta_r H^o$ for the ternary alloy $Pd_{0.77}Ag_{0.10}Cu_{0.13}$ (37.2 ± 0.3 (kJ/mol H_2)) and 34.7 ± 0.2 (kJ/mol D_2)) is lower in magnitude compared to Pd and Pd-Ag alloys and higher in magnitude compared to Pd-Cu alloys. From the Figure 3.33, it is observed that at a given temperature, the equilibrium desorption plateau pressure for different systems follows the trend: P_{eq} (Q_2) (Pd-Cu) > P_{eq} (Q_2)($Pd_{0.77}Ag_{0.10}Ag_{0.13}$) > P_{eq} (Q_2) Pd > P_{eq} (Q_2) Pd-Ag. The result is in accordance with the fact that the alloy having a smaller lattice constant results in shrinkage of the interstitial site which favors destabilization of the hydride phase thereby increasing the equilibrium pressure. The desorption temperature for release of 1bar of Q_2 gas from corresponding $Pd_{0.77}Ag_{0.10}Cu_{0.13}$-hydride/deuteride is listed in Table 3-6.

Table 3-6.Thermodynamic functions for desorption reactions of Pd-Ag-Cu-H_2/D_2, Pd-H_2/D_2, Pd-Ag-H_2/D_2 and Pd-Cu-H_2/D_2 systems

Alloy composition	Hydride		T_{des}	Deuteride		T_{des}	Temperature
	$\Delta_r H^o$ (kJ/mol H_2)	$\Delta_r S^o$ (J/(mol $H_2\cdot K$))	(K)	$\Delta_r H^o$ (kJ/mol D_2)	$\Delta_r S^o$ (J/(mol $D_2\cdot K$))	(K)	range (K)$^{\mathrm{Ref}}$
$Pd_{0.77}Ag_{0.10}Cu_{0.13}$[d]	**37.2 ± 0.3**	**95.4 ± 0.4**	**389**	**34.7 ± 0.2**	**98.6 ± 0.3**	**351**	**313-393**
Pd[d]	40.2	94.7	424	35.1	91.6	383	333 – 433[163]
$Pd_{0.90}Ag_{0.10}$ [d]	42.4	94.7	448	38.9	95.5	407	333 - 433[164]
$Pd_{0.77}Ag_{0.23}$ [d]	42.2 ± 0.5	86.5 ± 0.9	487	41.4 ± 0.2	94.8 ± 0.3	437	374 – 419[162]
$Pd_{0.85}Cu_{0.15}$ [d]	33.9	84-96	-	30.6	84-96	-	293 - 413[161]
$Pd_{0.85}Cu_{0.15}$ [c]	30.0	83.8	357	-	-	-	303[165]
$Pd_{0.80}Cu_{0.20}$ [c]	28.4	86.8	327	-	-	-	303[165]

[a]:absorption PCIs, [d]:desorption PCIs, [c]: calorimetry

The data in the present study reveal that desorption temperature for deuteride is lower compared to that of the hydride indicating normal hydrogen isotope effect. Hence it can be inferred that the desorption temperature of Q_2 from $Pd_{0.77}Ag_{0.10}Cu_{0.13}$ alloy will follow the following trend: $T_{des}(H_2) > T_{des}(D_2) > T_{des}(T_2)$. Further, Table 3.6 reveals that the desorption temperature of Pd and Pd alloys follows the trend: $T_{des}(Q_2)$ (Pd-Cu) < $T_{des}(Q_2)(Pd_{0.77}Ag_{0.10}Ag_{0.13})$ < $T_{des}(Q_2)$Pd < $T_{des}(Q_2)$ Pd-Ag. These favourable thermodynamic properties of the ternary alloy such as lower $\Delta_r H^o$, lower T_{des} and higher equilibrium plateau pressure compared to pure Pd enables its application in separation and purification of hydrogen isotopes in self-displacement gas chromatography and membrane reactors.

3.4.2. Derivation of isotope separation factor

Efficiency of separation of hydrogen isotopes greatly depends on the separation factor (α) which in turn depends on the magnitude of temperature dependent hydrogen-isotope effect on the equilibrium plateau pressures. The value of α for a plateau region for a particular isotherm is determined by the following equation [166, 167]:

$$\alpha = (P^o(D_2)/P^o(H_2))^{1/2} \tag{3-24}$$

where, $P^o(D_2)$ and $P^o(H_2)$ are the equilibrium plateau pressures of deuterium and hydrogen at a given temperature. The values of α were calculated from the experimental PCIs for the $Pd_{0.77}Ag_{0.10}Cu_{0.13}$-$H_2/D_2$ systems. The values of α at room temperature are found to be 2.00, 2.27, 1.93 and 2.02 for $Pd_{0.77}Ag_{0.10}Cu_{0.13}$-$H_2/D_2$, Pd-$H_2/D_2$, Pd-Ag-H_2/D_2 and Pd-Cu-H_2/D_2 systems [161, 162, 168], respectively and the variation of (ln α) with reciprocal temperature ($1/T$) is shown in Figure 3.34. For room temperature self-displacement chromatography application, the alloy should have higher value of α and lower value of $\Delta_r H$. A comparison of both α and $\Delta_r H$ for Pd,

$Pd_{0.77}Ag_{0.23}$, $Pd_{0.85}Cu_{0.15}$ and $Pd_{0.77}Ag_{0.10}Cu_{0.13}$ alloy suggest that the preferable order of applicability of these materials for use in room temperature self-displacement gas chromatography is: $Pd_{0.77}Ag_{0.10}Cu_{0.13} \approx Pd_{0.85}Cu_{0.15} > Pd > Pd_{0.77}Ag_{0.23}$.

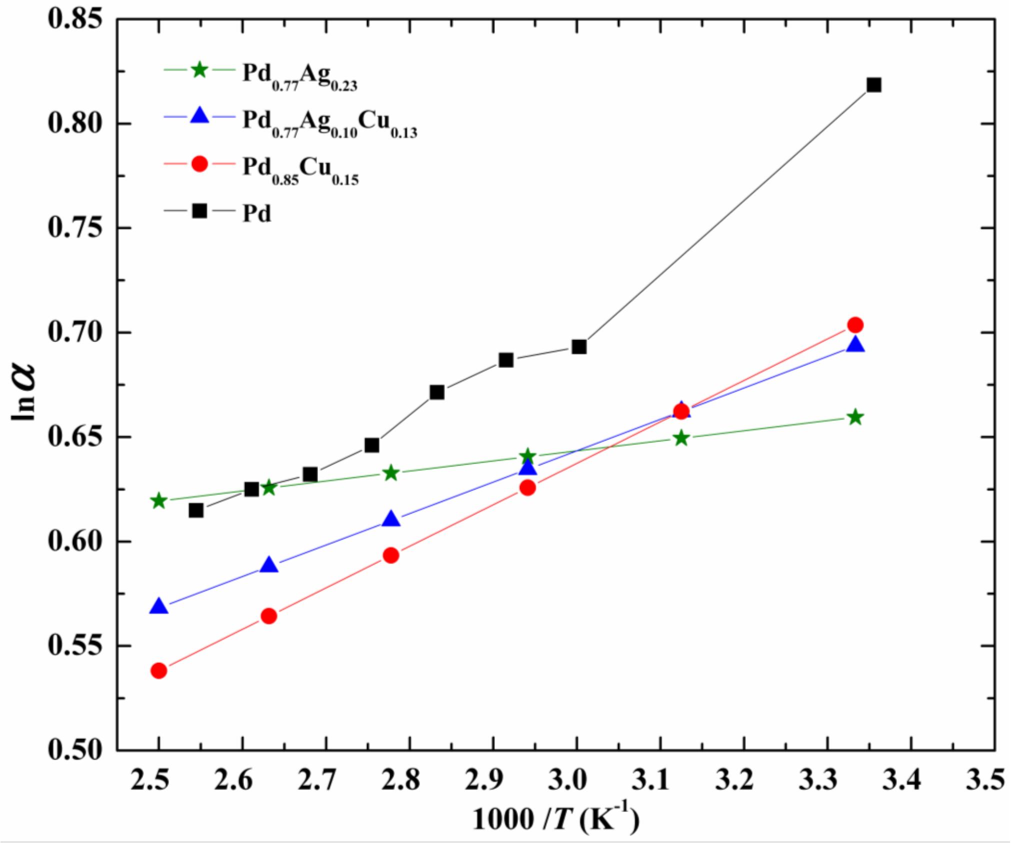

Figure 3.34. Comparison of hydrogen isotope separation factor (α)

3.5. Kinetics of hydrogen/deuterium absorption in $Pd_{0.77}Ag_{0.23}$ and $Pd_{0.77}Ag_{0.10}Cu_{0.13}$ alloy

The reactionof absorption of hydrogen/deuterium in $Pd_{0.77}Ag_{0.23}$ and $Pd_{0.77}Ag_{0.10}Cu_{0.13}$ alloy can be represented as:

$$Q_2\ (g) = 2[Q]_{alloy} \tag{3-25}$$

This absorption reaction is a complex gas-solid reaction in which a series of steps such as; transport of Q_2 molecules toward the alloy surface, physisorption, dissociative chemisorption, diffusion of atomic Q into the bulk and formation of hydride/deuterides are involved. The rate-limiting process of reaction (3-25) is conventionally determined by measuring dependence of reaction rate with time-temperature-hydrogen/deuterium pressure and concentration. Most of the kinetic measurements performed under constant pressure assume that diffusion of hydrogen/deuterium in metal/alloy is the rate limiting step. However, for constant volume measurements, at a particular temperature, the absorption of hydrogen/deuterium results in decrease in pressure with time till thermodynamic equilibrium is achieved. It is reported by Fernandez et al. [169] that for constant volume measurements, physisorption is not considered as the rate limiting step because of low activation energy.

In the present study, the constant volume kinetic data for the absorption reaction of H_2/D_2 on $Pd_{0.77}Ag_{0.23}$ alloy were generated in the temperature range 335 - 394 K with a step of 20 K. The time-dependent pressure and concentration for H_2 and D_2 absorption on $Pd_{0.77}Ag_{0.23}$ alloy are shown in Figure 3.35 and Figure 3.36, respectively. It is evident from the figures that the absorption of hydrogen/deuterium by the alloy results in a sharp decrease in pressure until complete saturation is reached. The concentration of hydrogen/deuterium in the alloy (Q/f.u) was calculated from the decrease in pressure due to hydrogen absorption. From the Figure 3.35 and Figure 3.36 it is clear that with the progress in reaction the concentration of hydrogen in the alloy increases for a certain period of time and then becomes constant after the thermodynamic equilibrium is attained.

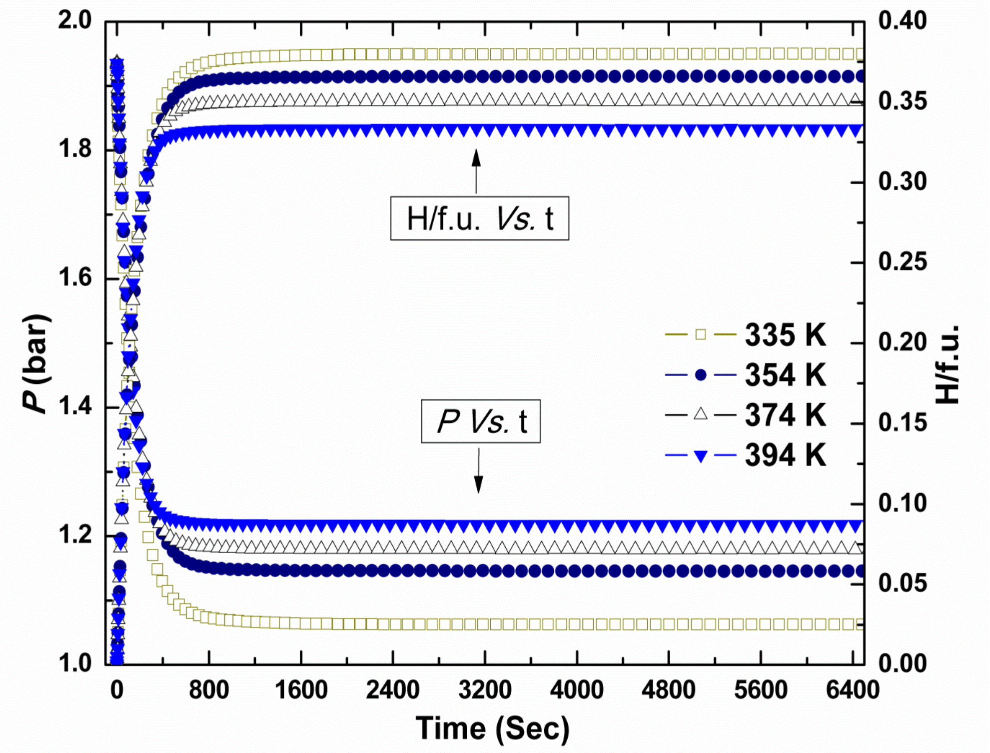

Figure 3.35. Kinetic plot for $Pd_{0.77}Ag_{0.23}$-H_2 absorption reaction

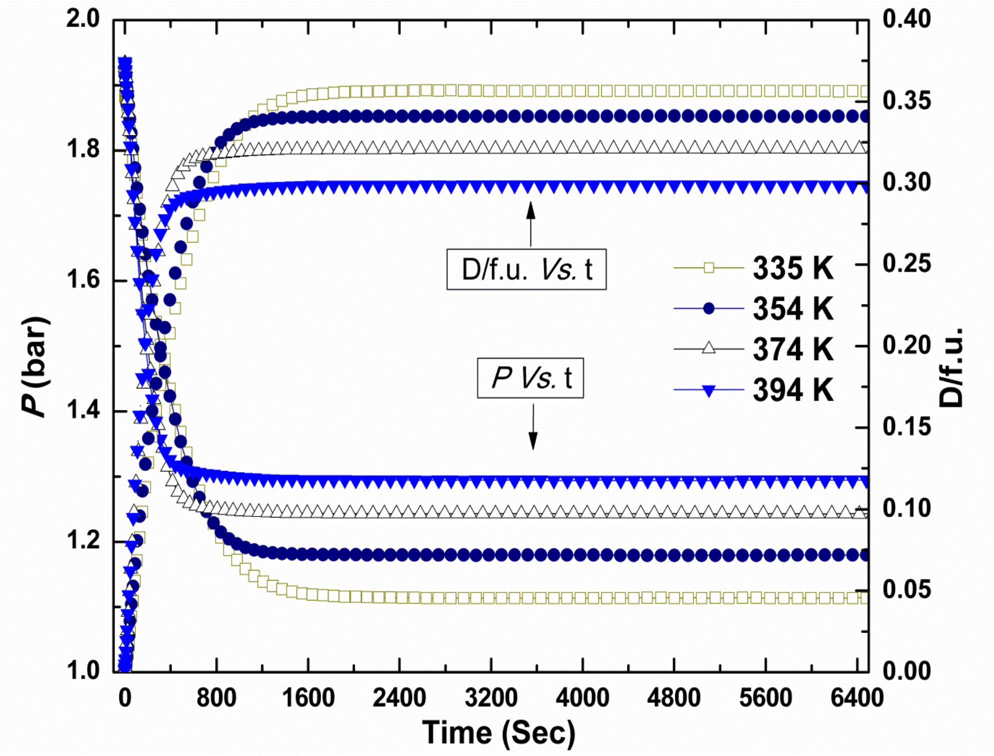

Figure 3.36. Kinetic plot for $Pd_{0.77}Ag_{0.23}$-D_2 absorption reaction

Further, it is observed that with increase in temperature the capacity of hydrogen absorption decreases, which indicates that at higher temperature the hydrogen/deuterium prefers to remain in gas phase rather than the solid alloy phase. The rate of reactions was derived by fitting the kinetic data in to different proposed kinetic models. Fernandez et al. [169] have proposed simple differential equations for different rate limiting steps of isochoric hydrogen absorption measurements. Those model equations were fitted to our experimental data, and it was observed that the following equation:

$$-dP/dt = k\,(P-P_f) \qquad (3\text{-}26)$$

pertaining to chemisorption as the rate limiting step best fits to our experimental data. This equation upon integration leads to:

$$\ln[(P-P_f)/(P_i-P_f)] = -kt \qquad (3\text{-}27)$$

where, k is apparent rate constant, P is the instantaneous pressure at time t, P_i is the initial pressure and P_f is the final pressure. The plot of $\ln[(P-P_f)/(P_i-P_f)]$ vs. t for both hydrogen and deuterium absorption are shown in Figure 3.37 and Figure 3.38. It is apparent from both these figures that a linear relation is observed for the region where the hydride phase (β) co-exists with the dilute phase (α). Hence, the apparent rate constants at different temperatures were derived in this bi-phasic (α + β) region. The figures depict faster reaction kinetics of hydrogen absorption compared to that of deuterium absorption.

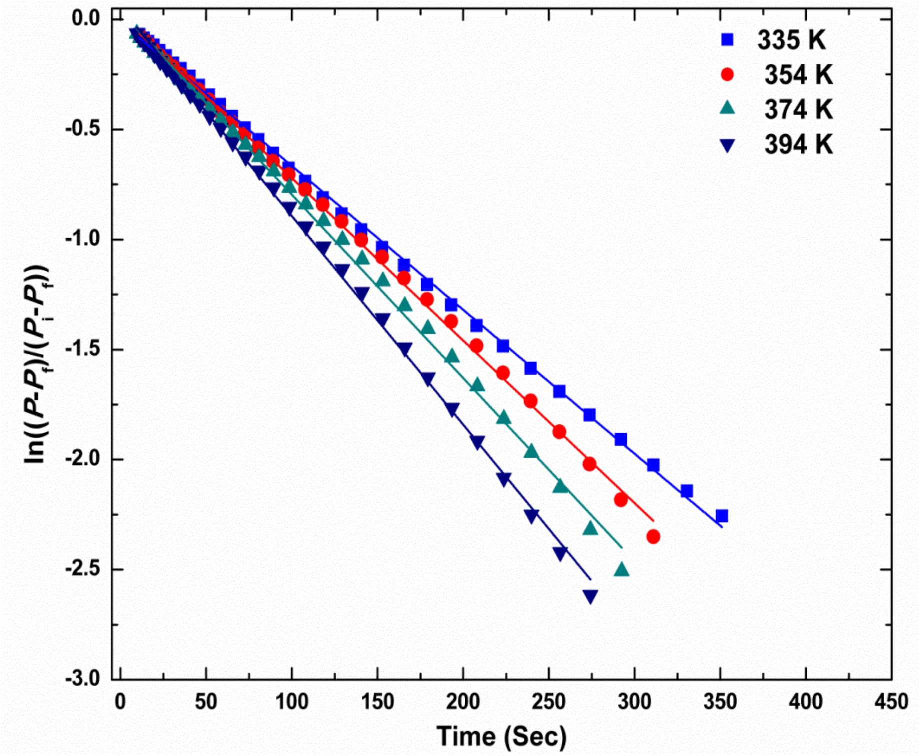

Figure 3.37. The plot of ln[(P-P_f)/(P_i-P_f)] vs. t for $Pd_{0.77}Ag_{0.23}$-H_2 absorption

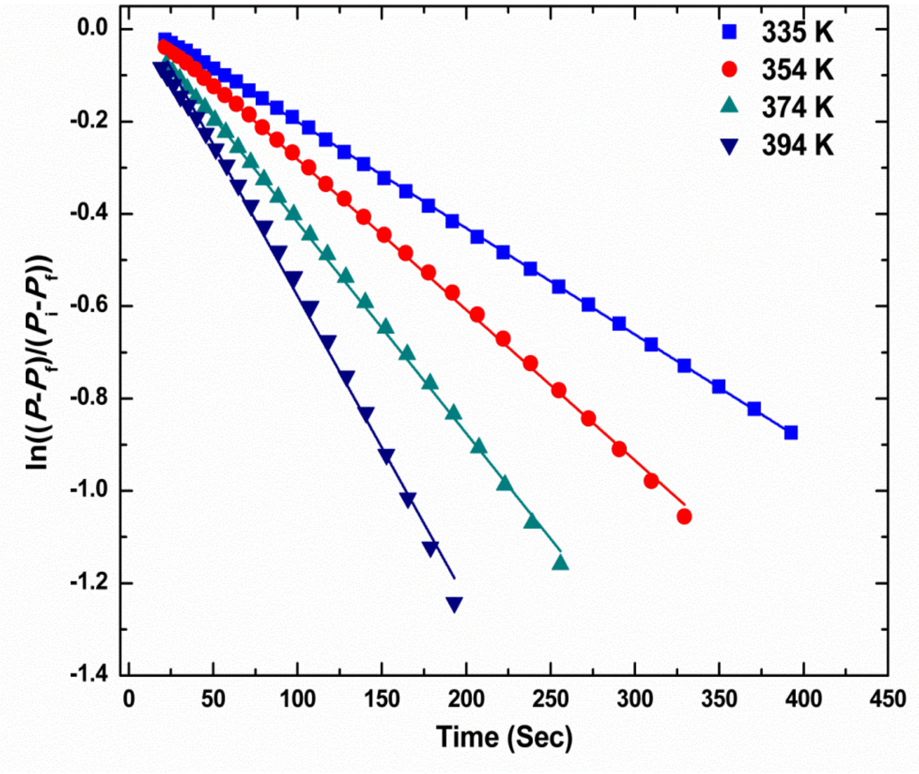

Figure 3.38. The plot of ln[(P-P_f)/(P_i-P_f)] vs. t for $Pd_{0.77}Ag_{0.23}$-D_2 absorption

Similarly, isochoric measurements on $Pd_{0.77}Ag_{0.10}Cu_{0.13}$-$H_2/D_2$ absorption reaction were carried out in the temperature range 303-333 K at a step of 10 K. The time dependent pressure and concentration (Q/f.u.) are shown in Figure 3.39 and Figure 3.40. Hydrogen/deuterium absorption results in decrease in gas pressure with respect to time until the samples are completely saturated. A flat line showing no further decrease in pressure with time indicates the achievement of thermodynamic equilibrium.

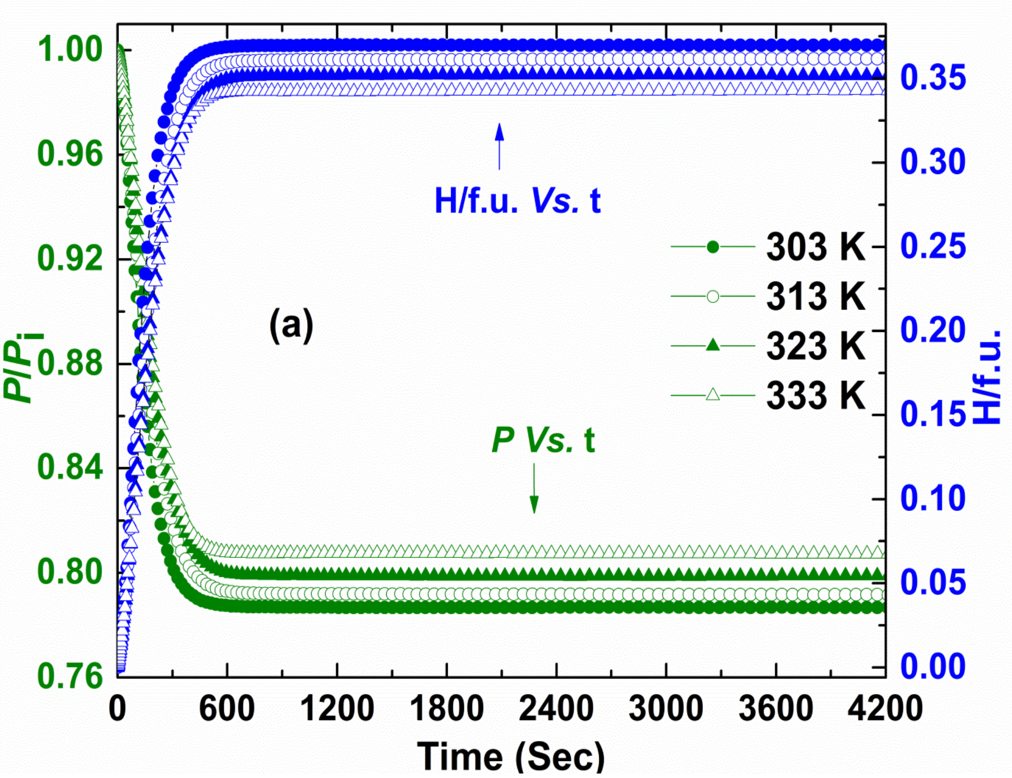

Figure 3.39. Kinetic plot for $Pd_{0.77}Ag_{0.10}Cu_{0.13}$-$H_2$ absorption reaction

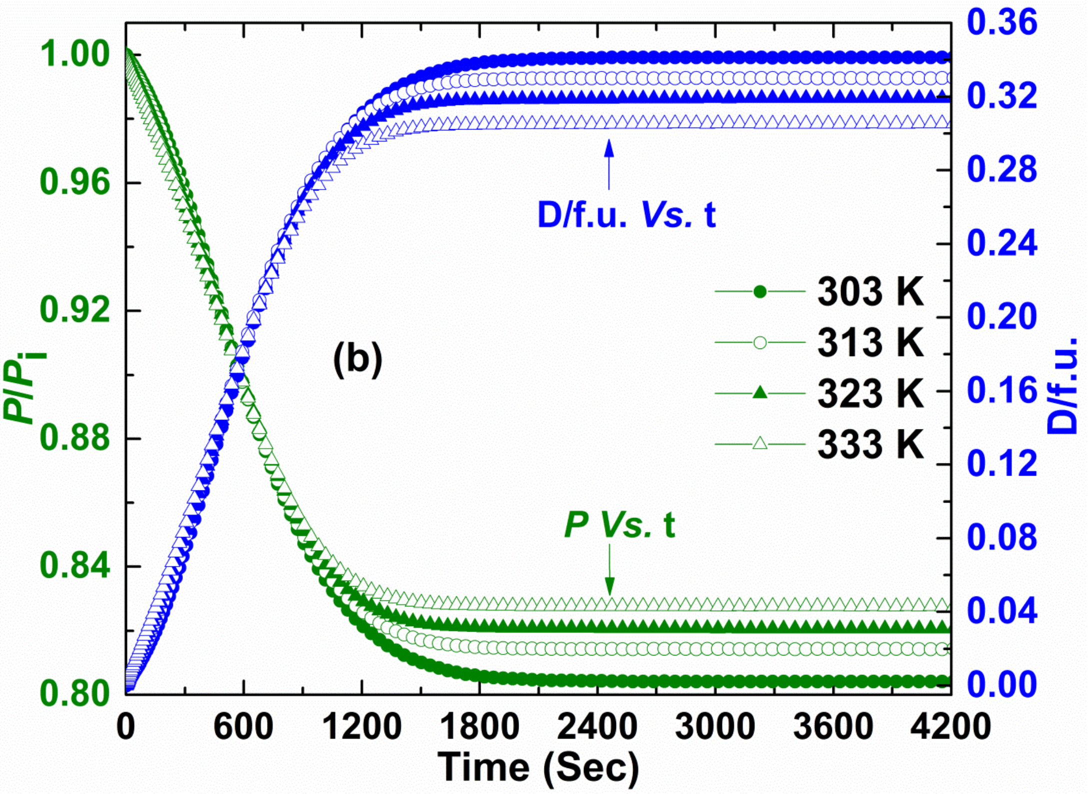

Figure 3.40. Kinetic plot for $Pd_{0.77}Ag_{0.10}Cu_{0.13}$-$D_2$ absorption reaction

With increase in the reaction temperature desorption reaction becomes preferable than absorption resulting in decrease of H_2/D_2 absorption capacity of the alloys. The figures also depicts slower absorption rate of deuterium compared to hydrogen. Different types of kinetic models are used to fit the experimental data to evaluate the kinetic parameters. In cases, where the kinetic parameters lead to negative activation energy, the model assumes no significance. It was observed that the pressure and concentration dependent model proposed by Wang and Suda [170] best fits to our kinetic data. The model equation is given as:

$$dC/dt = k(T)\cdot(P/P_{eq})^{a}\cdot\{1-(P_f/P)^{a}\cdot(C/C_f)^{b}\} \qquad (3\text{-}28)$$

where, $k(T)$ is the absorption rate constant; P and P_f are the pressure at time t and final pressure, respectively. P_{eq} is the equilibrium plateau pressure; C and C_f are the concentrations (Q/f.u.) at time t and at final pressure P_f, respectively. The constants a and b are the order of the reaction with respect to the pressure and concentration, respectively.

Eq. 3-28 can be alternatively written as:

$$dC/dt = k(T)\cdot F(C,P) \qquad (3\text{-}29)$$

where, $F(C,P)$ represents the pressure and concentration dependent terms in the right hand side of Eq. 3-28. The plot of dC/dt vs. $F(C,P)$ at different temperatures are shown in Figure 3.42 and Figure 3.42. It is observed that a linear relation exists in the concentration range where the hydride phase (β) coexists with the dilute solution phase (α). Hence, kinetic parameters are evaluated for this bi-phasic region. The values of adjustable parameters a and b and the temperature dependent rate constant $k(T)$ are listed in Table 3.7.

Table 3-7. The values of adjustable parameters *a* and *b* and the temperature dependent rate constant k(*T*) for absorption of hydrogen/deuterium in $\mathbf{Pd_{0.77}Ag_{0.10}Cu_{0.13}}$ alloy

Temperature (K)	Hydrogen			Deuterium		
	a	*b*	*k*(*T*), ((Q/f.u.)/s)	*a*	*b*	*k*(*T*), ((Q/f.u.)/s)
303	1.2	2	2.3573E-4	1.2	2	2.7548E-4
313	1.3	2	3.1973E-4	1.3	2	4.7704E-4
323	1.4	2	4.3928E-4	1.4	2	8.8362E-4
333	2	2	5.9251E-4	1.5	2	0.00163

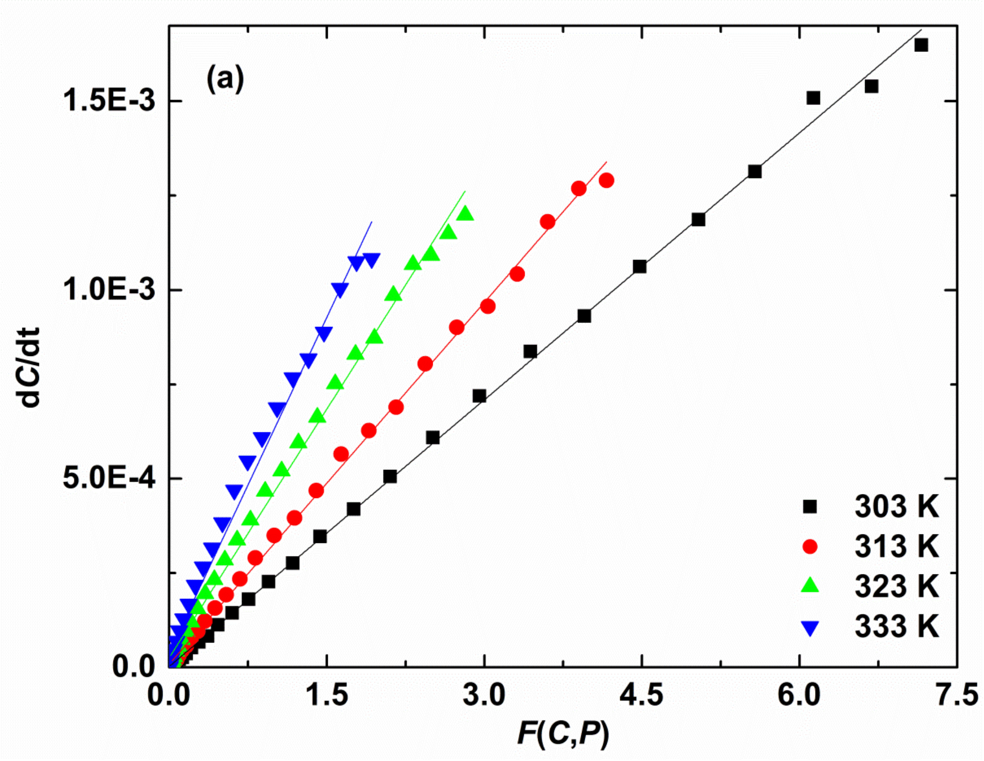

Figure 3.41. Plot of *dC/dt* vs. *F(C,P)* for $Pd_{0.77}Ag_{0.10}Cu_{0.13}$-$H_2$ system

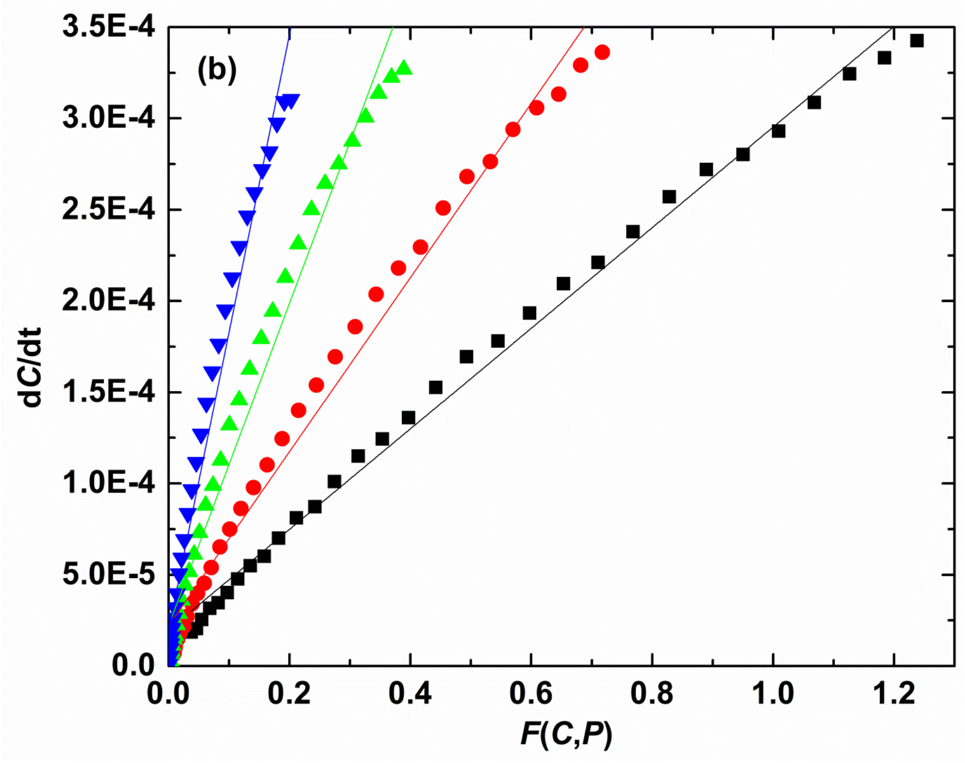

Figure 3.42. Plot of *dC/dt* vs. *F(C,P)* for $Pd_{0.77}Ag_{0.10}Cu_{0.13}$-$D_2$ system

It is observed that the value of *a* varies within 1 to 2 whereas the value of *b* is 2 at all temperatures. The predominance of concentration term over the pressure term suggests that diffusion of Q through the hydride/deuteride is the rate limiting step.

Arrhenius plot, logarithm of apparent rate constant (ln k) versus reciprocal temperature (1/*T*), was constructed using the values of apparent rate constants at different temperatures. Arrhenius plots for hydrogen/deuterium absorption by $Pd_{0.77}Ag_{0.23}$ and$Pd_{0.77}Ag_{0.10}Cu_{0.13}$alloy are shown in Figure 3.43 and Figure 3.44, respectively.

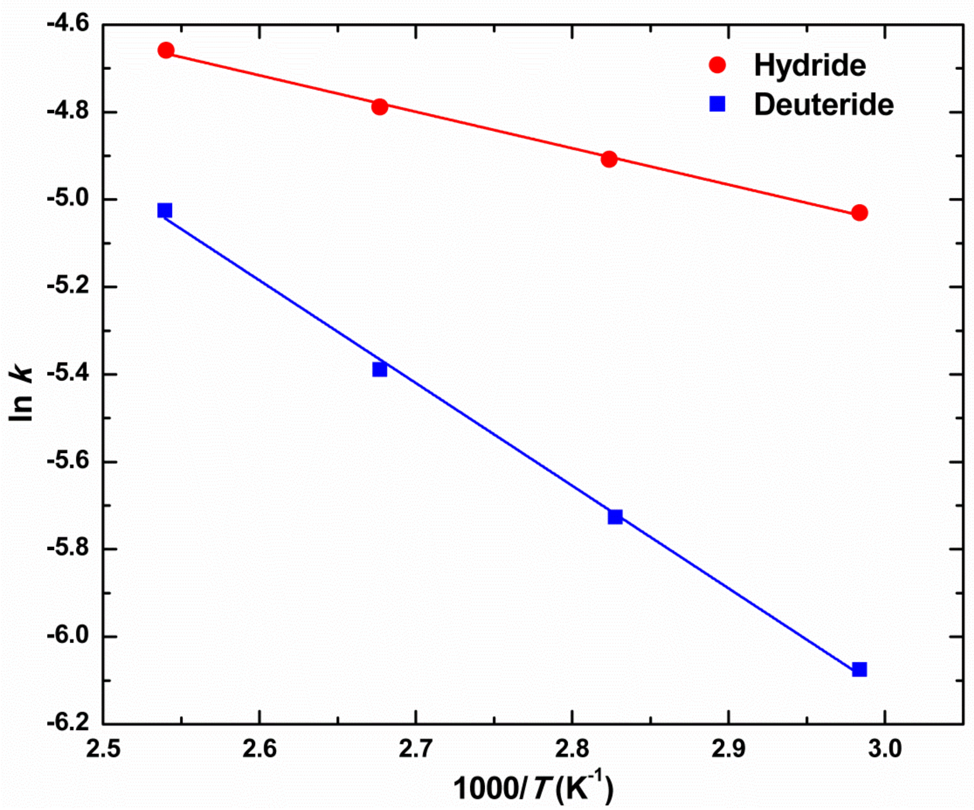

Figure 3.43. Arrhenius plots for H_2/D_2 absorption by $Pd_{0.77}Ag_{0.23}$ alloy

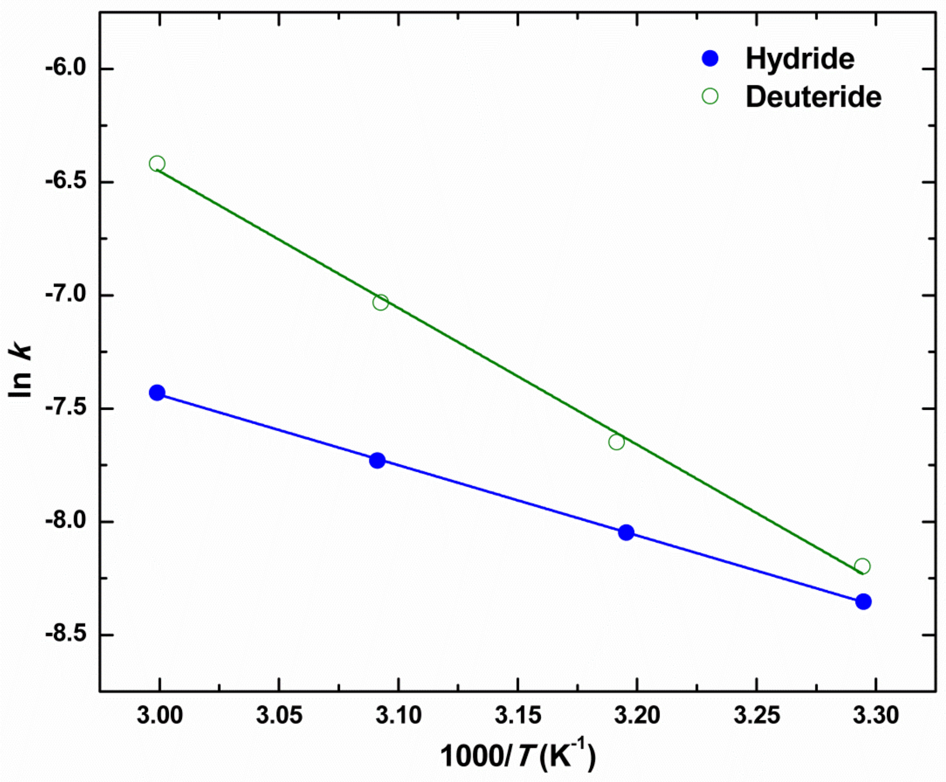

Figure 3.44. Arrhenius plots for H_2/D_2 absorption by $Pd_{0.77}Ag_{0.10}Cu_{0.13}$ alloy

The activation energies for the absorption of hydrogen/deuterium were derived from the Arrhenius equation;

$$k = A\cdot\exp\left(-E_a/k_BT\right) \quad (3\text{-}30)$$

where, A, E_a, k_B are the frequency factor, the apparent activation energy and the Boltzmann constant, respectively. The corresponding values of E_a and frequency factors for absorption reaction are listed in Table 3.8. From the table, it is evident that the activation energy of deuterium absorption is higher than that of hydrogen for both the binary and ternary alloy in the bi-phasic ($\alpha + \beta$) region.

Table 3-8. Activation energy and pre-exponential factor for H_2/D_2 absorption in $Pd_{0.77}Ag_{0.23}$ and $Pd_{0.77}Ag_{0.10}Cu_{0.13}$ alloys

System	Ea(kJ/mol Q_2)	A((Q/f.u.)/s)
$Pd_{0.77}Ag_{0.23}$ -H_2	6.9 ± 0.2	$7.8\text{x}10^{-2}\pm0.2$
$Pd_{0.77}Ag_{0.23}$ -D_2	19.5 ± 0.6	2.513±0.3
$Pd_{0.77}Ag_{0.10}Cu_{0.13}$-$H_2$	25.8 ± 0.2	6.55±0.1
$Pd_{0.77}Ag_{0.10}Cu_{0.13}$-$D_2$	50.2 ± 1.6	$1.16\text{x}10^{5}\pm0.4$

Further the values of E_a are for Q_2 absorption in the ternary $Pd_{0.77}Ag_{0.10}Cu_{0.13}$ alloy (25.8 ± 0.2kJ/mol H_2) and (50.2 ± 1.6kJ/mol D_2) were found to be higher than those for $Pd_{0.77}Ag_{0.23}$ alloy (6.9 ± 0.2 kJ/mol H_2 and 19.5 ± 0.6 kJ/mol D_2) and comparable to that of palladium (28.4 kJ/mol H_2). The difference in values of E_a for Pd, $Pd_{0.77}Ag_{0.10}Cu_{0.13}$ and $Pd_{0.77}Ag_{0.23}$ may be due to the difference in mechanism of hydrogen absorption in these materials. Further, the activation energies for absorption of hydrogen by $Pd_{0.77}Ag_{0.10}Cu_{0.13}$ alloy is comparable to the activation energy of hydrogen diffusion in Pd (approximately 25 kJ/mol H_2) as reported in the literature [171]. This is consistent with our observation that in the pressure and concentration dependent model, the concentration term predominates over the pressure term resulting the diffusion of Q as the rate limiting step. The kinetics of hydrogen absorption in palladium and Pd-Ag alloys have been studied by Auer and Grabke [171] with the aid of resistance measurements in a flow apparatus in the temperature ranges 293-423 K. However, they have reported the kinetic data only for the single phase regions and concluded that the rate determining step is the dissociation of the H_2

molecule on the metal surface. The activation energy for hydrogen absorption reaction is 28.5 kJ/mol H_2 for pure palladium and in the range of 29.3 to 37.6 (kJ/mol H_2) for $Pd_{1-z}Ag_z$ (z = 0.1 to 0.4). Johansson et al. [172] have studied the kinetics of hydrogen adsorption on palladium and palladium hydride at 1 bar and found out negligible difference in the rate of hydrogen splitting between α- and β-phases. The activation energy of hydrogen absorption quoted by Johansson et al. [172] is ~29 kJ/mol H_2. To the best of author's knowledge, the kinetics of hydrogen/deuterium absorption in Pd-Ag and Pd-Ag-Cu alloys in the bi-phasic (α + β) region is not reported in the literature for direct comparison. However, the activation energy of hydrogen absorption by $Pd_{0.77}Ag_{0.23}$ obtained in the present study is considerably lower compared to both the literature values reported for single phase region of pure palladium and Pd-Ag alloys [171, 173]. Since, kinetic data depends on many factors like method of measurement, sample size and shape, surface impurity and heat treatment; it is apparently difficult to compare results obtained by different authors.

The faster kinetics of H_2/D_2 absorption reaction on $Pd_{0.77}Ag_{0.23}$ and $Pd_{0.77}Ag_{0.10}Cu_{0.13}$ reaction indicates the suitability of these alloys for their application in hydrogen purification membranes. The relatively slower kinetics of H_2/D_2 absorption on $Pd_{0.77}Ag_{0.10}Cu_{0.13}$ alloy compared to the $Pd_{0.77}Ag_{0.23}$ alloy can be ascribed to the difference in the rate determining steps.

CHAPTER 4

SUMMARY AND CONCLUSION

Chapter 4. Summary and Conclusion

Palladium, Palladium-silver and Palladium-silver-copper metallic membranes were synthesized by both conventional metallurgical route and electroless plating method. The membranes were characterized for structure, morphology and composition employing different techniques. Hydrogen and deuterium permeation studies were carried out using the membranes prepared by metallurgical route. Thermodynamic and kinetic measurements of H_2/D_2 absorption/desorption reactions on these membranes were carried out for evaluating their performance in the field of hydrogen isotope separation and purification.

In the metallurgical route, pure Pd, $Pd_{0.77}Ag_{0.23}$ and $Pd_{0.77}Ag_{0.10}Cu_{0.13}$ alloy membranes of 100 μm thickness were synthesized by arc melting and cold rolling method. The structural characterization revealed that $Pd_{0.77}Ag_{0.23}$ and $Pd_{0.77}Ag_{0.10}Cu_{0.13}$ alloy membrane have single f.c.c crystal structure similar to Pd. It was observed that with reference to pure palladium, the binary alloy $Pd_{0.77}Ag_{0.23}$ has an expanded lattice, whereas the ternary alloy $Pd_{0.77}Ag_{0.10}Cu_{0.13}$ has a contracted lattice. The alloys retain same f.c.c structure in the temperature range of 298 to1023 K determined by high temperature X-ray diffraction method. Further, pure palladium foil shows preferred orientation whereas the alloys under same condition of annealing do not show preferred orientations. The lattice parameters of both the binary and ternary alloys show negative deviation from the Vegard's law in the entire temperature range of investigation and deviation increases with increase in temperature. For both the alloys, variation of lattice constant with temperature best fits to second order polynomial equation. The coefficient of linear thermal expansion increases linearly with temperature. The coefficient of liner thermal expansion shows the trend: α_T (Pd)

> α_T ($Pd_{0.77}Ag_{0.23}$) > α_T ($Pd_{0.77}Ag_{0.10}Cu_{0.13}$). The average values of α_T are found to be: 12.65×10^{-6} K^{-1}, 10.24×10^{-6} K^{-1} and $9.32 \times 10^{-6} K^{-1}$ for Pd, $Pd_{0.77}Ag_{0.23}$ and $Pd_{0.77}Ag_{0.10}Cu_{0.13}$, respectively, at the average experimental temperature of 660.5 K. X-ray Debye temperatures for $Pd_{0.77}Ag_{0.23}$ and $Pd_{0.77}Ag_{0.10}Cu_{0.13}$ have been calculated by using integrated intensity data of higher diffraction lines with a guessed initial value of Θ_M at 298 K. The value of X-ray Debye temperature for the alloy $Pd_{0.77}Ag_{0.23}$ and $Pd_{0.77}Ag_{0.10}Cu_{0.13}$ are found to be 225±10 K and 165±10 K, respectively.

Pd based metallic membranes were prepared by electroless plating method over porous stainless steel (PSS) disc using different plating baths. Various paramters like sensitization/activation of the substrate, effect of pH and addition of hydrazine was studied to evaluate the plating efficiency. It was observed that cleaning and activation of the substrate surface plays an important role in efficient plating. Temperature and pH of the plating bath are the two major parameters for better bath stability. The temperature of the plating bath was maintained constant througout the experiment. For Pd and Ag deposition the bath temperature was kept constant at 333 K and for Cu deposition the temperature was maintained at 298 K. It was observed that excellent bath stability and efficient plating was achived at pH = 10 for Pd and Ag bath and pH = 11 for Cu bath. It was also observed that bulk addition of the reducing agents immediately destabilizes the plating bath thereby preventing depostion of metals on PSS substrate. Hence controlled addition of haydrazine is found to be a pre-requisite condition for effciecient plating. For getting dence metallic membrane, multiple sequential plating is found to be necessary. The experiments on electroless plating of Pd-Ag and Pd-Ag-Cu alloy membrane deposition reveils, annealing the deposited film in hydrogen atompsohre is a necessary condition for formation of alloy membrane. Further, sequential deposition of metals was found to be an efficient way compared to co-deposition route for alloy membrane synthesis. Pd, $Pd_{0.65}Ag_{0.35}$ and $Pd_{0.74}Ag_{0.14}Cu_{0.12}$ alloy membranes of 30, 36 and 32 µm thickness, respectively were successfully synthesized in this method. The SEM analysis of the annealed membranes revealed that the membranes prepared by this method have finite defects due to presence of very small pinholes. The outcome of the present investigation suggest that cost effective membranes with minimum pinhole defects prepared by electroless plating can be used for purification of industrially produced hydrogen, where infinite hydrogen selectivity is not an important criteria. However, these membranes cannot be used for ITER fuel cycle applications, where infinite hydrogen selectivity is a prime requirement.

Hydrogen and deuterium permeation behaviour of $Pd_{0.77}Ag_{0.23}$ and $Pd_{0.77}Ag_{0.10}Cu_{0.13}$ alloy membranes of ~100 µm thickness were investigated for their intended application in recovery and purification of hydrogen isotopes. Both the alloy membranes were found to be efficient to purify hydrogen from the impurity over entire range of gas composition. The membrane module was fabricated using vacuum brazing technique and found to have infinite selectivity towards hydrogen isotopes. Hydrogen and deuterium flux through these dense metallic membranes followed Sieverts' law and hydrogen diffusion through bulk was found to be the rate limiting step. H_2/D_2 flux through the membranes was found to increase with experimental temperature and trans-membrane pressure. It was also observed that the flux through these membranes only depends upon the trans-membrane partial pressure of hydrogen and not upon the total feed gas pressure. Permeability of hydrogen isotopes shows Arrhenius type behaviour with temperature. Permeability of D_2 was found to be lower than that of H_2 at all experimental temperatures and trans-membrane pressures for both $Pd_{0.77}Ag_{0.23}$ and $Pd_{0.77}Ag_{0.10}Cu_{0.13}$ alloys. $Pd_{0.77}Ag_{0.10}Cu_{0.13}$ alloy membrane was found to have higher permeability than $Pd_{0.77}Ag_{0.23}$ alloy. Owing to the higher permeability, the ternary alloy $Pd_{0.77}Ag_{0.10}Cu_{0.13}$ can be a potential membrane material for efficient purification and recovery of hydrogen isotopes in the fuel cleanup system and blanket tritium recovery system of thermo nuclear fusion reactor. This dense metallic membrane can also be used for purification of ^{3}He with minimal tritium contamination. The results from the present investigation depicts that membrane prepared by metallurgical route have infinite hydrogen selectivity, which is the most important condition for the application of the membranes in fusion fuel cycle.

Thermodynamic measurements on $Pd_{0.77}Ag_{0.10}Cu_{0.13}$-$H_2/D_2$ desorption reactions were carried out to explore its potential use in hydrogen isotope purification and separation applications. The experimentally generated pressure-composition isotherms revealed higher equilibrium plateau pressure for deuterium than that for hydrogen thereby showing normal isotope effect. Considering normal isotopic effect, the predicted trend in equilibrium pressure of the three hydrogen isotopes for desorption reaction of $Pd_{0.77}Ag_{0.10}Cu_{0.13}$-$Q_2$ system is: $P_{eq}(H_2) < P_{eq}(D_2) < P_{eq}(T_2)$. The enthalpies and entropies of desorption equilibrium reactions involving the solution (α) and the hydride (β) phases were found to be: $\Delta_r H^o = 37.2 \pm 0.3$ kJ/mol H_2 and 34.7 ± 0.2 kJ/mol D_2; $\Delta_r S^o = 95.4 \pm 0.4$ J/(mol H_2·K) and 98.6 ± 0.3 J/(mol D_2·K). At room temperature, the values of separation factor (α) derived from the PCI measurements are found to be 2.00 for $Pd_{0.77}Ag_{0.10}Cu_{0.13}$-$H_2/D_2$ system. Comparison of the equilibrium desorption plateau pressure for different systems revealed the following trend:

P_{eq} (Q_2) (Pd-Cu) > P_{eq} (Q_2)($Pd_{0.77}Ag_{0.10}Ag_{0.13}$) > P_{eq} (Q_2) Pd > P_{eq} (Q_2) Pd-Ag

The thermodynamic results for the desorption reaction of $Pd_{0.77}Ag_{0.10}Cu_{0.13}$–$H_2/D_2$ shows higher desorption temperature of deuterium compared to hydrogen. Hence, the desorption temperature for release of 1bar of Q_2 gas is predicted to follow the following trend: $T_{des}(H_2) > T_{des}(D_2) > T_{des}(T_2)$. The favourable thermodynamic properties of the ternary alloy such as lower $\Delta_r H^o$, lower T_{des} and higher equilibrium plateau pressure compared to pure Pd enables its application in separation and purification of hydrogen isotopes in self-displacement gas chromatography and membrane reactors.

The constant volume kinetic data for H_2/D_2 absorption reaction for $Pd_{0.77}Ag_{0.23}$ alloy foil and $Pd_{0.77}Ag_{0.10}Cu_{0.13}$ alloy powders were generated and the experimental data were fitted with different kinetic models. Analysis of kinetic data for the hydrogen/deuterium absorption reaction revealed the following results:

i. For $Pd_{0.77}Ag_{0.23}$-H_2/D_2 system, in the bi-phasic ($\alpha + \beta$) region, dissociation and chemisorption is the rate-limiting step for hydrogen/deuterium absorption.

ii. And diffusion of Q through the hydride/deuteride is the rate limiting step for $Pd_{0.77}Ag_{0.10}Cu_{0.13}$-$H_2/D_2$ system, in the bi-phasic ($\alpha + \beta$) region,.

iii. The apparent activation energies (*Ea*) for absorption reaction of $Pd_{0.77}Ag_{0.23}$-H_2/D_2 system are 6.9 ± 0.2 (kJ/mol H_2) and 19.5 ± 0.6 (kJ/mol D_2), respectively.

iv. The activation energies for the absorption reaction of $Pd_{0.77}Ag_{0.10}Cu_{0.13}$-$H_2/D_2$ system are found to be 25.8 ± 0.2 kJ/mol H_2 and 50.2 ± 1.6 kJ/mol D_2, respectively.

v. The activation energies for absorption of hydrogen by $Pd_{0.77}Ag_{0.10}Cu_{0.13}$ alloy is comparable to the activation energy of hydrogen diffusion in Pd

The difference in values of E_a for Pd, $Pd_{0.77}Ag_{0.10}Cu_{0.13}$ and $Pd_{0.77}Ag_{0.23}$ is due to the difference in mechanism of hydrogen absorption in these materials. The above data provide useful information for application of $Pd_{0.77}Ag_{0.23}$ alloy for hydrogen permeation membranes. The faster kinetics of H_2/D_2 absorption on $Pd_{0.77}Ag_{0.23}$ and $Pd_{0.77}Ag_{0.10}Cu_{0.13}$alloys indicates the suitability of these alloys for their application in hydrogen purification membranes.

Overall, the study in this thesis shows that thin cost effective membranes with finite hydrogen selectivity can be prepared by electroless plating method, which, can be applied for industrially produced hydrogen. The membranes prepared by metallurgical route shows infinite hydrogen selectivity and hence can be utilized for purification and separation of hydrogen isotopes in fusion fuel cycle. Further, it was found that the ternary alloy $Pd_{0.77}Ag_{0.10}Cu_{0.13}$ is superior to the binary alloy $Pd_{0.77}Ag_{0.23}$ for hydrogen purification applications.

References

[1] G. J. MacDonald. The long - term impact of increasing atmospheric carbon dioxide levels. Ballinger Pushing Company, Cambridge, MA, 1982.

[2] M. Hook, X. Tang. Depletion of fossil fuels and anthropogenic climate change-A review. Energy Policy. 52 (2013) 797-809

[3] O. Ellabban, H. A. Rub, F. Blaabjerg. Renewable and Sustainable Energy Reviews 39 (2014) 748–764.

[4] Y. Yürüm. Hydrogen energy system: Production and utilization of hydrogen and future aspects, Springer Science & Business Media, 2012.

[5] L. Scchlapbach, A. Züttel. Hydrogen-storage materials for mobile applications. Nature, 414 (2001) 553-558.

[6] B.D. Solomon, A. Banerjee, A global survey of hydrogen energy research, development and policy, Energy Policy 34 (2006) 781.

[7] P. C. Souers. Hydrogen properties for fusion energy. University of California Press, 1986.

[8] W.H Scholz. Processes for industrial production of hydrogen and associated environmental effects. Gas Sep. Purif. 7 (1993) 131-139.

[9] R. Ramachandran, R. K. Menon. An overview of industrial uses of hydrogen. Int. J. Hydrogen Energy 23 (1998) 593-598

[10] M. J. Cole. The generation of pure hydrogen for industrial applications, Platinum Metals Rev. 25 (1981) 12-13.

[11] T. Hübert, L. B. Brett, W. Buttner, Sensors for safety and process control in hydrogen technologies. CRC Press, Florida, 2016

[12] J. Docekal. Hydrogen production from hydrocarbons. Int. J. Hydrogen Energy 11 (1986) 709-714

[13] A. J. Appleby, F.R. Foulkes, Fuel Cell Handbook, Van Nostrand Reinhold, New York, NY, 1989

[14] Hydrogen and Fuel Cells: Emerging Technologies and Applications. Bent Sørensen. Academic Press, 2012.

[15] S. Lee, J. G. Speight, S. K. Loyalka. Handbook of alternative fuel technologies. CRC Press, New York, 2014.

[16] T. E. Springer, T. Rockward, T. A. Zawodzinksi, S. Gottesfeld. Model for polymer electrolyte fuel cell operation on reformate feed effects of CO, H_2 dilution, and high fuel utilization. J. Electrochem. Soc.148 (2001) A11-A23.

[17] P. Ross, P. Stonehart, The use of porous electrodes to obtain kinetic rate constants for rapid reactions and adsorption isotherms of poisons. Electrochim. Acta, 21 (1976) 441-445.

[18] E. Gülzow, M. Schulze. Long-term operation of AFC electrodes with CO_2 containing gases. J. Power Sources, 127 (2004) 243–251.

[19] Fuel Cell Handbook, EG & G Technical Services, U.S. Department of Energy, U.S. Department of Energy, 2004.

[20] W. Vogel, J. Lundquist, P. Ross, P. Stonehart, Reaction pathways and poisons—II: The rate controlling step for electrochemical oxidation of hydrogen on Pt in acid and poisoning of the reaction by CO. Electrochim. Acta, 20 (1975) 79-93.

[21] R. Mohtadi, Studies on the effect of H_2S poisoning of the catalyst in PEM fuel cells utilizing electrochemical methods, Project report, Columbia,5,2002

[22] D.T. Chin, P.D. Howard, Hydrogen sulfide poisoning of platinum anode in phosphoric acid fuel cell electrolyte. J. Electrochem. Soc., 133 (1986) 2447-2450.

[23] S.T. Szymanski, G.A. Gruver, M. Katz, H.R. Kunz, The effect of ammonia on hydrogen-air phosphoric acid fuel cell performance. J. Electrochem. Soc. 127 (1980) 1440-1444.

[24] W. Shi, B. Yi, M. Hou, Z. Shao, The effect of H_2S and CO mixtures on PEMFC performance. Int. J. Hydrogen Energy. 32 (2007) 4412–4417.

[25] J. Sheffield Fusion Energy in India's Long-term Energy Future. Joint Institute of Energy and Environment. Report No. 2003-03.

[26] D. Clery. A Piece of the Sun: The Quest for Fusion Energy, Overlook Press, New York, 2014.

[27] G. McCracken, P. Stott. Fusion: The Energy of the Universe. Elsevier Academic Press, London, UK, 2005

[28] International Thermonuclear Experimental Reactor (ITER). <http://www.iter.org/>.

[29] ITER EDA Documentation Series No. 22, IAEA/ITER EDA/DS/22, 2001.

[30] Figure supplied courtesy of JET-EFDA publications copyright EUROfusion, Author provided, http://figures.euro-fusion.org/Images/JG95.113-55c1500.1500.jpg.

[31] R. Lasser. Tritium and Helium-3 in Metals. Springer Series in Mater. Sci. 9. Springer-Verlag, Berlin, 1989.

[32] M. Glugla, A. Antipenkov, S. Beloglazov, C. Caldwell-Nichols , I. R. Cristescu, I. Cristescu, C. Day, L. Doerr, J. P. Girard, E. Tada. The ITER tritium systems, Fusion Eng Design, 82 (2007) 472–87.

[33] D. J. Suiter. Lithium based oxide ceramics for tritium breeding applications. Argonnel national laboratory, report MDC E-2677, 1983

[34] S. Tosti, C. Rizzello, Advanced membrane science and technology for sustainable energy and environmental applications, A. Basile and S. P. Nunes (Eds.), Woodhead Publishing Limited, 2011.

[35] Y. Kawamura, M. Enoeda, T. Yamanishi, M. Nishi, Feasibility study on the blanket tritium recovery system using the palladium membrane diffuser, Fusion Eng. Des. 81(2006) 809-814.

[36] R. S. Willms, S. Konishi, Fuel cleanup systems for fusion fuel processing, Fusion Eng. Des. 18 (1991) 53-60.

[37] L. M. Gandia, G. Arzamedi, P. M. Dieguez. Renewable Hydrogen Technologies: Production, Purification, Storage. Elsevier, Amsterdam, Netherland, 2013.

[38] M. Kakiuchi. Hydrogen: Inorganic chemistry, in: R.B King (Ed.), Encyclopedia of Inorganic Chemistry, Wiley, 1994, 1444-1471.

[39] A. Basile, A. Iulianelli, Advances in Hydrogen Production, Storage and Distribution, Woodhead Publishing, 2014

[40] P. P. Edwards, V. L. Kuznetsov, W. I. F. David, N. P. Brandon, Hydrogen and fuel cells: Towards a Sustainable Energy Future, Energy Policy, 36 (2008**)** 4356–4362.

[41] D. A. J. Rand, R. Dell, Hydrogen energy: challenges and prospects, Royal Society of Chemistry, UK, 2008.

[42] A Demirbas. Biohydrogen for future engine fuel demands. Springer-Verlag London, 2009

[43] J. L. Wagner, Selective Adsorption of Gases. US Patent 3,430,418 (1969).

[44] S. Sircar, T. C. Golden, Purification of hydrogen by pressure swing adsorption. Sep. Sci. Technol. 35 (2000) 667–687.

[45] S. Sircar, W. C. Kratz. Simultaneous production of hydrogen and carbon dioxide from steam reformer off-gas by pressure swing adsorption, Sep. Sci. Technol. 23 (1988) 2397 -2415.

[46] S. Faraji, R. S. Gharebagh, N. Mostoufi, Hydrogen Recovery from Refinery Off-gases. J. Appl. Sci.5 (2005) 459-464.

[47] T. A. Shenoy, Cryogenic process for separating synthesis gas, US patent, US4217759 A, 1980.

[48] X. Chen, L. Wei, L. Deng, F Yang, Z. Zhang, A review on the metal hydride based hydrogen purification and separation technology, Appl. Mech. Matter. 448-453 (2014) 3027-3036

[49] A. G. Knapton. Palladium alloys for hydrogen diffusion membranes: A review of high permeability materials. Platinum Met. Rev. 1977, 21, 44.

[50] G. J. Grashoff, C. E. Pilkington, C. W. Corti. The purification of hydrogen. Platinum Metals Rev. 27 (1983) 157-169.

[51] N.W. Ockwig, T. M. Nenoff, Membranes for hydrogen separation, Chem. Rev. 2007, 107, 4078-4110.

[52] R. W Spillman, Economics of gas separation membranes. Chem. Eng. Prog. 85 (1989) 41-62

[53] V. M. Gryaznov. Metal containing membranes for the production of ultrapure hydrogen and the recovery of hydrogen isotopes. Sep. Purif. Methods 29 (2000) 171-187.

[54] S. C. A. Kluiters, Status review on membrane systems for hydrogen separation; Energy Center of Netherlands: Petten, The Netherlands, 2004.

[55] S. Adhikari, S. Fernando. Hydrogen Membrane Separation Techniques. Ind. Eng. Chem. Res. 45 (2006) 875-881.

[56] D. S. Sholl, Y. H. Ma, Dense metal membranes for production of high-purity hydrogen, MRS Bull., 31 (2006) 770–773.

[57] T. Graham. On the Absorption and Dialytic Separation of Gases by Colloid Septa Phil. Trans. Roy. Soc. 156 (1866) 399-439.

[58] R. E. Buxbaum, A. B. Kinney. Hydrogen transport through tubular membranes of palladium-coated tantalum and niobium. Ind. Eng. Chem. Res. 35 (1996) 530-537.

[59] D. Edlund, D. Friesen, B. Hohnson, W. Pledger. Hydrogen-permeable metal membranes for high-temperature gas separations. Gas Sep. Purif. 8 (1994) 131-136.

[60] J. E. Lennard-Jones. Processes of adsorption and diffusion on solid surfaces. Trans Faraday Soc. 28 (1932) 333-359

[61] A. Züttel. Materials for hydrogen storage. Mater Today. 6 (2003) 24-33.

[62] W. M. Mueller, J. P. Blackledge, G. G. Libowitz. Metal Hydrides. Academic Press. New York, 1968.

[63] J. W. Gibbs. The Scientific Papers of J. Willard Gibbs, Vol. 1: Thermodynamics, Published by Dover Publications Inc., 1961.

[64] T. B. Flanagan. W. A Oates. Some thermodynamic aspects of metal hydrogen systems. J. Alloys Compd. 404-406 (2005) 16-23.

[65] T. B. Flanagan, B. S. Bowerman, G. E. Biehl. Hysteris in Metal/Hydrogen systems. Scr Metall. 14 (1980) 443-447.

[66] T. L. Ward, T. Dao, Model of hydrogen permeation behavior in palladium membranes, J. Membr. Sci. 153 (1999) 211-231.

[67] D. S. Sholl. Using density functional theory to study hydrogen diffusion in metals: A brief overview, J. Alloys Compd 446–447 (2007) 462–468

[68] A. L. Athayde, R. W. Baker,P. Nguyen. Metal composite membranes for hydrogen separation. J. Membr. Sci. 94 (1994) 299-311

[69] R. G. Musket, Effects of contamination on the interactions of hydrogen gas with palladium: A review. J. Less-Common Met. 45 (1976) 173-183.

[70] H. C. Foley, A. W. Wang, B. Johnson, J. N. Armor. Effect of a model hydrogenation on a catalytic palladium membrane. ACS Symp. Ser. 517 (1993) 168-184.

[71] M. Eriksson, L. G. Ekedahl. Real time measurements of hydrogen desorption and absorption during CO exposures of Pd: Hydrogen sticking and dissolution. Appl. Surf. Sci. 133 (1998) 89-97.

[72] S. A. Koffler. J. B. Hudson, G. S. Ansell. Hydrogen permeation through alpha–palladium. Trans. Metall. Soc. AIME 245 (1969) 1735

[73] A. B. Antoniazzi, A. A. Haasz, P. C. Stangeby, The effect of adsorbed carbon and sulphur on hydrogen permeation through palladium. J. Nucl. Mater. 162–164 (1989) 1065-1070.

[74] J. Chabot, J. Lecomte, C. Grumet, J. Sannier. Fuel clean-up system: Poisoning of palladium–silver membranes by gaseous impurities. Fusion Technol. 14 (1988) 614-618.

[75] F. L. Chen, F. Kinari, Y. Sakamoto, Y. Nakayama. Hydrogen permeation through palladium-based alloy membranes in mixtures of 10% methane and ethylene in the hydrogen. Int. J. Hydrogen Energy 21 (1996) 555-561.

[76] M. V. Swaay, C. E. Birchenall. Permeability and diffusion of hydrogen through palladium. AIME Trans. 218 (1960) 285.

[77] J. K. Ali, E. J. Newson, D. W.T. Rippin. Deactivation and regeneration of Pd–Ag membranes for dehydrogenation reactions. J. Membr. Sci. 89 (1994) 171-184.

[78] H. Connor. Palladium alloy diffusion cells. Platinum Met. Rev. 6 (1962) 130-135.

[79] T. L. Ward, T. Dao. Model of hydrogen permeation behavior in palladium membranes. J. Membr. Sci. 153 (1999) 211-231.

[80] H. Zu¨chner, H. J. Schluter, T. Rauf, R. Hergemoller, Properties of thin palladium-films and their hydrogen-permeability. Ber. Bunsen-Ges. 95 (1991) 1401-1404

[81] R. V. Bucur, N. O. Ersson, X. Q. Tong. Solubility and diffusivity of hydrogen in palladium and $Pd_{0.77}Ag_{0.23}$ containing lattice defects. J. Less- Common Met. 172-174 (1991) 748-758.

[82] H. Hagi. Diffusion coefficient of hydrogen in palladium films prepared by RF sputtering. Mater. Trans., JIM 31 (1990) 954-958.

[83] G. P. Revkevich, A. A. Katsnel’son, V. Khristov. Time and orientation dependence in hydrogen-saturated palladium outgassing rates. Moscow Univ. Phys. Bull. 43 (1988) 74.

[84] G. Q. Lu, J. C. D. da Costa, M. Duke, S. Giessler, R. Socolow, R. H. Williams, T. Kreutz, Inorganic membranes for hydrogen production and purification: a critical review and perspective, J. Colloid Interface Sci. 314 (2007) 589–603.

[85] Y. Sakamoto, S. Hirata, H. Nishikawa. Diffusivity and solubility of hydrogen in Pd–Ag and Pd–Au alloys. J. Less-Common Met. 88 (1982) 387-395.

[86] K. L. Yeung, S. C. Christiansen, A. Varma. Palladium composite membranes by electroless plating technique: Relationships between plating kinetics, film microstructure and membrane performance. J. Membr. Sci. 159 (1999) 107-122.

[87] G. Xomeritakis, Y. S. Lin. CVD synthesis and gas permeation properties of thin palladium/alumina membranes. AIChE J. 44 (1998) 174-183.

[88] N. L. Timofeyev, F. N. Berseneva, V. I. Gromov. Changes in the mechanical properties of palladium and its alloys with silver on exposure to hydrogen. Phys. Met. Metallogr. 51(1981) 159-163.

[89] V. V. Latyshev, V. M. Bystritskiy. Interaction of hydrogen isotopes and diffusion membranes made from palladium alloys. Phys. Met. Metallogr. 71 (1991) 5-24.

[90] S. Yun, S. T. Oyama, Correlations in Palladium membrane for hydrogen separation: A review. J. Membr. Sci. 375 (2011) 28-45

[91] A. Caravella, N. Hara, H. Negishi, S. Hara, Quantitative contribution of non-ideal permeability under diffusion-controlled hydrogen permeation through Pd-membranes. Int. J. Hydrogen Energy. 39 (2014) 4676-4682

[92] G. Sicking, Isotope effects in metal- hydrogen systems, J. Less-Common Met. 101 (1984) 169-190

[93] S. Tosti, L. Bettinali, V. Violante. Rolled thin Pd and Pd–Ag membranes for hydrogen separation and production. Int. J. Hydrogen Energy 25 (2000) 319–325

[94] S. Morooka, S. Yan, S. Yokoyama, K. Kusakabe. Palladium membrane formed in macropores of support tube by chemical vapor deposition with crossflow through a porous wall. Sep. Sci. Technol. 30 (1995) 2877-.

[95] S Tosti, L Bettinali, S Castelli, F Sarto, S Scaglione, V Violante, Sputtered, electroless, and rolled palladium–ceramic membranes. J. Memb Sci. 196 (2002) 241–249.

[96] R. E. Buxbaum, A. B. Kinney. Hydrogen transport through tubular membranes of palladium-coated tantalum and niobium. Ind. Eng. Chem. Res. 35 (1996) 530.

[97] S.C. Chen, G.C. Tu, C. C.Y. Hung, C.A. Huang, M.H. Rei. Preparation of palladium membrane by electroplating on AISI 316L porous stainless steel supports and its use for methanol steam reformer. J. Membr. Sci. 314 (2008) 5–14.

[98] J. Shu, B. P. A. Grandjean, A. Van Neste, S. Kaliaguine. Catalytic palladium-based membrane reactors: A review. Can. J. Chem. Eng., 69 (1991) 1036–1060

[99] J. Tong, R. Shirai, Y. Kashima, Y. Matsumura. Preparation of a pinhole-free Pd–Ag membrane on a porous metal support for pure hydrogen separation. J. Membr. Sci. 260 (2005) 84-89.

[100] Y. H. Ma, Membranes for energy conversion, K. V. Peinemann, S. P. Nunes (Eds.), John Wiley & Sons: 2008, 245-257.

[101] Y.S. Cheng, K.L. Yeung. Effects of electroless plating chemistry on the synthesis of palladium membranes. J. Membr Sci. 182 (2001) 195–203.

[102] J. Shu, B.P.A. Grandjean, E. Ghali, S. Kaliaguine, Simultaneous deposition of Pd and Ag on porous stainless steel by electroless plating, J. Membr. Sci. 77 (1993) 181-195.

[103] E.A. Kikuchi, S. Uemiya, Y. Kude, K. Sugino, N. Sato, T. Matsuda. Palladium/porous-glass composite membrane for hydrogen separation. Chem. Lett. 1988, 1687-1690.

[104] S. Uemiya, T. Matsuda, E. Kikuchi. Hydrogen permeable palladium– silver alloy membrane supported on porous ceramics. J. Membr. Sci. 56 (1991) 315-325.

[105] T. B. Flanagan, W. A. Oates. The palladium-hydrogen system. Annu Rev Mater Sci. 21 (1991) 269-304.

[106] A. K. M. Fazle-Kibria, Y. Sakamoto. Hysteresis of pressure-composition and electrical resistance-composition isotherms of palladium-silver alloys-hydrogen system. Mat Sci Eng. B53 (1998) 256-261.

[107] A.K.M Fazle Kibria, Y. sakamoto, The effect of alloying of palladium with silver and rhodium on the hydrogen solubility, miscibility gap and hysteresis, Int. J. Hydrogen Energy 25 (2000) 853-859.

[108] Flanagan TB, Wang D. Luo S. Thermodynamics of H in disordered Pd-Ag alloys from calorimetric and equilibrium pressure-composition-temperature measurements. J Phys Chem B. 111 (2007) 10723-10735.

[109] H. Brodowsky, E. Poeschel, Hydrogen in palladium-silver alloys, Z. Phys. Chem. 44 (1965) 143.

[110] E. Kikuchi, S. Uemiya, Preparation of supported thin palladium-silver alloy membranes and their characteristics for hydrogen separation, Gas Sep. Purif. 5 (1991) 261-266.

[111] S. N. Paglieri, J. D. Way. Innovations in palladium membrane research. Sep Purif Rev. 31 (2002) 1-169

[112] C. H. Chen, Y. H. Ma. The effect of H_2S on the performance of Pd and Pd/Au composite membrane J. Membr. Sci. 362 (2010) 535–544.

[113] A. Kulprathipanja, G. O. Alptekin, J. L. Falconer, J. D. Way. Pd and Pd–Cu membranes: inhibition of H_2 permeation by H_2S J. Membr Sci. 254 (2005) 49–62.

[114] S. Tosti, L. Bettinali. Diffusion bonding of Pd-Ag rolled membranes, J. Mater. Sci. 39 (2004) 3041 – 3046.

[115] A. Basile F. Gallucci. Membranes for Membrane Reactors: Preparation, Optimization and Selection, John Wiley & Sons, Ltd. 2011.

[116] ASM, Handbook (formerly Metals Handbook, volume 2). Properties and selection: nonferrous alloys and special-purpose materials, 2000

[117] R. Klockenkàmper, J. Knoth, A. Prange, H. Schwenke. Total-Reflection X-Ray Fluorescence Spectroscopy. Analytical chemistry, 64 (1992) 1115-123

[118] R. Klockenkaemper, Total Reflection X-ray Fluorescence Analysis, Chemical Analysis, John Wiley & Sons, New York, 1996.

[119] Bragg WL. The Diffraction of Short Electromagnetic Waves by a Crystal. Proceedings of the Cambridge Philosophical Society. 17 (1913) 43-57.

[120] http://www.icdd.com

[121] P. P. Mardilovich, Y She, Y. H Ma. Defect-free palladium membranes on porous stainless-steel support. AIChE Journal, 44 (1998) 310-322.

[122] D. D. Snnyder. Preparation for deposition, Modern electroplating, Edts. M. Schlesinger, and M. Paunovic. John Willey & sons Inc. 2000.

[123] G. Dehm, J. M. Howe,J. Zweck. In-Situ Electron Microscopy : Applications in Physics, Chemistry and Materials Science. Wiley-VCH Verlag GmbH, germany (2012).

[124] B. D. Fahlman. Materials Chemistry. Springer Netherlands, 2007.

[125] J. Karl. Gross et al., Recommended Best Practices for the Characterization of Storage Properties of Hydrogen Storage Materials: V 3.34 (2s012), National Renewable Energy Laboratory Contract No. 147388, H_2 Technology Consulting, LLC.

[126] NIST Standard Reference Database 23, Web link: http://www.nist.gov/srd/nist23.htm

[127] N.L. Misra, Sangita Dhara and S.K. Aggarwal. Total Reflection X-ray Fluorescence Spectrometry for characterization of nuclear materials, BARC newsletter, 337 (2014) 1-8.

[128] T. J. B. Holland, S. A. T. Redfern, Unit Cell refinement from powder diffraction data: The use of regression diagnostics, Mineral. Mag. 61 (1997) 65-77.

[129] J. W. Arblaster, Crystallographic properties of palladium, Platinum Met. Rev. 56 (2012) 181-189.

[130] V. Jayaraman, Y. S. Lin, Synthesis and hydrogen permeation properties of ultrathin palladium-silver alloy membranes. J. Memb. Sci. 104 (1995) 251-262.

[131] L. Zhao, A. Goldbach, C. Bao, H. Xu, Structural and Permeation Kinetic Correlations in PdCuAg Membranes, ACS Appl. Mater. Interfaces.6 (2014) 22408-22416.

[132] I. K. Suh, H. Ohta, Y. Waseda, High-temperature thermal expansion of six metallic elements measured by dilatation method and X-ray diffraction, J. Mater. Sci. 23 (1988) 757-760.

[133] B. N. Dutta, B. Dayal, Lattice constants and thermal expansion of palladium and tungsten up to 878 °C by X-ray method, Phys. status solidi B, 3 (1963) 2253-2259.

[134] Y. C. Venudhar, C. V. V Reddy, K. S. N. Murthy, and L. Iynengar. Precision lattice parameters and co-efficient of thermal expansion of Pd-Ag-Au-Cu quaternary alloy at elevated temperatures. J. Less Common Met. 109 (1985) L25-L28

[135] E. A. Owen, J. I. Jones, The effect of pressure and temperature on the occlusion of hydrogen by palladium, Proc. Phys. Soc. 49(1937) 587-602.

[136] A. B. Ziya, S. Atiq, A. Aziz, S. Ahmad, A study of thermal parameters of $Ag_{0.50}Pd_{0.50}$ alloy using X-ray diffraction, Physica B, 406 (2011) 3335-3337.

[137] Agilent laser and optics, User manual, vol.1, Agilent Technologies Inc., USA, 2007.

[138] R.W. James, The Optical Principles of the Diffraction of X-rays, Bell, London, 1954

[139] J. A . Ibeers, W. C. Hamilton, International Tables for X-ray Crystallography, IV, The Kynoch Press, Birmingham, 1974.

[140] S. V. N. Naidu, C. R. Houska, X-Ray determination of the Debye temperature and thermal expansion for Pd-Ag-Au system, J. Appl. Phys, 42 (1971) 4971-4975.

[141] M. M. Shukla, N. T. Padial, A Calculation of the Debye characteristic temperature of cubic crystals. Rev. Bras. Fis. 3 (1973) 39-45.

[142] E. K. Delczeg-Czirjak, L. Delczeg, M. Ropo, K. Kokko, M. P. J. Punkkinen, B. Johansson, and L. Vitos. Ab initio study of the elastic anomalies in Pd-Ag alloys, Phys. Rev. B 79 (2009) 085107, 1-8.

[143] F. Hanna, Z. A Hamid, A. A. Aal. Controlling factors affecting the stability and rate of electroless copper plating, Materials Letters 58 (2003) 104– 109

[144] F. Guazzone, E. E. Engwall, Y. H. Ma, Effect of surface activity defects and mass transfer on hydrogen permeance and n value in composite palladium porous stainless steel membranes, Catal. Today.118 (2006) 24-31.

[145] R. Bhandari, Y. H. Ma. Pd–Ag membrane synthesis: The electroless and electro-plating conditions and their effect on the deposits morphology. J. Membr Sci. 334 (2009) 50–63.

[146] F. Guazzone, E. E. Engwall, Y. H. Ma, Effect of surface activity defects and mass transfer on hydrogen permeance and n value in composite palladium porous stainless steel membranes, Catal. Today.118 (2006) 24-31.

[147] T. B. Flanagan, D. Wang, Temperature Dependence of H permeation through Pd and Pd-alloy membranes. J. Phys. Chem. A. 116(2012) 185-192.

[148] E. Serra, M. Kemali, A. Perujo, D. K. Ross, Hydrogen And deuterium in $Pd_{0.75}Ag_{0.25}$ alloy: permeation, diffusion, solubilization, and surface reaction, Metall. Mater. Trans. A. 29A (1998) 1023-1028.

[149] B. H. Howard, R. P. Killmeyer, K. S. Rothenberger, A. V. Cugini, B. D. Morreale, R. M. Enick, F. Bustamante, Hydrogen permeance of palladium-copper alloy membranes over a wide range of temperatures and pressures, J. Membr. Sci.241 (2004) 207-218.

[150] B. D. Morreale, M. V. Ciocco, R. M. Enick, B. I. Morsi, B. H. Howard, A. V. Cugini, K. S. Rothenberger, The permeability of hydrogen in bulk palladium at elevated temperatures and pressures, J. Membr. Sci. 212 (2003) 87-97.

[151] S. Tosti, A. Basile, L. Bettinali, F. Borgognoni, F. Chiaravalloti, F. Gallucci, Long-term tests of Pd–Ag thin wall permeator tube, J. Memb Sci. 284 (2006) 393–397.

[152] N. Itoh, W. C. Xu, Selective hydrogenation of phenol to cyclohexanone using palladium based membranes as catalysts, Appl. Catal. A: Gen. 107 (1993) 83–100.

[153] D. Mendes, V. Chibante, J. M Zheng, S. Tosti, F. Borgognoni, A. Mendes, L.M. Madeira. Enhancing the production of hydrogen via water-gas shift

reaction using Pd-based membrane reactors, Int. J. Hydrogen energy. 35 (2010)12596-12608.

[154] A. Basile, F. Gallucci, L. Paturzo, Hydrogen production from methanol by oxidative steam reforming carried out in a membrane reactor, Catal. Today. 104 (2005) 251–259.

[155] S. Tosti, Supported and laminated Pd-Based metallic membranes, Int. J. Hydrogen Energy. 28 (2003) 1445-1454.

[156] L. Zhao, A. Goldbach, C. Bao, H. Xu, Structural and permeation kinetic correlations in PdCuAg membranes. ACS Appl. Mater. Interfaces, 6 (2014) 22408-22416.

[157] A. M. Tarditi, F. Barun, L. M. Cornaglia. Novel PdAgCu ternary alloy: Hydrogen Permeation and surface properties, Appl. Surf. Sci. 257 (2011) 6626-6635.

[158] C. Ling, L. S. Flecha, D. S. Sholl, First principle screening of PdCuAg ternary alloys as H_2 purification membranes, J. Membr. Sci. 371 (2011) 198-196.

[159] G. Zeng, A. Goldbach, L. Shi, H. Xu, Compensation effect in H_2 permeation kinetics of PdAg membranes, J. Phys. Chem. C. 116 (2012) 18101-18107.

[160] G. G. Libowitz. The solid state chemistry of binary metal hydrides, chapter-4. New York: W. A Benjamin, Inc.; 1965

[161] M. Matsuyama, H. Sugiyama, M. Hara, K. Watanabe. Applicability of Pd-Cu Alloy to Self-Developing Gas Chromatography of Hydrogen Isotopes. J. Nucl. mater. 367-370 (2007) 1096-1101.

[162] N. S. Anand, S. Pati, R. A. Jat, S. C. Parida, S. K. Mukerjee, Thermodynamics and Kinetics of Hydrogen/Deuterium Absorption-Desorption in $Pd_{0.77}Ag_{0.23}$ Alloy. Int. J. Hydrogen Energy. 40 (2015) 444–450.

[163] Y. Yasumatsu, J. L. Wan, M. Matsuyama, K. Watanab. Absorption of Hydrogen Isotopes by Pd–Pt Alloys. J. Alloys Compd. 293-295 (1999) 900-907.

[164] R. Lässer, Tritium in Metals. Z. Phys. Chem. NF. 143 (1985) 23-49.

[165] T. B. Flanagan, S. Luo, J. D. Clewley. Calorimetric Enthalpies for The Reaction of H_2 with Pd-Cu Alloys at 303 K. J. Alloys Compd. 356-357 (2003) 13-16.

[166] W. Luo, D. Cowgill, R. Causey, K. Stewart. Equilibrium Isotope Effect in The Preparation and Isothermal Decomposition of Ternary Hydrides $Pd(H_xD_{1-x})_y$ ($0 < x < 1$ and $y > 0.6$). J. Phys. Chem. B. 112 (2008) 8099-8105.

[167] W. Luo, D. F. Cowgill, R. A. Causey. Equilibrium Isotope Effect for Hydrogen Absorption in Palladium. J. Phys. Chem. C. 113 (2009) 20076-20080.

[168] B. M. Andreev, E. P. Magomedbekov, G. H. Sicking. Interaction of Hydrogen Isotopes With Transition Metals and Intermetallic Compounds; Spronger-Verleg Berlin Heidelberg: Berlin, Germany, 1996.

[169] G. E. Fernández, D. Rodríguez, G. Meyer. Hydrogen absorption kinetics of $MnNi_{4.7}Al_{0.3.}$ Int J Hydrogen Energy. 23 (1998) 1193-1196.

[170] X. L. Wang, S. Suda. A Dehydriding Kinetic Study of $LaNi_{4.7}Al_{0.3}$ Hydride by a Stepwise Method. J. Less-Common Met. 159 (1990) 109-119.

[171] W. Auer, H. J. Grabke. The Kinetics of Hydrogen Absorption in Palladium (α- and β-phase) and Palladium-Silver-Alloys. Ber. Bunsenges. Phys. Chem. 78 (1974) 58-67.

[172] M. Johansson, E. Skúlason, G. Nielsen, S. Murphy, R. M. Nielsen, I. Chorkendorff. Hydrogen adsorption on palladium and palladium hydride at 1 bar. Surf Sci. 607 (2010) 718-29

[173] G. L. Holleck, Diffusion and Solubility of Hydrogen in Palladium and Palladium-Silver Alloys. J. Phys. Chem. 74 (1970) 503-511.